國 立 交 通 大 學

材料科學與工程學系

博 士 論 文

多孔性氧化鋁薄膜之發光性質研究及其在光學上應用

A Study on Photoluminescence Properties of Porous Alumina

Membranes and Their Optical Application

研究生: 陳 蓉 萱

指導教授: 朝 春 光 博士

　　　　　 劉 增 豐 博士

中華民國九十七年六月

多孔性氧化鋁薄膜之發光性質研究及其在光學上應用

A Study on Photoluminescence Properties of Porous Alumina Membranes and Their Optical Application

研究生：陳蓉萱 　　　　　　Student：Jung-Hsuan Chen

指導教授：朝春光博士 　　　Advisor：Dr. Chuen-Guang Chao

劉增豐博士 　　　　　　　　　Dr. Tzeng-Feng Liu

國立交通大學

材料科學與工程學系

博士論文

A Dissertation
Submitted to Department of Materials Science and Engineering
College of Engineering
National Chiao Tung University
in partial Fulfillment of the Requirements
for the Degree of
Doctor of Philosophy
in
Materials Science and Engineering

June 2008

Hsinchu, Taiwan, Republic of China

中華民國九十七年六月

多孔性氧化鋁薄膜之發光性質研究及其在光學上應用

研究生:陳蓉萱　　　　　　　　　　指導教授:朝春光 博士

劉增豐 博士

國立交通大學

材料科學與工程學系博士班

摘　　要

　　本研究的目的是以純鋁的陽極處理法製備多孔性氧化鋁薄膜,並且研究其光激發光特性,更進一步利用氧化鋁薄膜為基板,製造奈米光學材料—硫化鉛奈米晶體,作為其光學應用的延伸。此研究內容分為下列兩部份:

　　首先採用三種不同陽極處理溶液所製備出的氧化鋁模板其孔徑分別為 20、80 及 200 奈米,進行光激發光實驗後發現,只有利用草酸溶液製備的氧化鋁薄膜才能產生高效能的藍光特性,其發光強度隨著氧化鋁薄膜厚度增加而增強,針對其放射光譜分析,發現此一高效能的藍光是由兩種發光中心所貢獻,短波長部份(443 奈米)來源為氧缺陷,而較長波長部分(470 奈米)為草酸溶液中解離出來的陰離子所造成。此外藉由掃描式電子顯微鏡觀察與放射光譜分析可以得知草酸雜質於氧化鋁薄膜中概略的分布情形。

　　另一方面, 將氧化鋁薄膜應用於製造奈米的光學材料硫化鉛奈米晶體前,需要先利用真空鑄造法製備出鉛的奈米線陣列,由穿透式電

子顯微鏡以及凝固行為的理論計算顯示利用此製程可製得不同線徑的單晶奈米線。使用此奈米線陣列與硫化氫氣體進行反應，控制不同的反應溫度及時間，可以得到邊長約為 8 奈米的硫化鉛正方晶體，由光激發光實驗得知，此硫化鉛奈米晶體具有橘紅光的放光特性，相較於硫化鉛塊材(發光特性為紅外光)顯現出強烈的量子限制效應，且隨著反應時間增加，晶體成長過程中所形成的晶體缺陷對於奈米晶體的發光強度有著顯著的影響。

A Study on Photoluminescence Properties of Porous Alumina Membranes and Their Optical Application

Student：Jung-Hsuan Chen   Advisor：Dr. Chuen-Guang Chao
                                             Dr. Tzeng-Feng Liu

Department of Materials Science and Engineering

National Chiao Tung University

ABSTRACT

The objective of this research is to investigate the photoluminescence properties of porous alumina membranes prepared by anodization method. Furthermore, it is an application of porous alumina membranes to work as a template fabricating an optical nanomaterial, PbS nanocrystals. The research results can be divided into two parts.

Porous alumina membranes were produced by anodization method in three kinds of electrolytes in this study. As indicated by the PL emission spectra, the alumina membrane prepared only in oxalic acid solution has a strong blue emission band and the intensity of PL band increases with increasing thickness of alumina membranes. According to the deconvolution of the PL spectra by Gaussian functions, both centers contribute greatly to the PL emission band, one at 443 nm is correlated with the oxygen vacancies and the other at 470 nm is originated from the oxalic impurities. Finally, a distribution of oxalic impurities in the porous alumina wall can be found by the results of SEM and PL experiments.

Before the production of PbS nanocrystals in porous alumina membrane, we have to fabricate Pb nanowires in alumina membranes by the pressure casting process

firstly. According to the theoretical calculation and TEM analyses, the nanowires prepared by the pressure casting process are single crystal structure regardless of the diameter. Then, the PbS nanocrystals can be produced by the reaction between Pb nanowires and H_2S gas. According to the PL spectra, there is a broad orange-red emission band in PbS nanocrystals and the existence of the defects would induce the nonradiative transition and substantially decline the intensity of the emission band. In this study, it can be found that a significant quantum confinement effect makes the energy gap of PbS nanocrystals produce a blue shift from 0.41eV to 1.89 eV.

誌　　謝

　　在交大的校園裡度過了九個年頭，從大學部到博士班畢業，這條路雖然漫長但卻不孤單，感謝在這一路上曾經給予我幫助的師長、同學、朋友們，因為你們的幫忙，讓我在這求學的路上能夠走的更加穩健、順利。其次，感謝家人的支持與包容，使我無後顧之憂，可以專心致力於研究，也得以完成博士學業。

　　還記得剛踏進校園時的青澀模樣，轉眼間也到了要離開的時候，最後藉由此論文為我在交大的求學生涯畫上一個句點，或許它並不夠完美，但至少證明我真的做到了。

CONTENT

TABLE LIST

FIGURE LIST

minutes.

XIII

electron diffraction pattern of the Pb wire. (c) Low magnification

TEM image of the PbS sample with 1 hour sulfization exposed

to H_2S gas at 573 K. (d) Energy- dispersive X-ray spectrum

recorded from a PbS nanocube (the circular area in (c)). (e) High

resolution TEM image of a single PbS nanocrystal. (f) TEM

morphology of the PbS nanocube as the reaction time was 3

hours.

model.

Chapter 1 General Introduction

In recent years, there has been a dramatic proliferation of researches concerned with low dimensional materials. The physical properties of one dimensional and quasi-one-dimensional structure have attracted much attraction for fundamental studies and for practical application in electronics and optoelectronics. Nanomaterials in the templates exhibit both optical and transport anisotropy. The effects of the confinement to nanomaterials by the templates are the dielectric enhancement and the optical anisotropic properties. An appropriate infill, such as Ⅱ-Ⅵ or Ⅳ-Ⅵ semiconductors, can produce the significant broadness of the electronic transitions resulting from the quantum confinement effect. Quantum confinement effect in low-dimensional systems not only provides a forceful tool for managing their optical, electrical, and thermoelectric properties, but also creates possibilities for nano-technological applications. Because of the distinguished optical and electronic properties, the control of the size and morphologies of nano-materials has been a primary focus.

The electrochemically produced porous alumina membranes with highly ordered nanopore arrays have been widely used as templates for the fabrication of ordered nanostructures with nanocrystals, nanowires or nanorods of various materials. The porous alumina membrane itself owns a strong blue photoluminescence band; nevertheless, the phenomenon is still not very clear. Therefore, detailed optical characteristics are technological importance from the viewpoints of the porous alumina membranes. The synthesized nanomaterials in porous alumina membranes for optical device applications also attract many interests until now.

In this study, lead sulfide (PbS) is chosen as the nanomaterial produced in porous alumina membrane for several reasons.

First, PbS is a narrow band gap semiconductor material that can be readily prepared as nanostructure exhibiting strong quantum confinement effect of charge carriers, electron and hole. PbS nanocrystals in the quantum regime (crystal size smaller than the Bohr radius) have tunable broad band absorption from visible light to near-infrared light. Secondly, electrons and holes are equally mobile, unlike cadmium selenide (CdSe) where electron transport dominates. Thirdly, PbS nanocrystals exhibit a relatively long excited state life time. The distinguishing features make PbS nanocrystals be potentially useful on solar cells, optical switches, light emitting diodes, and optically active component for optoelectronic applications.

The present works are to investigate the photoluminescence properties of porous alumina membranes and to use porous alumina membrane as a template to fabricate the optical nanomaterials, PbS nanocrystals. In chapter 2, we provide a background about the basic concepts, luminescence origins, and classification of luminescence materials. After that, some representative researches about photoluminescence phenomenon of porous alumina membranes are indicated. The most popular methods to fabricate PbS nanocrystals and the emission properties of PbS nanocrystals are also reported in chapter 2. Chapter 3 describes the details of fabrication process of porous alumina membranes and PbS nanocrystals. Subsequently all kinds of characteristic analyses methods are also provided. Chapter 4 reports the morphologies and experimental conditions of porous alumina membranes. We explore the effects of thickness, electrolyte, and pore widening on the photoluminescence intensity of porous alumina membranes as well as explain the emission centers about the luminescence. In chapter 5, thermodynamic calculation and experiment identification of Pb nanowires are first described. Then, we demonstrate the morphologies and structure characteristic of PbS nanocrystals produced from the reaction of Pb nanowires and H_2S gas. The growth mechanism is

studied by TEM and thermodynamic calculation. At last, the photoluminescence properties and mechanism of PbS nanocrystals are also provided and explained. In chapter 6, we make a brief conclusion of this work. Finally, a broad concept for future work in this field is given.

Chapter 2 Literature Review

2.1   Photoluminescence of Solids

Luminescence in solids is the phenomenon in which electronic states of solids are excited by some energy from an external source and the excitation energy is released as light. When the energy comes from short wavelength light, usually ultraviolet light, the phenomenon is called photoluminescence.

Photoluminescence can be divided into two major types, namely intrinsic luminescence and extrinsic luminescence. In the former there are three kinds, band-to-band luminescence, exciton luminescence and cross-luminescence. The latter consists of two parts, unlocalized and localized. In unlocalized luminescence, excited electrons and holes of the host lattice participate in luminescence processes. When the luminescence excitation and emission processes are confined to localized centers, this kind of luminescence is called localized luminescence [1].
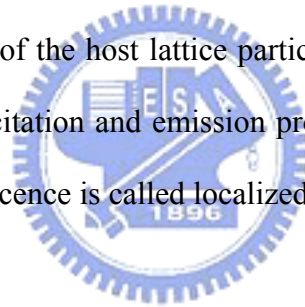
2.1.1   Intrinsic luminescence

There are three kinds of intrinsic luminescence: band-to-band luminescence, exciton luminescence, and cross luminescence. Here each kind of luminescence will be explained and discussed briefly.

(1) Band-to-band luminescence: Luminescence owing to the band-to-band transition can be observed in very pure crystals at relatively high temperature. For example, an electron in the conduction band recombines with a hole in the valence band. This has been observed in Si, Ge, and some Ⅲ-Ⅴ compounds such as GaAs. At low temperature, this luminescence is transformed into exciton luminescence. From the viewpoint of luminescence application, light emission from light emitting diodes and semiconductor lasers are due to the band-to-band transition.

4

(2) Exciton luminescence: An exciton is a composite particle of an excited electron and a hole. It moves in a crystal to convey energy and produces luminescence due to the recombination of the electron and the hole. There are two kinds of excitons: the Winnier exciton and the Frenkel exciton. The Winnier exciton model expresses an exciton as composed of an electron in the conduction band and a hole in the valence band bound together by their attractive coulomb interaction. This model works well for inorganic semiconductors such as Ⅲ-Ⅴ and Ⅱ-Ⅳ compounds. The Wannier exciton moves in a crystal but does not contribute to electric conduction because it is electrically neutral. It emits luminescence by the recombination of the electron and hole composing it. This type of exciton is weakly bound, with an average electron-hole distance large in comparison with a lattice constant. Wannier excitons are stable only at relatively low temperatures, where the binding energies of excitons are higher than the thermal energy. At higher temperatures, where the thermal energy is higher, the excitons are no longer stable and the band-to-band luminescence appears instead.

The Frenkel exciton model is used in cases where the distance between the electron and hole is smaller than the lattice constant. A Frenkel exciton is a tightly bound exciton and essentially an excited state of a single atom. The excitation is localized on or near a single atom because the hole is usually on the same atom as the electron. Typical examples are organic molecular crystals and inorganic complex salts including transition-metal ions. In these materials, the binding within a molecule is strong in comparison with the van der Waals binding between molecules, so that the cxcitons are Frenkel excitons.

(3) Cross-luminescence: Cross-luminescence is produced by the recombination of an electron in the valence band with a hole created in the outermost core band. The luminescence can take place only when the energy difference between the top of

the valence band and that of the outermost core band is smaller than the band gap energy. An Auger process occurs when the hole in the outermost core band is filled nonradiatively with an electron in the valence band and another electron in the conduction band is dropped to the valence band with energy release as luminescence. Therefore, cross-luminescence is observable only in materials satisfying the condition.

2.1.2 Extrinsic luminescence

Luminescence caused by intentionally incorporated impurities, such as metallic impurities or defects, is classified as extrinsic luminescence. Most of the observed types of luminescence that have practical applications belong to this category. Intentionally incorporated impurities are called activators and materials made luminescent in this way are usually called phosphors. Extrinsic luminescence can be divided into two types: unlocalized and localized. In the unlocalized type, the electrons and holes of the host lattice can participate in the luminescence process. In the case of the localized type, the luminescence excitation and emission processes are confined in a localized luminescence center.

(1) Unlocalized luminescence: In semiconductors, most important impurities are donors and acceptors that dominate semiconductive properties, and these act as luminescence activators. Donor-acceptor pair luminescence is a very important example of the unlocalized extrinsic type. Electrons excited into the conduction band are captured by ionized donors, and the holes in the valence band are captured by ionized acceptors. The emission involves electron transfer between neutral donors and neutral acceptors. Therefore, the emission energy of this luminescence generated on a donor-acceptor pair depends on the distance between the donor and the acceptor in a pair.

Another important luminescence of the unlocalized type is isoelectronic traps. If an impurity atom is introduced and replaces or substitutes for the host atom in a semiconductor, it attracts an electron or a hole because of the difference in electron affinity. Such a substitutional atom is called an isoelectronic trap. When the electron affinity of the introduced atom is larger than that of the host atom, the substitutional atom can become an electron trap. If an electron is trapped, a hole is attracted through the coulomb interactive force. In this way, a bound exciton is formed and luminescence is produced. In addition to these mentioned above, the unlocalized luminescence is very important in terms of practical applications.

(2) Localized luminescence: Various kinds of metallic impurities intentionally incorporated in the ionic crystals and semiconductors often create efficient localized luminescence centers. In the localized luminescence, the impurity atoms form the emission centers in the semiconductor. These centers are essentially closed and do not couple with the host atoms. Therefore, the luminescence properties are primary decided by the emission centers and the host material almost has no influence on the luminescence. Localized type centers with regard to energy transitions are classified into: allowed-transition type, and forbidden-transition type. Energy levels of localized centers are seen in the energy band scheme in Fig. 2-1. In the case of A, both the ground and the excited states are located in the forbidden gap. In the case B, the states are embedded in or located below the valence band. There are many intermediate cases between A and B. Localized centers can be also excited by the band-to-band transition as shown by C and D in Fig. 2-1. In the case of C, first a hole is captured by the center and then an electron is captured to produce luminescence. In the case of D, the electron is captured first and then the hole.
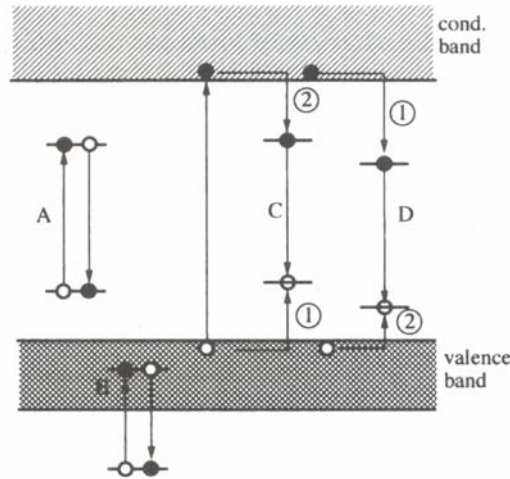
Fig. 2-1 Energy levels of localized centers and luminescence transition [1].

2.1.3   Classification of luminescent materials

Luminescence is the emission of optical radiation resulting from nonthermal excitation of the energy levels of atoms, molecules, polymers, and crystals. Luminescent materials can be classified into several broad groups [2, 3]:

(1) Aromatic molecules: These kinds of materials luminesce in the vapor phase, liquid phase, solid phase, and in fluid or rigid solutions. They constitute the large group, and are used widely in luminescent dyes and paints, fabric and paper brighteners, dye laser, etc.

(2) Inorganic crystals: These types of materials include diamond, ruby, alkali halides, zinc sulfide, calcium tungstate and so on. Their emissions are usually efficient, and result from impurity centers or crystal defects. Luminescent inorganic crystals are used for scintillators, luminescent screens, solid state lasers, jewelry, etc.

(3) Noble gases (He, Ne, Ar, Kr, Xe): These materials luminesce in the vapor phase, liquid phase, solid phase, and solutions. They are used in discharge lamps, gas lasers, and scintillators.

8

(4) Simple inorganic molecules: These molecules usually luminesce in the vapor phases. Some like H_2, D_2, N_2, and Hg, are used in discharge lamps as well as others (N_2, I_2, and CO_2) are applied to gas lasers.

(5) Inorganic ions: These ions notably of the rare earths are used as activators in crystals, glasses, and chelates. Applications include inorganic and glass scintillators, and glass lasers.

(6) Aliphatic molecules (paraffins and cyclohexane): These kinds of molecules are now known to emit in the far UV with a low photon yield.

Whole not exhaustive, this list illustrates the wide range of luminescent materials and their applications.

2.2   Optical properties of porous alumina membranes

Optical properties of aluminum oxide have been investigated since 1970s. Ultraviolet absorption, emission and excitation spectra were studied for high-purity crystalline alumina by Evans [4]. Crystallized alumina [5], including α-, γ-, and η phases, or sapphire [6-7] doped with titanium and chromium ions had also reported the optical behaviors by using various methods from the 70's to the 90's. The photoluminescence properties of the electrochemically produced porous alumina membranes were increasingly investigated in the late 20th century because of the potential use in optoelectronics and nanotechnology. Although many studies have been done on the optical properties of crystalline alumina, little information is available on the optical behaviors of porous alumina membranes. Due to the mechanisms and the characterization of the photoluminescence band are quite complex, the photoluminescence phenomenon has been studied by several researches until now. There are three major models to explain this phenomenon stated in following paragraphs.

Du and his co-works [8] reported that a very strong PL band of the porous alumina membrane anodized in oxalic acid solution was observed when excited by a Xe lamp. Figure 2-2 shows a broad PL band centered about 450 nm occurs in the wavelength of 400-600 nm. The process parameters of the tested samples are shown in table 2-1. The intensity of the PL band increases with the heat treatment temperature, Ta, and reaches a maximum when Ta is 773 K. Electron paramagnetic resonance (EPR) measurement are carried out to find the origin of the blue PL band, as shown in Fig. 2-3. It describes that an obvious EPR signal appears in the spectrum. This means that there are many singly ionized oxygen vacancies (F^+ centers) in the porous alumina membranes because other oxygen vacancies (F and F^{++} centers) are not paramagnetic. Oxygen vacancies have several categories, such as F, F^+, F^{++}, etc. F means an oxygen vacancy with two electrons, F^+ center is formed by an oxygen vacancy trapping an electron, and F^{++} is an oxygen vacancy without electron. Therefore, the authors thought that the PL band originated from single ionized oxygen vacancies (F^+ centers) in the porous alumina membranes. The similar results were also described in other reports [9-10]. Li et al. [9] observed that the PL band peaking around 470 nm in the wavelength range of 200 nm to 500nm was caused by the F^+ centers of the porous alumina membrane with excitation wavelength of 360 nm. The PL properties from silicon based porous alumina films were also investigated by Wu et al. [10]. The PL spectra of as anodized samples showed that there were three strong PL bands centered at 295, 340, and 395 nm with an excitation wavelength of 240 nm. They suggested that oxygen-related defects, F^+ centers, were responsible for the observed PL peaks.
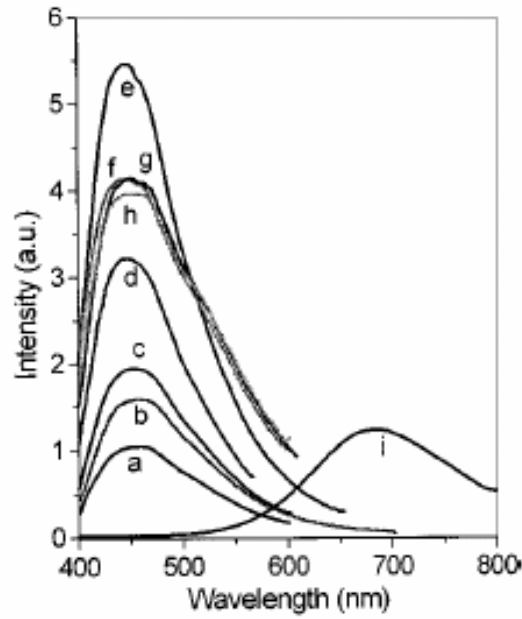
Fig. 2-2 PL spectra of porous alumina membranes and the porous silicon [8].

Table 2-1 Parameters of the heat treatment for the porous alumina membranes [8].

sample	conditions
a	as prepared
b	473 K for 4 hours
c	573 K for 4 hours
d	673 K for 4 hours
e	773 K for 4 hours
f	823 K for 4 hours
g	aging in air for 15 days after heating at 823 K for 4 hours
h	annealing at 823 K in H_2 for 1 hour after aging in air for 15 days
i	porous silicon
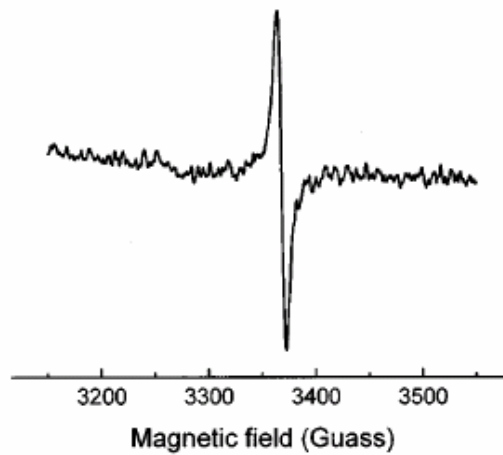
Fig. 2-3 EPR trace at room temperature for porous alumina prepared in oxalic acid

[8].

A further investigation of PL properties from alumina membranes anodized in 0.5 M oxalic acid solution was reported by Huang and his co-works [11]. Figure 2-4 shows that a PL peak in the Blue can be divided into two bands around 405 nm and 455 nm. From the spectra, the intensity of the 455 nm band relative to the 405 nm band increases with the electrolyte concentration. When the electrolyte concentration increases, the current is larger and more charge carriers can move to the alumina. Moreover, the oxygen vacancies in porous alumina membrane can trap two electrons easily, and the density of the F center becomes larger. Therefore, the writers suggested that the two luminescent bands arose from two kinds of different defects (F and F^+ centers) rather than only one kind of defect center, F^+, as reported previously. A defect distribution model in the alumina membrane also presents as shown in Fig. 2-5. The density of the F centers is the largest near the surface because the oxygen vacancies located on the surface can easily trap two electrons and become the F center. Then, the density of the F centers decreases gradually with an increase in the pore wall depth. The situation of the F^+ centers is just reversed.
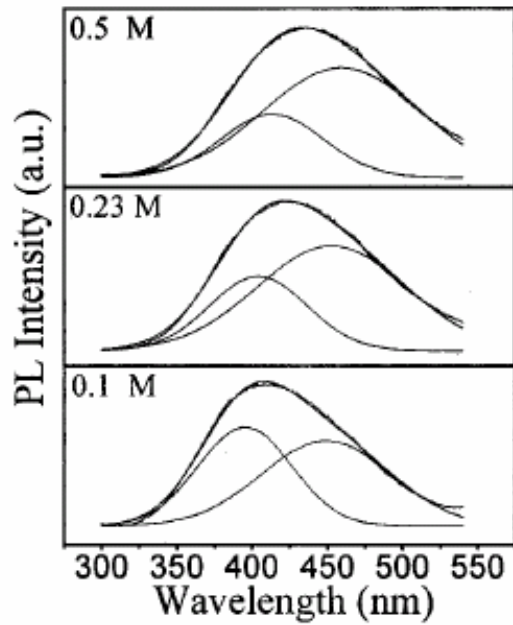
Fig. 2-4 The PL spectra of the alumina membranes obtained by anodization of Al

foils in 0.5, 0.23, and 0.1 M oxalic acid solutions [11].
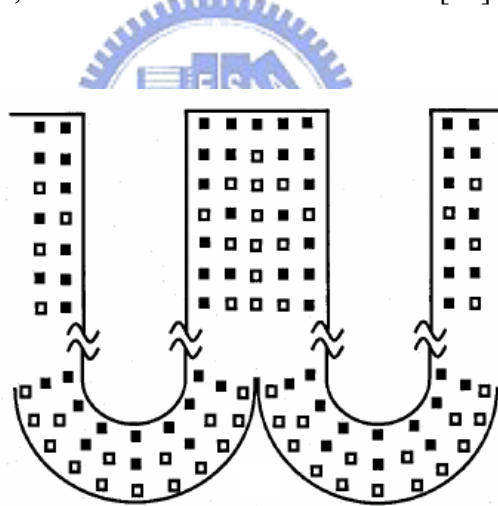
Fig. 2-5 A model for distribution of the F (dark square) and F^+ (open square) centers

in the alumina membranes [11].

The Second model concerning the origins of the blue PL band in porous

alumina membranes was proposed first by Yamamoto et al. [12]. They reported that

the oxalic impurity was the reason for the blue PL band. Later research by Gao et al.

[13] supported the viewpoint of Yamamoto et al. Figure 2-6 shows the PL excitation

and emission spectra of the alumina films anodized in 0.3 M oxalic acid solution in the ultraviolet-to-green region. In Fig. 2-6 (b), an intensive and broad PL emission band peaks around 470 nm. The corresponding excitation spectrum shown in Fig. 2-6 (a) describes that a major excitation band around 360 nm and a weaker side band located around 250 nm are observed. From the results of PL and PLE spectra, it can be suggested that the 470 nm emission band is related to the two excitation centers. Figure 2-7 shows that the intensity of the 470 nm PL emission peak and the intensity of the EPR signal peak for the alumina films vary as a function of annealing temperature. The intensity of the 470 nm PL emission increases with the rise of the temperature, meanwhile, the intensity of the EPR signal decreases with the rise of the temperature. This reveals that the origin of the 470 nm emission band is different from that of the EPR signal. In addition, during the anodization process, the oxalic impurities can be incorporated into porous alumina films [12]. The dissociation of acids generates conjugate base anions (from reaction 1 and 2), and the conjugate base anions can partly replace the O^{2-} in the alumina film.

$$H_2C_2O_4 \rightarrow HC_2O_4^- + H^+ \quad (2\text{-}1)$$

$$HC_2O_4^- \rightarrow C_2O_4^{2-} + H^+ \quad (2\text{-}2)$$
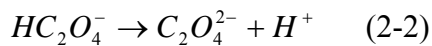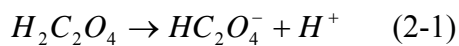
It is reasonable that the incorporated impurities existing in the alumina films have important influences on their optical properties. Therefore, Gao et al. concluded that the evidence for F^+ centers in oxalic alumina membranes was slight. The PL centers produced from the incorporated oxalic impurities during the anodization process were responsible for the 470 nm blue luminescence.

However, the details of the oxalic impurities existing in the alumina films anodized in oxalic acid solution, such as their exciting and distributing forms, are not very clear at present.
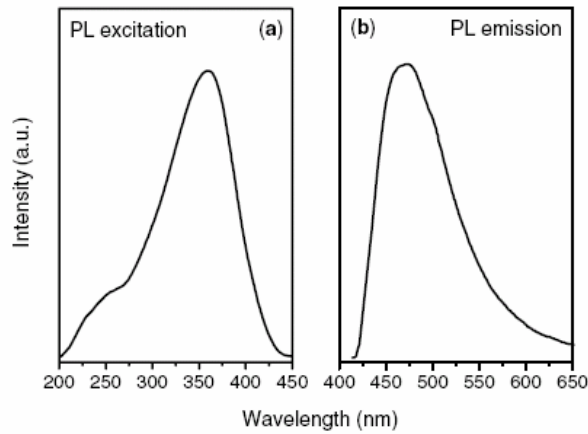
Fig. 2-6 The PL excitation (a) and emission (b) spectra of the porous alumina film

anodized in oxalic acid solution [13].
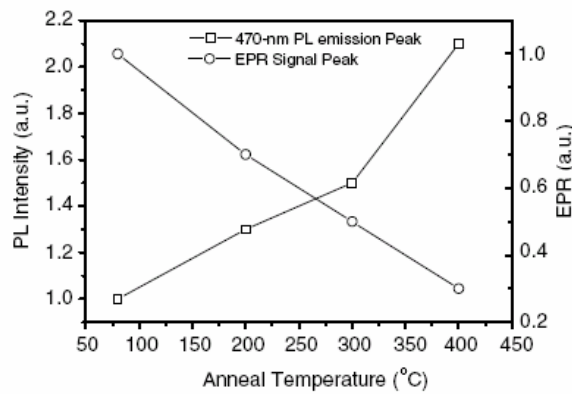
Fig. 2-7 The intensity of the 470 nm PL emission peak and the EPR signal of the

oxalic alumina film as a function of annealing temperature [13].

The last model describes F^+ centers and the oxalic impurities are both the origins of the PL band in porous alumina membranes. Li et al. [14] indicated that a PL band range from 300 to 600 nm was observed. The PL intensity and peak position depended strongly on the excitation wavelength. Figure 2-8 shows that there are two peaks in the PL band: one (P_1) is at constant wavelength of 460 nm, and the other (P_2) increases almost linearly from 420 to 465 nm with excitation wavelength. The authors concluded that there were two PL centers, one originating from the

oxygen-related defects in the barrier layer (the relatively pure alumina), contributing mainly to the second PL band (460 nm), and the other correlated with the aluminum incorporated into the anion-contaminated alumina layer, contributing mainly to the first PL band (420 ~ 465 nm). The similar phenomenon was also observed by Li and his co-works [15]. Indeed, they suggested that there were three optical centers in the annealed alumina membranes. Due to the F^+ centers could convert to F centers at high temperature annealing, the first was originated from the F center, the second was correlated with F^+ centers, and the third was associated with the oxalic impurities incorporated in the alumina membranes.
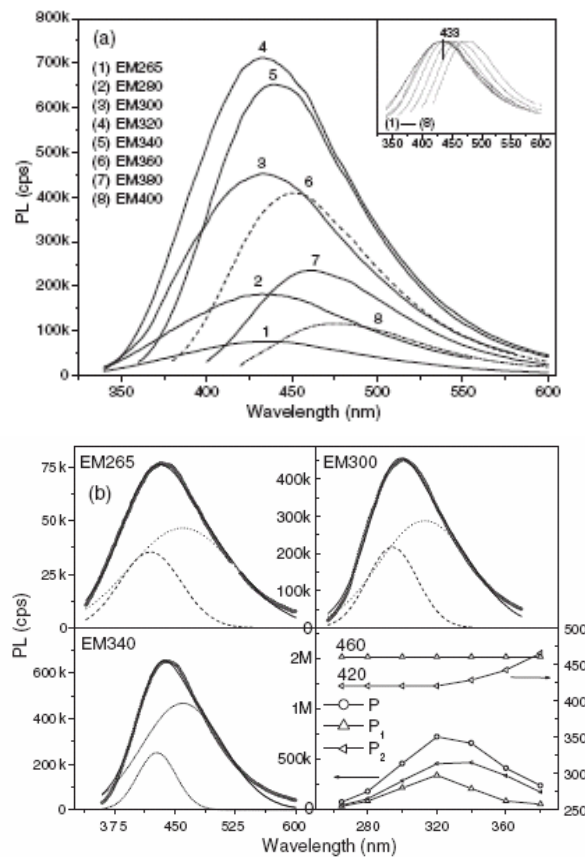
Fig. 2-8 (a) PL emission spectra for porous alumina membranes prepared in oxalic acid solution.(b) The Gaussian fitting of emission spectra with the changes of Gaussian fitting peak position and PL intensity with wavelength [14].

2.3 Reviews of the PbS nanocrystals

2.3.1 Fabrication processes of PbS nanocrystals

Various approaches producing PbS nanocrystals have been developed for years. The different methods for PbS nanocrystals fabrication can be divided into two main categories: PbS nanocrystals not embedded in a matrix and embedded in an attached materials.

(1) PbS nanocrystals not embedded in a matrix

One of the most used chemical routes to produce PbS nanocrystals is colloidal chemistry [16-19]. This method consists in the reaction of the lead precursor (typically a lead salt: lead acetate, nitrate, or perchlorate) and sulfur precursor (usually H_2S, Na_2S or CS_2) in suitable solvents. In this method, the nucleation and growth processes are controlled through suitable stabilizer (capping agent), temperature, solvents, and pH values. Among these factors, the capping agent plays a very important role in controlling the surface states and the optical properties of the PbS nanocrystals.

PbS nanocrystals have also been synthesized using a micelles mediated colloids methods [20-22]. Zhang and his co-works [20] prepared a microemulsion in the system, surfactant/isooctane/water, allowing the reaction between the lead and sulfur precursors inside the micelles. In the system, the surfactant tended to self-associated to minimize contact with water molecules, resulting in the formation of various aggregates with the concentration change of the surfactant. Figure 2-9 shows a possible micelle with a rod-like shape. The water pool within the micelle can be divided into two parts, one part is in the region similar to the shell of a peanut, and the other part is in the sphere micelles just like the peanuts. Thus it can be seen that the size and shape of the products usually depend on the size and shape of the micelles.
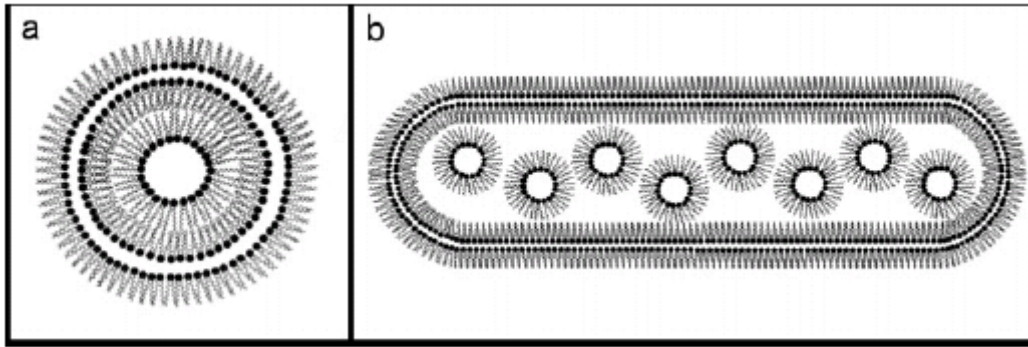
Fig. 2-9 Schematic illustration of a possible micells: (a) the cross section of the short

axis, (b) the cross section along the long axis [20].
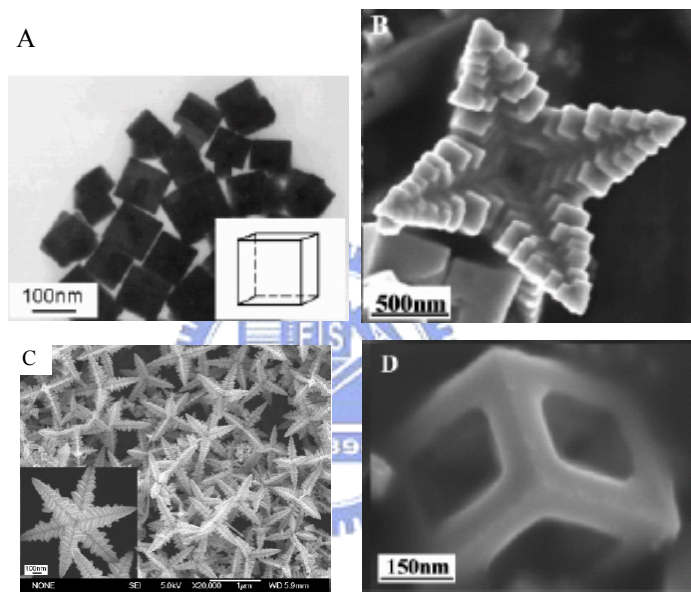
Fig. 2-10 (a) TEM image of PbS nanocubes [26]; (b) SEM image of star-shaped PbS

nanocrystals [25]; (c) SEM image of star-shaped PbS dendrites with six

arms [26]; (d) SEM image of PbS hollowed cube [25].

PbS nanocrystals were also obtained through a thermal decomposition

process [23-26]. Most of the above researches produced near spherical PbS

nanocrystals, however, a variety of morphologies of PbS nanocrystals such as

cubes, rod-like shapes, wires, truncated octahedrons, dendrites, star-shapes, and

flower-shaped structures, had been achieved by thermal decomposition method.

Figure 2-10 shows some PbS nanocrystals with different morphologies prepared by thermal decomposition method. The morphologies of PbS nanocrystals can be controlled by choosing suitable reaction temperature, adjusting pH value, and concentration of precursors.

Other methods, such as chemical deposition [27-28], chemical vapor deposition [29], electrochemistry [30], microemulsion [31], and microwave assisted synthesis [32-33] have been also used to prepare PbS nanocrystals.

(2) PbS nanocrystals in a attached materials

PbS nanocrystals have been embedded in many different kinds of host materials as films or bulks. Polymers are one of the most used matrices to embed PbS nanocrystals [34-40]. A polymer matrix is usually chosen because of uniform and optical transparent properties. Wang et al. [34] used poly(vinyl butyral) (PVB) as a matrix, which acted as both a stabilizer and a robust template, for the nanocrystals growth. Rod shaped PbS nanocrystals were formed inside the PVB film using $Pb(AOT)_2$, (bis(2-ethylhexyl)sulfosuccinate), as the precursor upon exposure to H_2S. PbS nanocrystals in the conducting polymer MEH-PPV, poly(2-methoxy-5(2'-ethyl-hexyloxy)-p-phenylene vinylene), were also obtained for the optoelectronic application [35-36]. The conjugated polymer MEH-PPV was used to control the nanocrystal growth and passivate surface states. The conjugated polymer could act as a colloidal template, and therefore, the nanocrystals self assembled are highly crystalline. A typical example is shown in Fig. 2-11. As prepared PbS nanocrystal in MEH-PPV has a single crystal structure.
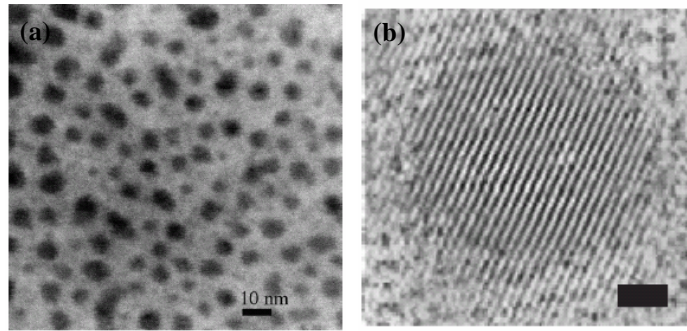
Fig.2-11 (a) TEM image of a dilute sample of PbS nanocrystals; (b) HRTEM image

of the lattice planes in a single nanocrystal (bar =1 nm) [35].

PbS nanocrysatls were also produced on the internal surface of a nanoporous

TiO_2 template. During the process, the TiO_2 template was put into a concentrated

sol-gel solution to coat lead ions and followed by immersing in Na_2S solution to

produce PbS nanocrystals on the TiO_2 template [41-43]. In this process, the PbS

nanocrystals about 3 nm in diameter were obtained, while larger crystals about

3~10 nm also existed when the immersing process was repeated several times.

Glasses doped with PbS nanocrystals had also been prepared by a traditional

glass melting technique [44-45]. Lipovskii et al. [44] melted the materials

including sulfur at a temperature about 1373 K, and then promoted the nucleation

and growth of the nanocrystals while annealing the sample just over the glass

transition temperature in reducing atmosphere. In this process, the size and size

distribution of PbS nanocrystals was strictly related to the heat treatment

schedule.

2.3.2   Emitting properties of PbS nanocrystals

The effects of dimensional confinement on the optical properties of the

materials whose bulk phases exhibit a relatively free motion of electrons have been

studied for many years. Basically, the effects can make the materials to produce a

blue shift in the band gap and appear some discrete sub-bands in the energy band. As

the dimensions of confinement increase, the band gap decreases, and therefore the band to band transitions shift to longer wavelengths, finally approaching the bulk value for a large width. Quantum confinement of electrons and holes also leads to enhanced binding between them and thereby produces increased exciton binding energy compared to the exciton binding energy for the bulk materials, list in table 2-2.

Table 2-2 Semiconductor materials parameters [46-49].

Materials	Band gap energy (eV)	Band gap wavelength (µm)	Exciton Bohr radius (nm)	Exciton binding energy (meV)
CdS	2.58	0.48	2.8	29
CdSe	1.89	0.67	4.9	15
GaN	3.42	0.36	2.8	
GaP	2.26	0.55	10~6.5	3.5
GaAs	1.42	0.87	12.5	5
Si	1.11	1.15	4.3	15
PbS	0.41	3.02	18	4.7

The exciton Bohr radius gives an estimate of the size of the exciton (the most probable distance between the electron and the hole) in a semiconductor. Exciton Bohr radius or often simply the Bohr radius of a specific semiconductor, a_B, is defined as:

$$a_B = \frac{\varepsilon \hbar^2}{\mu e^2} \qquad (2\text{-}3)$$

In the above equation, ε is the dielectric constant of the material, $\hbar$ is Planck constant, and μ is the effective mass of the electron- hole pair defined as:

$$\mu = \frac{m_e m_h}{m_e + m_h} \qquad (2\text{-}4)$$

Here, m_e is the effective mass of electron, and m_h is the effective mass of hole. Besides the Bohr radius, the nature of the confinement is associated with other two lengths: a_e and a_h. The electron radius a_e and the hole radius a_h are indicated as:

$$a_e = \frac{\varepsilon \hbar^2}{m_e e^2} \quad (2\text{-}5)$$

$$a_h = \frac{\varepsilon \hbar^2}{m_h e^2} \quad (2\text{-}6)$$

In PbS, the Bohr radius a_B is 18 nm, and the electron and hole radii are both about 10 nm [50]. The confinement of both electron and hole can be more easily achieved than other semiconductor, like CdSe ($a_e\sim3$ nm, $a_h\sim1$ nm). Therefore, a strong quantum confinement effect can be observed in PbS nanocrystals, with the radius of nanocrystal R ＜ a_B, and R ＜ a_e, a_h [51].

Quantum confinement in the PbS nanocrystals results in an increase of the band gap. The larger band gap can cause a strong blue shift of absorption band and emission band to visible or near-infrared wavelengths. Many research groups have revealed the blue shift phenomenon of optical spectra in PbS nanocrystals, as listed in table 2-3. It can be seen that the photoluminescence spectra of PbS nanocrystals change markedly with the morphologies and the procedures used. The emission band can occur in a wide range from 300 nm to 1600 nm. Most of the published results contain only one emission peak which can be attributed to the PbS nanocrystals. Warner et al. [52] described that PbS nanocrystals with 1 nm in diameter are synthesized by colloidal techniques and capped with oleic acid. Fig. 2-12 shows the PbS nanocrystals with 1 nm in diameter have an absorption band edge at 580 nm and exhibit an emission peak centered at 770 nm. It also suggests that lower synthesis temperature yield the smaller PbS nanocrystals. This is typical of the PL spectra that the peak position displays a red shift as the crystal size increases.

Table 2-3 Optical experimental results of PbS nanocrystals.

State	diameter	Absorption	PLE	PL	Ref.
Oleic acid capped PbS nanocrystals	1~2 nm	580~900 nm		700~900 nm	52
PbS quantum dots in oxide glass	8.5 nm	0.65, 0.85, 1.1 eV			48
Surface passivation PbS nanocrystals	3 nm			636 nm (1.95 eV)	53
PbS nanocrystals	3.3 nm	250 nm		300, 335, 363 nm	54
Surface passivation PbS nanocrystals	2~3 nm		3.44 eV	653 nm (1.9 eV)	55, 61
Alkanethiolate-protected PbS nanocrystals	2~4 nm	560~800 nm	655 nm	804 nm	56
PbS nanocrystals	4 nm	600, 400, 300 nm		700 nm	57
PbS monomers and dimmers in a UV curable sol-gel matrix				510, 810 nm	58
PbS nanocrystals in porous Si	5 nm			665 nm (1.87 eV)	59
PbS nanocrystals in a conjugated polymer	5 nm	1200 nm		1000~1600 nm	60
PbS nanocubes	83 nm×59 nm×22 nm 39 nm×10 nm×7 nm	246~275 nm		434 nm (2.86 eV)	62
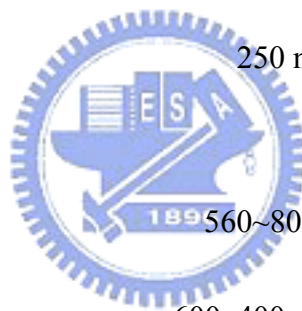
State	diameter	Absorption	PLE	PL	Ref.
PbS nanocystals in silicate glass	3~4 nm			1000~1500 nm	63
PbS nanoparticles in PVA solution	less than 15 nm	540 nm (~2.3 eV)		1100 nm	64
Nano-PbS/ polymer composites	less than 10 nm	317 nm			65
PbS nanocrystals in toluene solution	6.5 nm	1300 nm		1350 nm	17
PbS quantum dots in PMMA				850, 950 nm	66
PbS crystals with the clover-like structure	600 nm (from the apex to the center)	259, 280, 324.5 nm	414 nm	649 nm	33
PbS nanocrystals doped silica film	1~2 nm		311 nm	446 nm	67
PbS hollow spheres	10 nm (size of crystallites) 20 nm (thickness of sphere shell) 500 nm (diameter of sphere)	238, 322 nm		352 nm	68
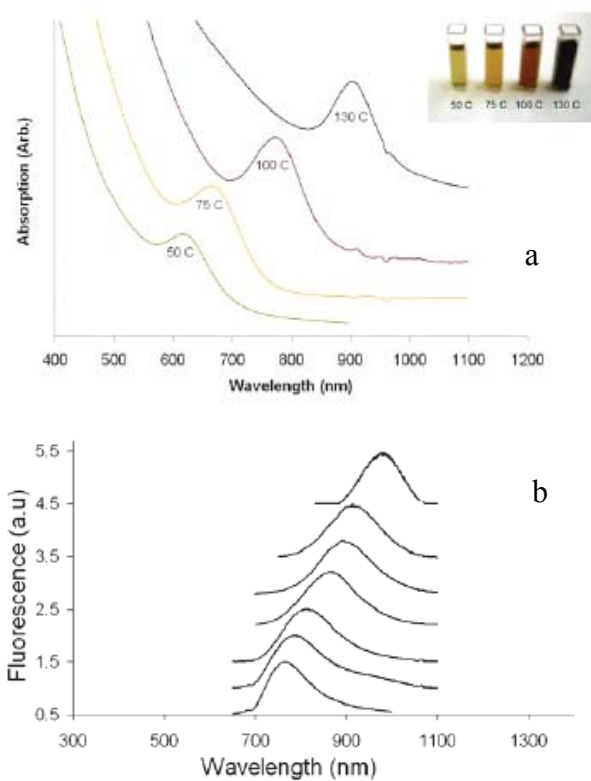
Fig. 2-12 (a) Absorption spectra of oleic acid capped PbS nanocrystals prepared at 50, 75, 100, 130℃. (b) Fine tuning of the photoluminescence spectra of oleic acid capped PbS nanocrystals as the temperature is varied between 40 and 130 ℃ [52].

Chapter 3 Experimental procedures

3.1 Fabrication of porous alumina membranes

General commercial aluminum foils with purity of 99.7 wt % were used to produce porous alumina membranes. The aluminum sheets first annealed at 673 K for 3 hours to release the mechanical stresses of the substrate and then electropolished. After electropolishing, two-step anodization process was progressed. In the first anodization process, the treated aluminum sheet was anodized in an acid solution under a particular condition with a platinum plate as the cathodic electrode. The detailed experimental parameters are list in table 3-1. The pre-formed alumina was removed by wet etching in the mixture of phosphoric acid (6 wt %) and chromic acid (2 wt %) until it entirely dissolved. The sample was anodized again under the same condition like the first anodization. The thicknesses and pore sizes of templates were controlled by choosing suitable anodizing conditions. Hexagonally ordered pores were obtained on the aluminum surface after the entire anodization process. Then, the remaining aluminum was removed in a saturated $CuCl_2$ solution and finally cleaned the sample thoroughly in distilled water.

Table 3-1 3 sets of parameters for anodization of aluminum polished foils in this study.

Electrolyte	Concentration	Voltage (V)	Temperature (K)
H_2SO_4	10 wt %	18	281
$H_2C_2O_4$	0.3 M	40	293
H_3PO_4	0.1 M	160	276

3.2 Formation of Pb nanowires in the porous alumina membranes

To investigate the properties of the 1D quantum wire system, a template is usually used to fabricate various material nanowires. Porous anodic alumina membranes with average channel diameters of 20, 80, 200 and 300 nm were used as templates in this experiment.

The fabrication of the Pb nanowires was based on the pressure casting process of melted metal. The purity of the initial lead was 99.99 wt %, while the content of impurities did not exceed 10^{-2} wt %. An alumina template, still attached to Al substrate, and a piece of Pb metal were placed inside the vacuum chamber. Meanwhile, the vacuum pressure was maintained at 10^{-6} Torr to prevent the active metal oxidation. A hydraulic force was applied on the Pb melt to inject the melt into the nanochannels of the porous alumina membrane. Solidification proceeded using a water cooling method at the bottom of the chamber. We adopted a quenching procedure during Pb melt solidification to separate the nanowire and the remaining metal on the anodic alumina template. Then, the Pb nanowires were formed after cooling to room temperature. This quenching procedure could provide a steep temperature gradient between the nanowires and remaining metal. We could easily obtain the Pb nanowire arrays inside the alumina membrane.

3.3 Production of PbS nanocrystals

The fabrication procedures of the PbS nanocrystals are shown in Fig.3-1. Firstly, the porous alumina membranes as templates were fabricate after the anodization of the published aluminum foils (99.7 wt %) in 10 wt % sulfuric acid solution (H_2SO_4) and 0.3 M oxalic acid solution ($H_2C_2O_4$). The nanochannel structures with diameters of 20 nm and 80nm were obtained on the Al substrate. Secondly, a piece of Pb metal and an anodic aluminum oxide template were placed inside an ultra-vacuum chamber. After the chamber was heated to 673 K, a hydraulic force was applied to inject the Pb melt into the nanochannels. When the Pb melt solidified, the Pb nanowire arrays formed in the alumina membrane. Finally, a sulfization procedure was proceeded to obtain PbS nanocrystals. Two different methods were adopted to fabricate the PbS nanocrystals in this study. The first process was that the PbS nanocrystals produced via the reaction between Pb nanowires and sulfur vapor. Pb nanowires with the porous alumina membrane and sulfur powders were sealed in a vacuum glass tube. The tube was put in a furnace with heat treatment at 573K for 3 and 8 hours. The sulfur vapor reacted with the Pb nanowires and the PbS nanocrystals were produced then.

The second method was using H_2S gas to produce the PbS nanocrystals. The nanowires were put into a gaseous furnace full of H_2S gas whose flow rate was 30 milliliter/minute and applied a heat treatment at 573 K for 1, 3, 6, 8 hours. Finally, the PbS nanocrystals were produced on/in the porous alumina membrane.
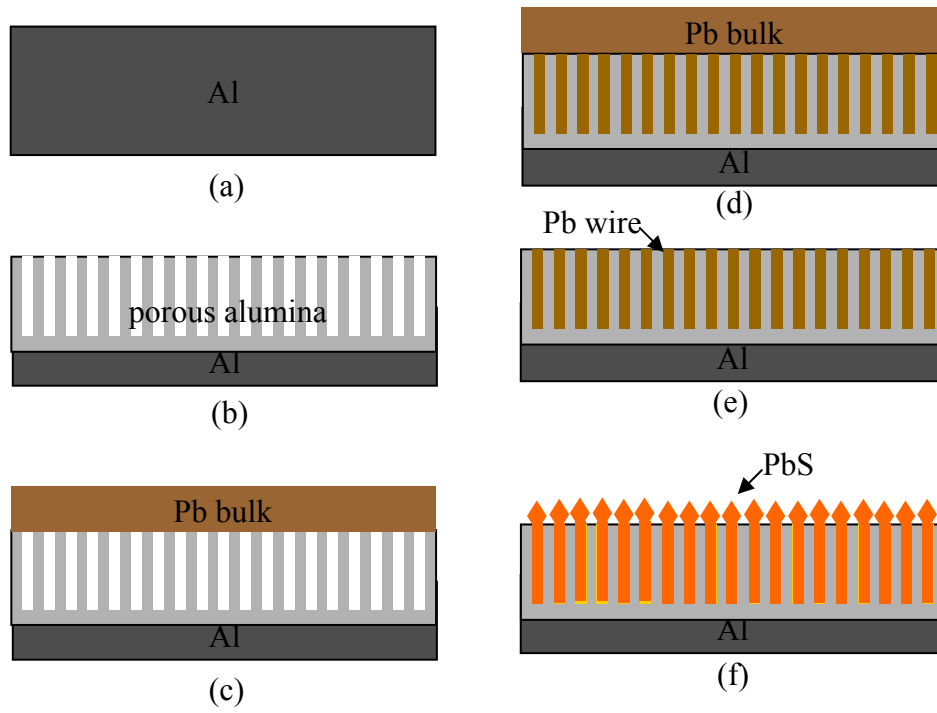
Fig. 3-1 Schematic diagrams of PbS nanocrystals fabricated in this work.
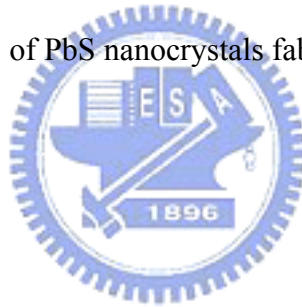
3.4 Characteristic analyses

Characterization of nanomaterials and nanostructures is largely based on the surface analysis techniques and conventional characterization methods developed for bulk materials. Various structural characterization methods, some typical physical and chemical characterization techniques are discussed following.

3.4.1 Structural characterization

X-ray diffraction (XRD)

X-ray diffraction analysis is a kind of non-destructive analytical technique and has very widely applications on material science including phase identification and the crystal structure of solids, identification of unknown materials, orientation of single crystals, preferred orientation of polycrystals, etc. In X-ray diffraction, a collimated beam of X-rays is incident on a specimen and is diffracted by the crystalline phases of the specimen according to Bragg's law. The diffraction pattern is used to identify the specimen's crystalline phases and to measure its structural properties. In this study, the crystal structures of porous alumina membranes, Pb nanowires, and PbS nanocrystals were analyzed by X-ray diffraction (Cu Kα, λ= 1.5418 Å, Siemens D5000).

Scanning electron microscopy (SEM)

When the electron probe illuminates the specimen, secondary electrons, backscattered electrons, transmitted electrons, characteristic X-ray, and so forth are emitted from the specimen surface. A scanning electron microscope is a type of electron microscope and a useful tool for high resolution image observation. The surface image of the specimen is obtained from the signals of the secondary electrons detected by the secondary electron detectors.

Morphologies of the porous alumina membranes, Pb nanowires and PbS nanocrystals were observed by a JEOL JSM-6500 scanning electron microscope in this study.

Transmission electron microscopy (TEM)

TEM is a powerful tool to understand the structural features and chemical information at a spatial resolution less than 1 nm of materials. When materials are in the nanometer scale, most of properties and behaviors observed are typically group characteristics corrected from a large number of nanostructural materials. Characterization and measurement of individual nanostructures require not only extreme sensitivity and accuracy, but also ultra-high resolution. A TEM with a finely focused electron probe can provide a complete structural characteristic of a single nanocrystal. In this study, the investigations of the nanowires and nanocrystals were carried out with a Philip Tecnai 20 transmission electron microscope and a JEOL JEM-2100F transmission electron microscope operating at 200 kV.

Atomic force microscopy (AFM)

2D/3D morphologies of the annealed aluminum sheet were determined by the tapping atomic force microscope (Veeco D5000) in this study. AFM is a novel technique for high resolution imaging of conducting as well as non-conducting surface. The physical meaning in AFM is the interaction force between the sample surface and a sharp probing tip. There are three types of imaging modes in AFM: contact, tapping, and non-contact modes. In the tapping mode, the probing tip is periodically in contact with the sample surface and the morphology of the sample is obtained from the change of the

vibration amplitude of the oscillating cantilever.

Focus ion beam (FIB)

In this study, the advanced TEM specimen preparation method of using a focused ion beam miller (FEI Dual Beam FIB) was applied to prepare the cross-sectional TEM specimen. The dual beam FIB system combines an ion beam and a scanning electron beam on the same platform. FIB/SEM technology is also utilized in novel ways to engineer nanostructures and devices using ion and electron beam deposition of metals, organic materials or insulators, as well as milling of materials with the ion beam. The use of FIB for the nanometer precision of TEM specimen preparation has become more and more popular because it is possible to mill very thin membranes from a specific area of a sample.
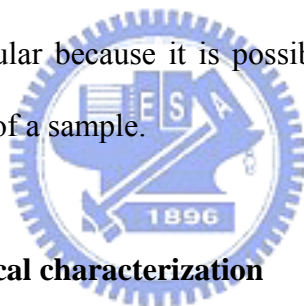
3.4.2 Physical and chemical characterization

Energy dispersive X-ray spectroscopy (EDX)

An energy dispersive spectrometer is usually equipped in an electron microscope. The instrument can also be used as an electron probe microanalyzer for accurate, efficient and non-destructive element analysis or element distribution observation of microscopic areas on the specimen surfaces or cross-sections. This capability is very useful in the fields of materials science such as metals, minerals, semiconductors, and new materials, as well as biological or industrial researches. In the present study, the compositions of nanowires and nanocrystals were detected by energy dispersive X-ray spectroscopy (EDS, Oxford).

X-ray photoelectron spectroscopy (XPS)

X-ray photoelectron spectroscopy, also commonly knows as electron spectroscopy for chemical analysis (ESCA), is used to study the composition and electronic states of the surface region in a sample. It makes use of the photoelectric effect in which an X-ray beam strikes the surface of a material to eject electrons that leave the surface with various energies. This technique is capable of providing information on the oxidation states, immediate chemical environment, and concentration of the constituent atoms. In this study, the chemical compositions of PbS nanocrystals were detected by X-ray photoelectron spectrum (XPS, VG Scientific Microlab 350).

Differential scanning calorimeter (DSC)

Differential scanning calorimeter is a thermal analysis technique which is used to measure the temperatures and heat flows associated with transitions in materials as a function of time and temperature. The operation of a DSC is based on measurement of the thermal response of an unknown substance as compared with an inert reference material when the two specimens are heated or cooled at a constant rate. The difference in thermal response of the two specimens maybe caused by differences in mass, specific heat, heats of reaction or phase transitions, etc. In the present study, the PerkinElmer Diamond differential scanning calorimeter was used to measure the thermal characters of nanocrystals and nanowires.

Photoluminescence spectrometer (PL)

Photoluminescence (PL) is a luminescence caused by ultraviolet, visible, or infrared radiation. PL spectroscopy is a sensitive, non-destructive

technique that can provide valuable information on the type and distribution of defects or impurities in a crystal. Since PL is a characteristic of a given luminescent materials, its measurement can be used for material characterization. In this study, the photoluminescence experiment was performed at room temperature using a Jobin-Yvon Spex Fluolog-3 spectrophotometer with a xenon lamp as the excitation light source. The spectra fitting were executed by the Gaussian functions in the Origin 7.0 software.

Chapter 4 Photoluminescence properties of porous alumina membranes

4.1 Motivation

In recent years, nanostructure materials have inspired great interest in fundamental study and high-tech industry because they are expected to exhibit very different properties from their bulk forms. Low-dimensional systems represent one of the important fields in advanced material research. Since the development of nano science and technology, researches on porous alumina membranes have drawn much attention. Porous alumina usually contains a hexagonally packed two-dimensional array of cylindrical pores with a relatively uniform size and is often prepared by using anodization of aluminum foils in an anodic medium [69-71]. Due to their regular nanostructure, they have been widely used as templates for fabricating nanostructured materials, such as wires, tubes, and rods for application in the fields of electronics or photoelectronics [72], magnetics [73], energy storage [74], photocatalysis [75], and biosensors [76].

Optical properties of aluminum oxide have been investigated since 1970s. However, photoluminescence property of porous alumina membranes was first studied in 1999. Du and his coworkers reported that a strong and broad PL band was observed in porous alumina membranes anodized in oxalic acid solution [8]. The mechanisms and the characterization of the PL band were complex, and therefore there were many different explanations about this phenomenon. For example, Li et al. suggested that the PL and optical absorption in the wavelength range of 200 nm to 500 nm can be attributed to the F^+ centers in alumina membranes [9]. Gao et al. reported that the oxalic impurity was the origin of the PL emission [13].

While many studies have been done to date, more researches need to be

conducted to understand the PL behavior more clearly. The present study is carried out to determine the relationship between the thickness and the PL properties of porous alumina membranes. In order to establish a reasonable inference to examine the phenomenon, the effect of electrolyte and the distribution of oxalic impurities in porous alumina membrane are also discussed. The results of this study could be useful to understand the mechanism of the optical properties of porous alumina membranes.

4.2 Microstructure observation and characterization of porous alumina membranes

In this study, porous alumina membranes were produced by anodization method by a two-step process in sulfuric acid solution, oxalic acid solution, and phosphoric acid solution. The porous alumina film was found to grow on aluminum with an equilibrium of oxide dissolution at the interface of the alumina / electrolyte and oxide grown at the metal / alumina interface [77]. Figure 4-1 (a) shows that after the aluminum sheet is heat treated at 673 K for 3 hours, there is a thin oxide film on the surface of aluminum. Based on the AFM measurement result (Figure 4-1 (b)), it can be verified that the oxide is a dense alumina with a thickness about 20 nm and the roughness of 5.6 nm. As shown in Figs. 4-2 (a)-(c), the SEM morphologies of porous alumina membranes produced in sulfuric acid solution (a), oxalic acid solution (b), and phosphoric acid solution (c) reveal that the nanopores with different diameters are order and uniform arrays. The corresponding pore size distributions of porous alumina membranes are performed by the histogram analysis. As presented in Fig. 4-3, the histograms are plotted by measuring at least 50 pores in each sample and the average pore diameters are obtained by fitting the histograms with Gaussian functions. The average pore diameters are 18.66 ± 3.36 nm, 79.11 ± 10.04 nm, and

191.77 ± 21.66, respectively. The porosity of each sample is 16.49 %, 36.41%, and 40.72 %. The relationship between anodization time and the thickness of porous alumina membranes anodized in different electrolytes is shown in Fig. 4-4 in which the thickness is measured using SEM microscopy. It can be seen that the alumina membrane anodized in sulfuric acid solution has a faster growth rate than other samples. According to above results, we can understand more clearly about the characters of the porous alumina membranes and prepare the required sample easily by choosing the optimum anodization conditions. Moreover, all the as-prepared alumina membranes are shown to be amorphous in nature as observed by using the XRD technique (Fig. 4-5).
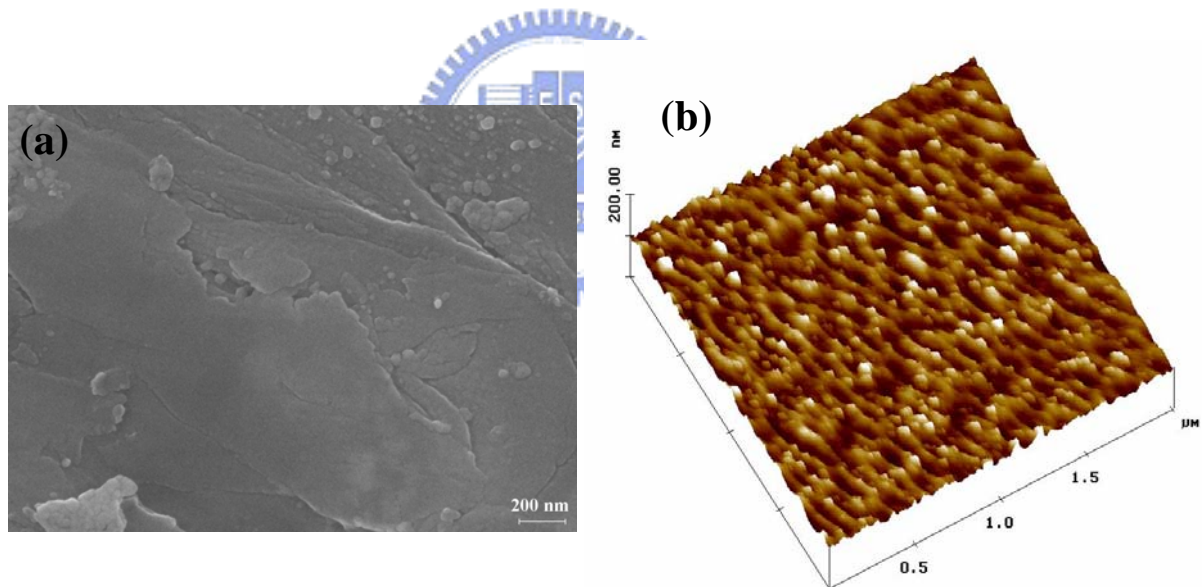
Fig. 4-1 (a) SEM image of an aluminum sheet annealed and (b) AFM image of an aluminum sheet, both annealed at 673 K for 3 hours.
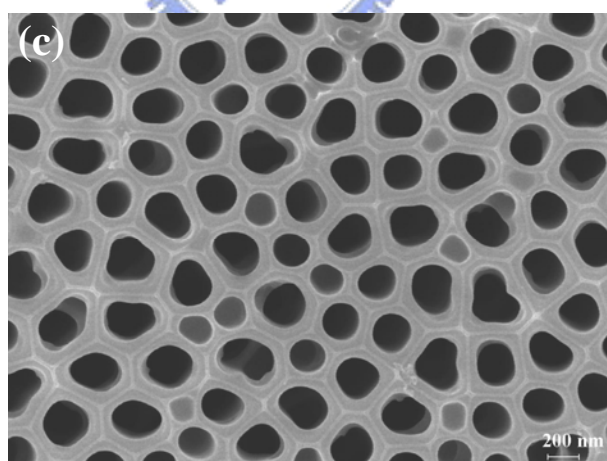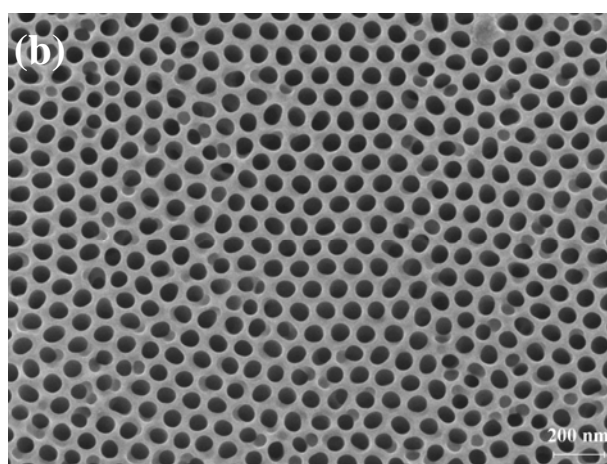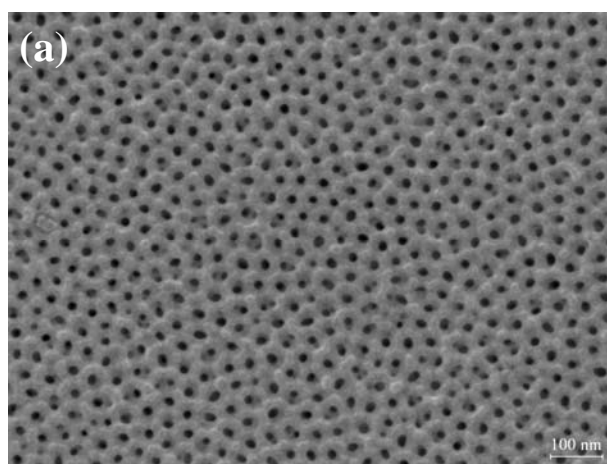
Fig. 4-2 SEM images of porous alumina membranes were formed in (a) sulfuric acid

solution, (b) oxalic acid solution, and (c) phosphoric acid solution.
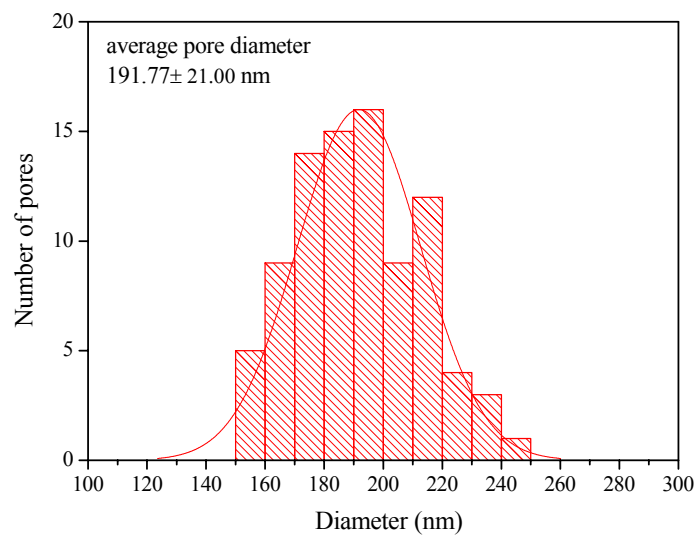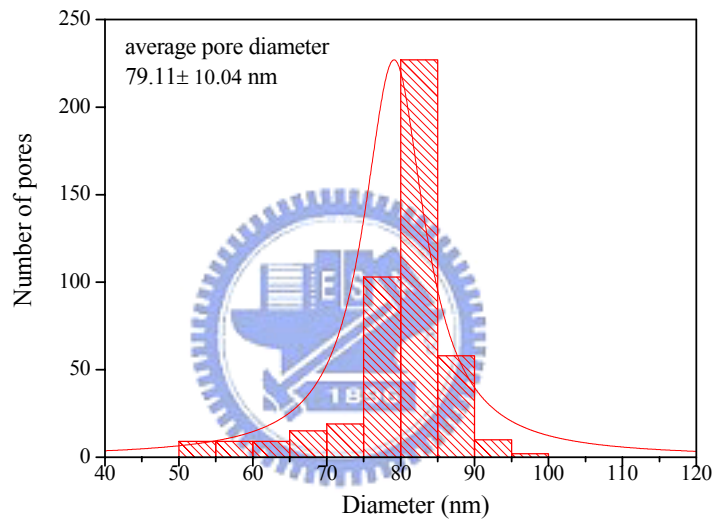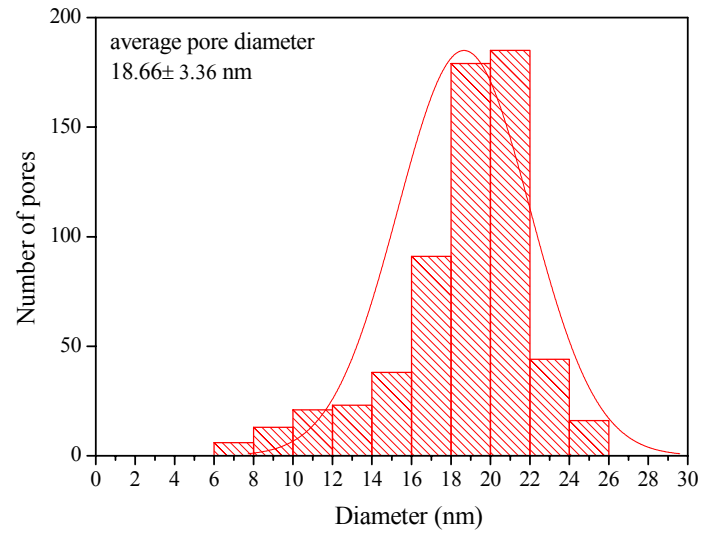
Fig. 4-3 The representative histograms of the porous alumina membranes shown in

Figs. 4-2 (a)-(c). The average pore diameters denote in the figures.
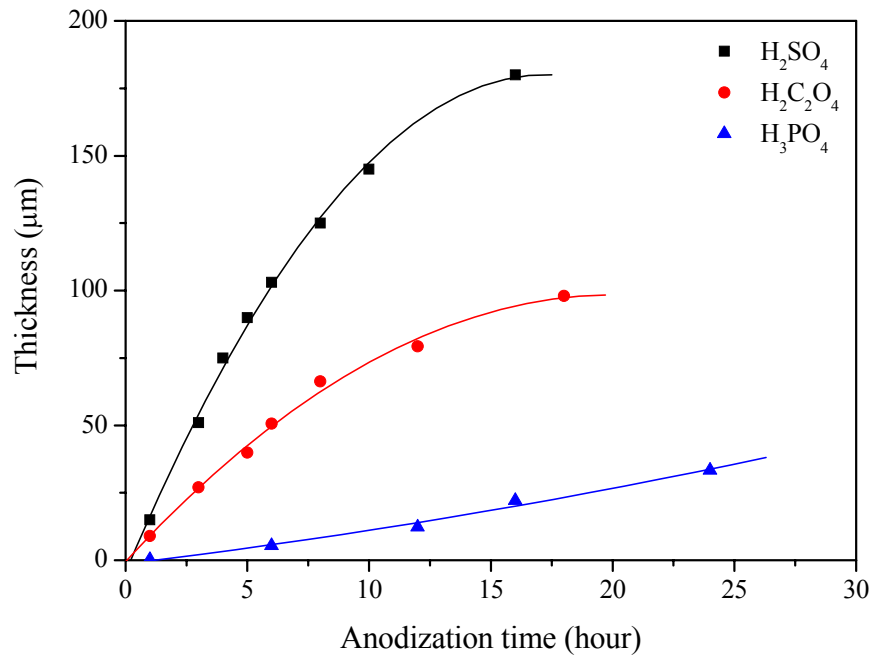
Fig. 4-4 The correlation between the thickness of porous alumina membranes and anodization time.
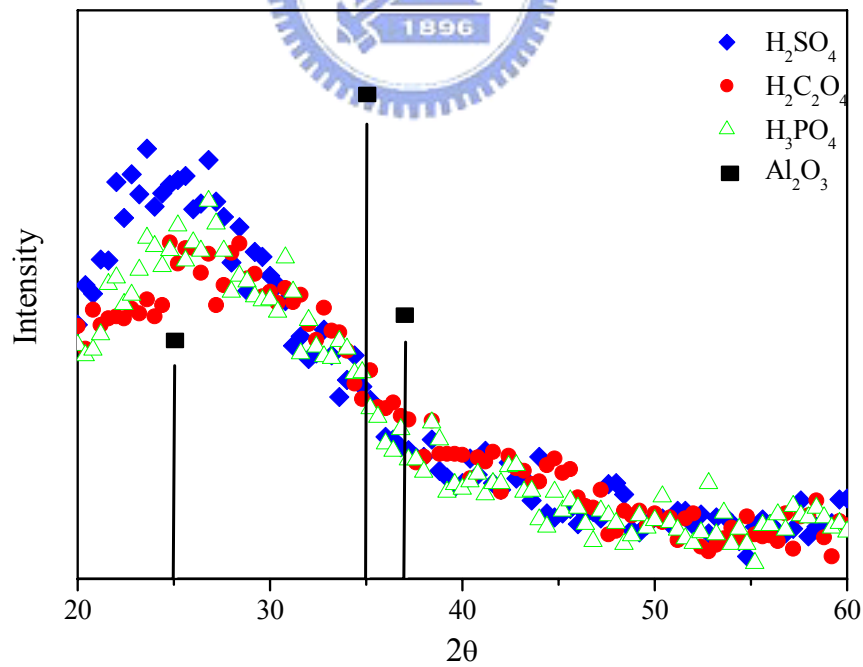
Fig. 4-5 X-ray diffraction profile of porous alumina membranes produced in sulfuric acid solution, oxalic acid solution, and phosphoric acid solution.

4.3 Photoluminescence properties of porous alumina membranes

4.3.1 Photoluminescence centers in porous alumina membranes anodized in oxalic acid solution

PL is used to assess the optical properties of our samples prior to anodization and after formation of porous alumina. Figure 4-6 shows that the characteristic PL spectra of the dense alumina and porous alumina membranes are broad blue-emitting bands at 420-600 nm. In Fig. 4-6, curve 1 peaking at 443 nm is attributed to the dense alumina on the aluminum sheet and curves 2 peaking at 470 nm can be attributed to the porous alumina membranes prepared in oxalic acid solution for 10 minutes. When the anodization time is longer than 15 minutes (e.g., 15-60 minutes), the emission band is found to be broad centered at 452 nm, as shown in curves 3 to 6. The thickness of membrane is closely related proportion to the anodization time in oxalic acid solution. The growth rate of alumina grew on the aluminum surface is 72 nm per minute, estimated from the slope of curve shown in Fig. 4-7. As the thickness of the porous alumina membrane increases, the peak intensity of the emission band increases gradually and the peak position changes obviously. Moreover, the dense alumina and the porous alumina membranes have different emission centers, which induce a red shift for the PL emission peaks. As indicated by the results, both the thickness of porous alumina membranes and the PL intensity are found to increase with increasing anodization times.

Fig. 4-6 PL spectra of the aluminum sheet and porous alumina membranes prepared in oxalic acid solution. 1: annealed aluminum; 2: anodized 10 minutes; 3: anodized 15 minutes; 4: anodized 20minutes; 5: anodized 40 minutes; 6: anodized 60 minutes.
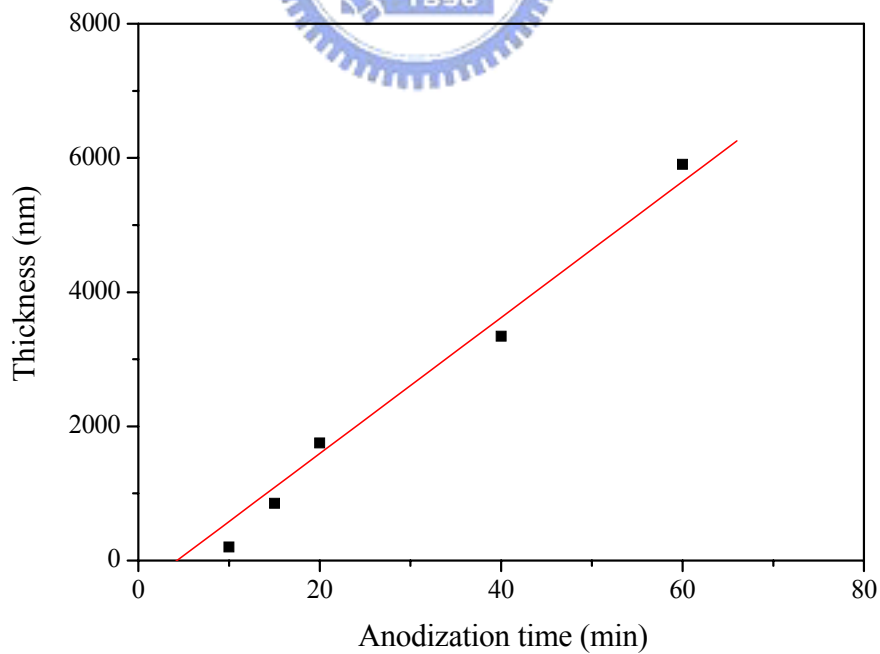
Fig. 4-7 Thickness as a function of anodization time when the aluminum sheet was anodized in 0.3 M oxalic acid solution.

In this work, PLE spectra were measured in the 200-400 nm spectra range for porous alumina membranes. The spectra monitored at 440 nm and 470 nm are presented in Fig. 4-8 (a) and (b), respectively. When the anodization time is shorter than 15 minutes (curves 1-3), the PLE spectra monitored at 440 nm exhibit two excitation centers located at 343 and 360 nm, respectively, except the curve of the dense alumina which only shows a vague peak at around 343 nm. Furthermore, the intensity of the excitation band grows steadily and the peak positions remain unshifted at 350 nm when the anodization time exceeds 15 minutes (curves 4-6). The spectra monitored at 470 nm are similar to those monitored at 440 nm but there is a red shift in the excitation spectra. When the spectra monitored at 470 nm, the excitation center located at 360 nm achieves a dominant position and the other center around 343 nm has a less influence on the excitation band. Therefore, it is reasonable that a red shift appears in the excitation spectra monitored at 440 nm and 470 nm. These findings seem to suggest that the observed blue emission peaks occurred at 443 nm and 470 nm may be attributed to the different excitation centers.

The mechanisms of photoluminescence for porous alumina membranes have been studied by several researchers. Du et al. [8] and Huang et al. [11] reported that a blue-emitting PL band was originated from ionized oxygen deficient defect centers of the alumina membrane occurring in the wavelength range of 400-600 nm. The density of the oxygen defects in the alumina membrane was found to increase by increasing the depth of pore walls. Gao and his coworkers [13] suggested that the oxalic impurities rather than F^+ was responsible for blue luminescence at 470 nm observed in the alumina membrane. We could conclude with certainty that both studies are able to

explain significant variance of PL spectra. A thin dense alumina film without oxalic impurities forms after the aluminum foil is annealed at 673 K. The emission center of this dense alumina is observed only at the wavelength of 443 nm, which can be attributed to the oxygen defects. However, when the sample is anodized in oxalic acid solution, the other emission appears at around 470 nm which is in agreement with the results obtained from Gao et al. [13]. At the mean time, there is also the oxygen vacancies produced in the porous alumina membrane during the anodization process. The concentrations of the oxygen defects and the oxalic impurities are found to increase with increasing anodization time, and thus, the intensities of both peaks increase gradually. The experimental spectra of the porous alumina membranes have been deconvoluted by Gaussian functions into two emission bands, as showed in Fig. 4-9. The schematic diagram adequately describes the PL behavior in terms of three components, namely, the oxygen defects (A, located at 443 nm), the oxalic impurities (B, located at 470 nm) and the dense alumina of the substrate (C). The emission profiles of the porous alumina membranes with different thickness are observed to exhibit remarkable changes due to the combination of A, B and C curves. Although the emission intensity is amplified, the integrated emission contribution of two fitting peaks is invariable with the ratio of 1 to 1. Therefore, we propose that the PL emission band can be attributed to two sources, one at 443 nm is correlated with the oxygen vacancies and the other at 470 nm is originated from the oxalic impurities.
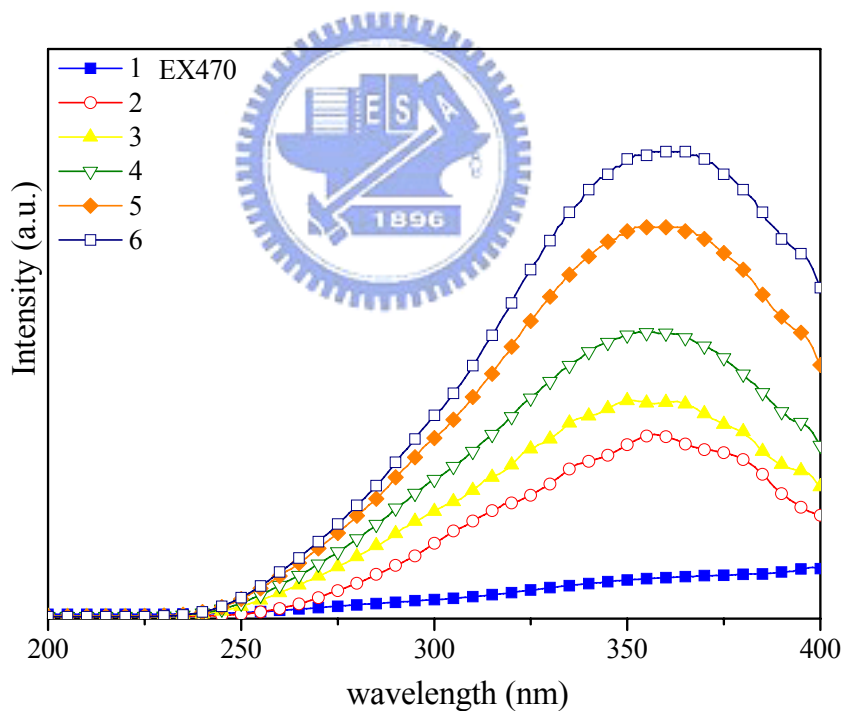
Fig. 4-8 PLE spectra monitored at 440 nm (a) and 470 nm (b) for the aluminum sheet
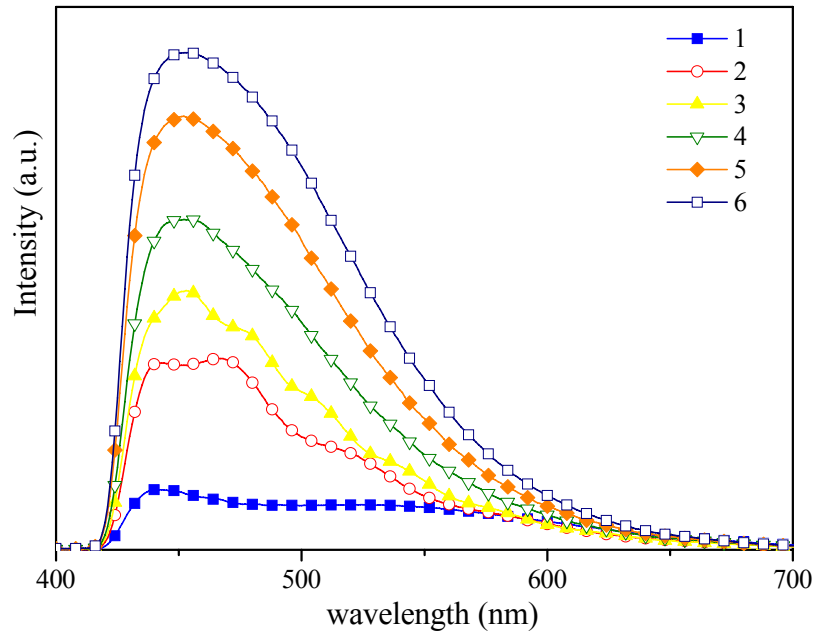and porous alumina membranes prepared in oxalic acid solution. 1: annealed
aluminum; 2: anodized 10 minutes; 3: anodized 15 minutes; 4: anodized
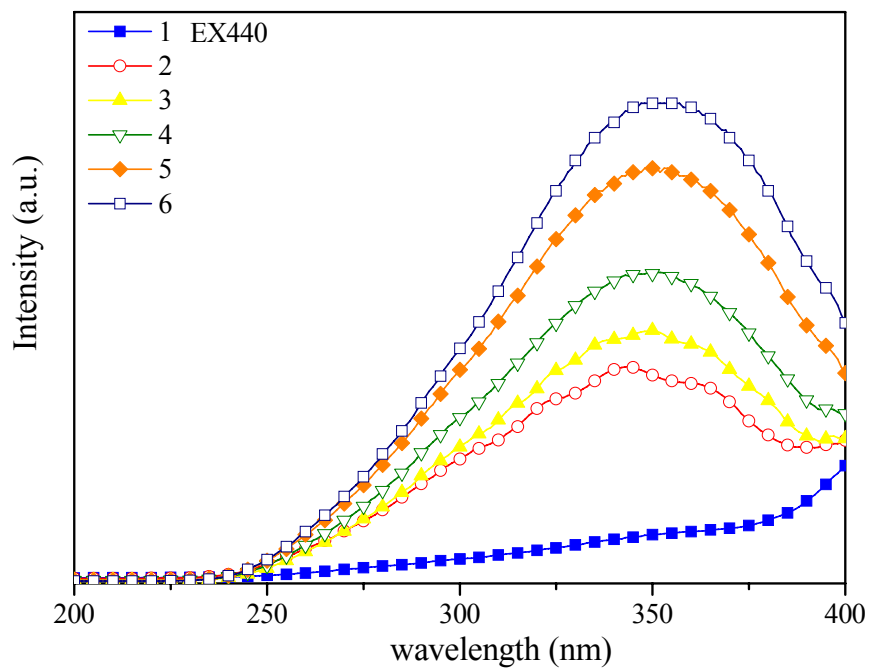20minutes; 5: anodized 40 minutes; 6: anodized 60 minutes.
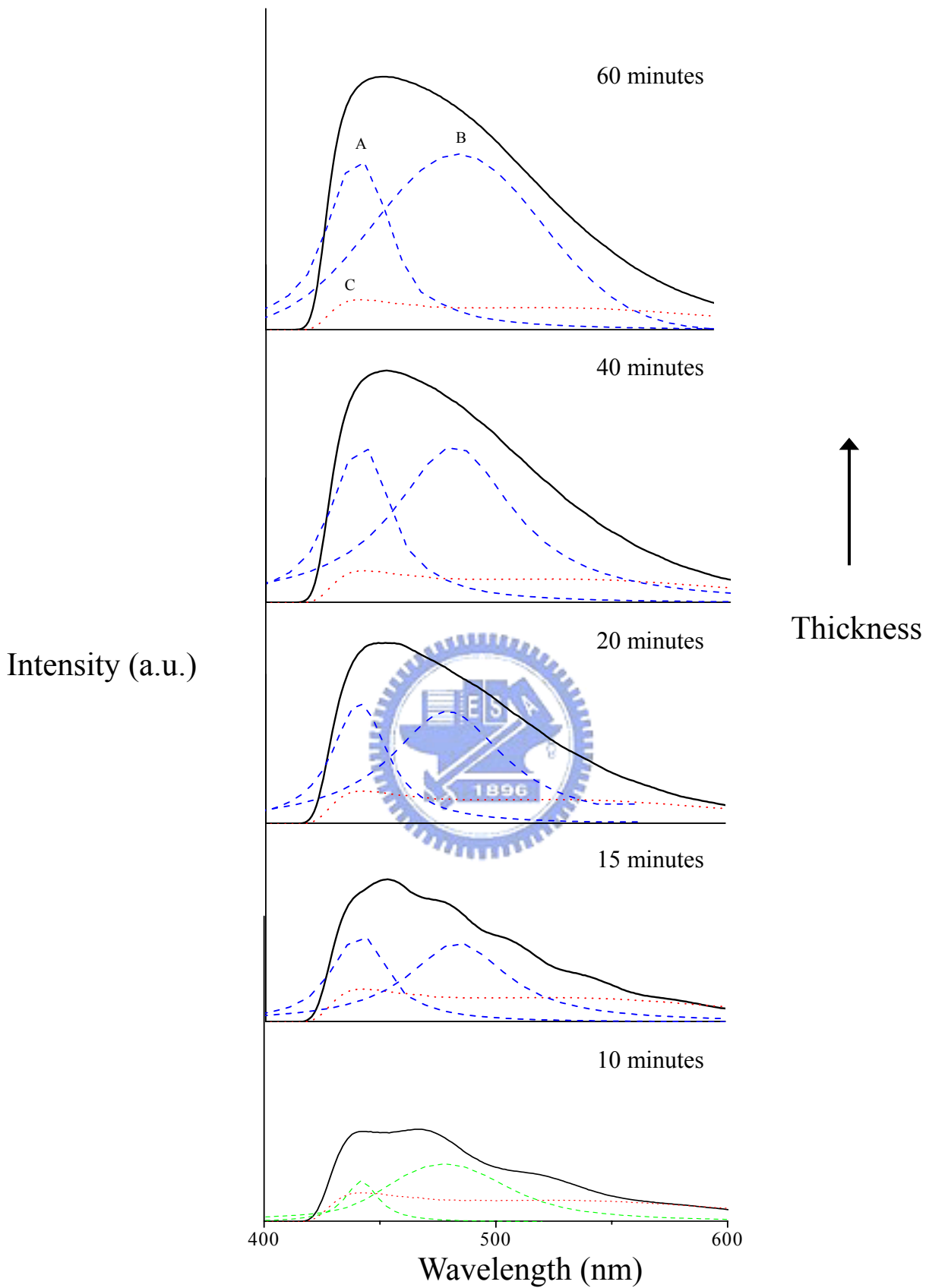
Fig. 4-9 Schematic diagram for PL curve of the porous alumina membranes whose

spectra have been deconvoluted by Gaussian functions (A and B curves) and

the dense alumina (C curve).

4.3.2 The effects of electrolytes and pore widening on the photoluminescence properties of porous alumina membranes

The PL spectra of the porous alumina membranes formed in 10 wt% sulfuric acid solution, 0.3 M oxalic acid solution, and 0.1 M phosphoric acid solution are shown in Fig. 4-10. It can be seen that under an excitation of the 365 nm using a Xe lamp, the membrane formed in oxalic acid displays a strong blue PL peak at 452 nm, while those formed in sulfuric acid solution, and phosphoric acid solution only have a weak emission around 443 nm. The PL properties of porous alumina membranes prepared in sulfuric acid solution and phosphoric acid solution are very similar to that of dense alumina. Therefore, we believe that the sulfuric and phosphoric impurities have less contribution, even no help to the emission band. These results also indicate that the electrolyte has a large influence on the light-emitting property of porous alumina membranes.
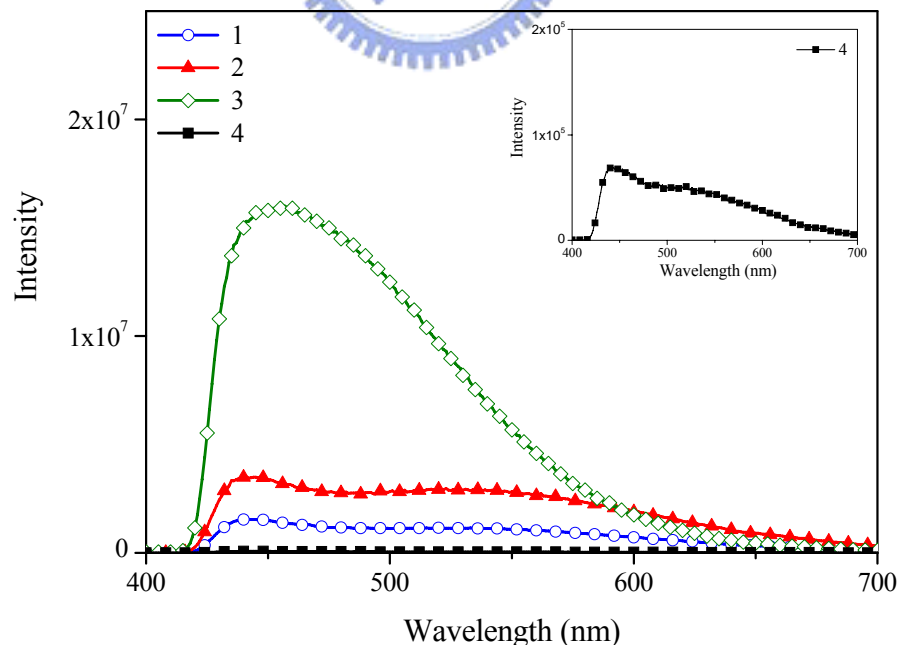
Fig. 4-10 PL spectra of the aluminum sheet and porous alumina membranes prepared in different acid solution, 1: annealed aluminum; 2: 10 wt% sulfuric acid; 3:

0.3 M oxalic acid; 4: 0.1 M phosphoric acid. The insert is an enlargement of the curve 4.
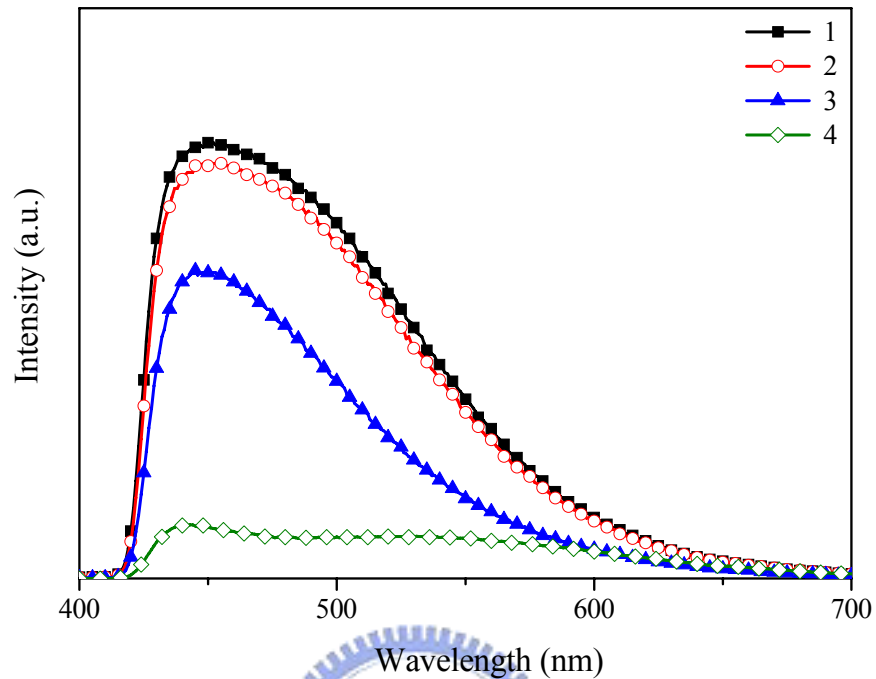
Fig. 4-11 PL spectra of porous alumina membranes prepared in oxalic acid solution, 1: as prepared sample; 2: pore widening 30 minutes; 3: pore widening 60 minutes; 4: pore widening 120 minutes.

The effect of pore widening by chemical etching is investigated. Figure 4-11 reveals that as the etching time of membranes immersed in phosphoric acid solution increases, the PL intensity shows a tendency to decrease. Figures 4-12 (a)-(d) show that the surface morphologies of porous alumina membranes with the different level of etching in phosphoric acid solution. Based on the model for the porous alumina structure researched by Ono et al. [78], the pore wall of the porous alumina membranes consisted of an inner oxide layer composed of pure alumina and an outer oxide layer. The outer oxide could also divide into two parts, an outermost oxide close to the electrolyte and an intermediate oxide next to the inner oxide layer. Choi et al.

[79] suggested a distribution of anions in the duplex oxide layers of the porous alumina wall when the alumina was anodized in phosphoric acid solution. Anions and anion incorporated compounds were gathered in the intermediate part of the outer oxide. In this work, the intensity of the emission band decreases slightly when the etching time reaches thirty minutes. The SEM image (Fig. 4-12 (b)) shows the outermost oxide of alumina wall is removed at this moment. As the etching time increases to an hour, the blue shift of PL emission appears obviously from 455 nm to 445 nm, as indicated in Fig. 4-13. In the meanwhile, the intensity of the emission band declines gradually. These phenomena occur because of a large consumption of the most anions or impurities in the intermediate oxide over this period. When the most parts of the porous alumina are removed (Fig. 4-12 (d)), the intensity of the emission band drops abruptly and the peak has a slight blue shift to 443 nm behaved as the dense alumina. From Fig. 4-13, the distance from the pore center to the pore wall increases with the pore widening time. It can be seen that a large blue shift occurs when the intermediate part of alumina is removed. That means the PL contribution of oxalic impurities whose emission peak centered at 470 nm disappear mainly at this region.

According to the results, it can be suggested that only oxalic impurities could be emission centers in the porous alumina membranes. The distribution of oxalic impurities in this work is in agreement with pervious researches and variations in amount of oxalic impurities would have a strong influence on the emission intensity.
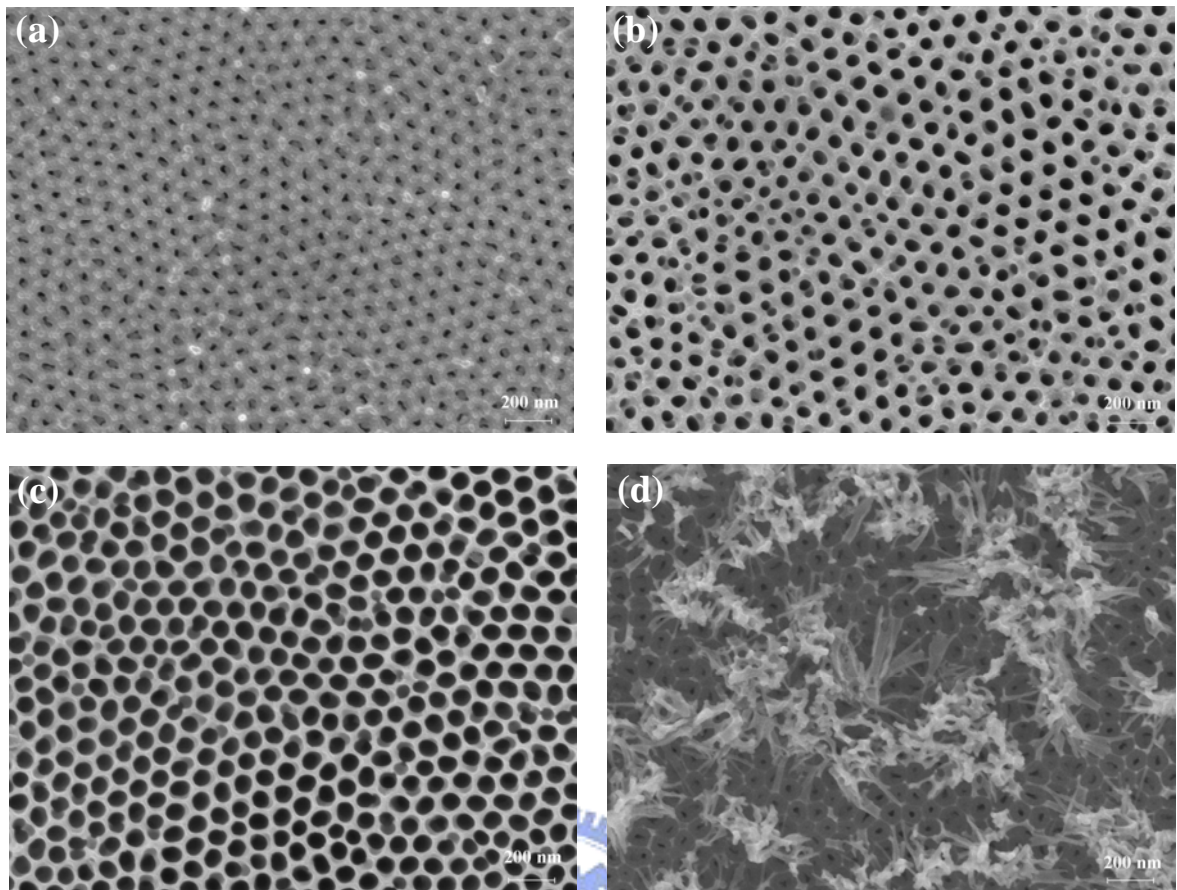
Fig. 4-12 SEM images of porous alumina membranes were formed in oxalic acid solution with different etching time: (a) 0 minute, (b) 30 minutes, (c) 60 minutes, and (d) 120 minutes.
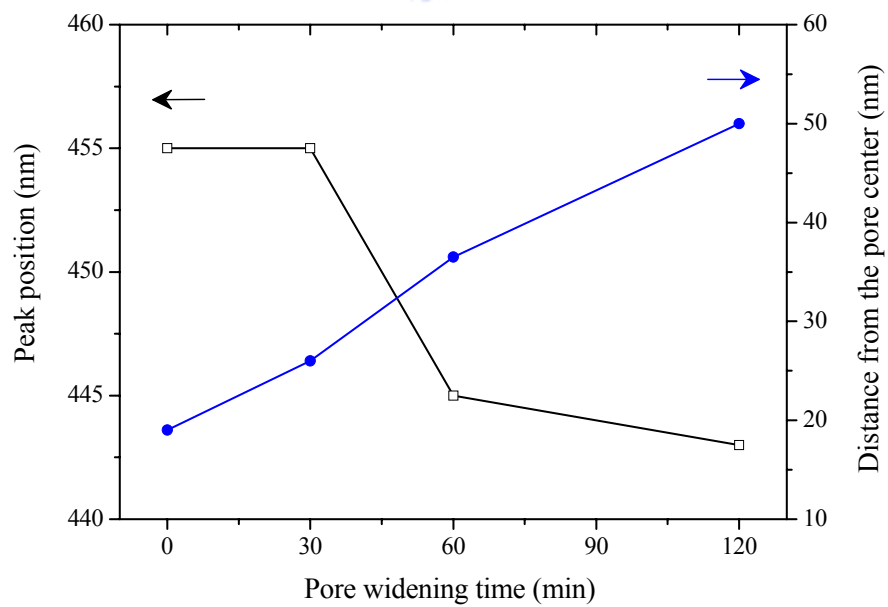
Fig. 4-13 The variations in the PL peak position and the distance from the center of the nanopore at the different pore widening time.

4.4 Summary

Porous alumina membranes were produced by adopting a two-step anodization process in sulfuric acid solution, oxalic acid solution, and phosphoric acid solution. X-ray analyses show that the prepared alumina membranes are amorphous phase. As indicated by the PL emission spectra, the intensity of PL band increases with increasing thickness of alumina membranes determined from SEM figures. The emission wavelength shifts from 443 nm to 443 nm and 470 nm, and finally located around 452 nm as the thickness of porous alumina membranes increases. A part of the explanation for these may lie in the fact that there are two emission centers caused by oxygen vacancies and oxalic impurities in the PL band. According to deconvolution of the PL spectra, both centers contribute greatly to the PL emission band. Finally, the effects of electrolytes and pore widening on PL properties of alumina membranes are also investigated. The alumina membrane prepared only in oxalic acid solution has a strong blue emission band. According to experiments of pore widening, a distribution of oxalic impurities in the porous alumina wall can be found to correspond to the previous researches. This study has taken a step in the direction of defining the relationship between the thickness and the photoluminescence in porous alumina membranes as well as the effects of process conditions.

Chapter 5 Fabrication and properties of PbS nanocrystals

5.1 Motivation

Semiconductor nanocrystals exhibit electronic, magnetic, optical, physical and chemical properties greatly differing from those observed in the corresponding bulk materials [80-82]. Because the size dependence of the band level in the semiconductor crystals results in a shift of the optical spectrum, quantum mechanical descriptions of the shift have been carried out by several researches [49, 83-85]. These interesting size effects occur on the nanoscale, allowing tunable optical properties of the nanostructure. Devices and applications make use of such properties like fast optical nonlinearity, high luminescence efficient and single electron transfer, as well as the potential applications in solar energy.

Most metal sulfides, such as PbS, ZnS, CdS, CuS......, belong to non-organic optical materials. Those materials have been known and investigated for a long time [86-90]. PbS is a IV-VI group semiconductor, which has attracted great attentions for the study of quantum confinement effect. PbS has a direct narrow band gap and a small effective mass combining to allow wavelength turning in a broad range [63]. This material is potentially useful in versatile applications like solar cell [91-92], optical switches [93] and light emitting diodes.

When the nanocrystals aggregate together, the quantum effect would decrease or disappear. Therefore, an important issue in the investigation and application of nanoparticles is how to assemble and disperse individual nanoparticles in a fast and controllable way. In this chapter, a novel process to fabricate PbS nanocrystals in the porous alumina membrane with the ordered arrays and the uniform size is offered. PbS nanocrystals were formed by using Pb nanowires reacted with sulfur vapor or

hydrogen sulfide (H₂S) gas. Firstly, we describe that how to fabricate Pb nanowires by casting process, characterize theirs properties, and discuss the formation mechanism of Pb nanowires. And then this experiment explores the reaction conditions controlling the agglomeration of the PbS nanocrystals. The nanocrystals produced in this process can be dispersed well in the alumina membrane. The photoluminescence properties and growth mechanism of PbS nanocrystals are also investigated. In addition, this process could be more suitable to produce the large area PbS nanocrystals without aggregation on/in porous alumina membranes. The results of this research may lead to a better understanding of PbS in nano-scale.

5.2 Microstructure and characterization of Pb nanowires

Figure 5-1 shows that the plane views of Pb nanowires with the diameters of 20, 80, 200 and 300 nm fabricated by the pressure casting procedure are uniform distributions and have high filling ratios. TEM images of nanowires with diameters of 20 nm and 80 nm are displayed in Figs. 5-2 (a) and (b), respectively. The bright field image suggests a uniform and without branches wire structure. The insert is the corresponding selective area electron diffraction (SAED) of the Pb nanowire. According to index of the SAED, the nanowire is a single-crystal structure growing along [110] direction. TEM micrographs as presented in Figs. 5-2 (c) and (d) show that interrupted wire structures like grain boundary appear when the diameters of the nanowires are 200 nm and 300 nm. In the casting process, the mold shape and material also affect the characteristics of the crystals such as orientation, shape, composition and perfection. The alumina membranes with pore diameters larger than 200 nm synthesized in the phosphoric acid solution have the less order and regular pore structures. The cross-section image of the alumina membrane with diameter 200 nm reveals that there are some defects like branches, interrupted and deformed

channels, as shown in Fig. 5-3 (a). The imperfect regions may induce the changes of heat flow direction or offer preferably nucleated sites during the solidification process. Therefore, polycrystals would grow more possibility in these nanowires. Figure 5-3 (b) is the cross-section image of the alumina membrane whose pore diameter is 80 nm. Since the nanochannel is straight and uninterrupted, the wire solidified in it could form a single crystal structure as the result in Fig.5-2 (b).
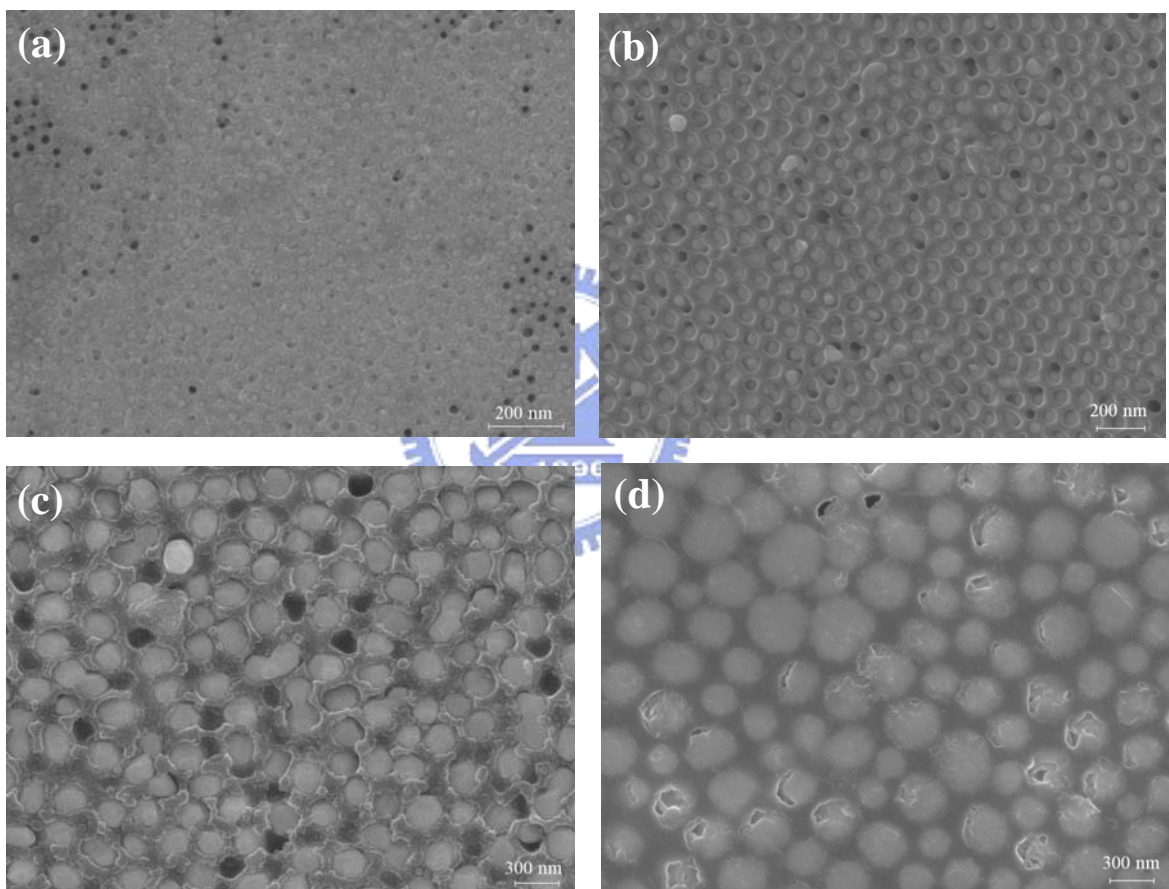
Fig. 5-1 SEM images of Pb nanowires with diameters of 20 nm (a), 80 nm (b), 200 nm (c) and 300 nm (d).
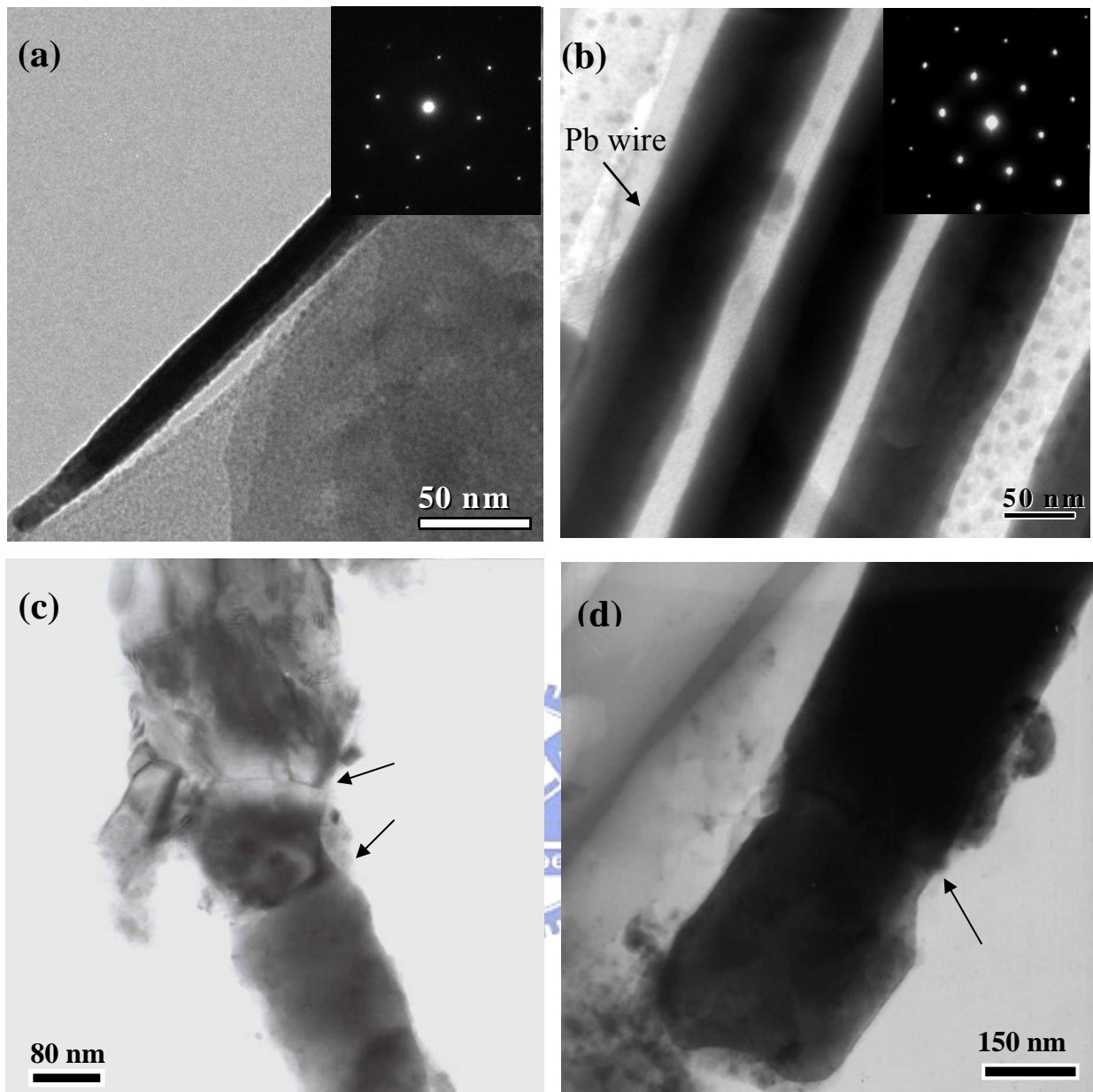
Fig. 5-2 TEM morphologies of the Pb nanowires with diameters of 20 nm (a) and 80 nm (b). The inserts in (a) and (b) are the selective area electron diffraction pattern of the corresponding Pb wire. (c) and (d) are the TEM images of the Pb nanowires with diameters of 200nm and 300nm, respectively. The grain boundaries are indicated by arrows.
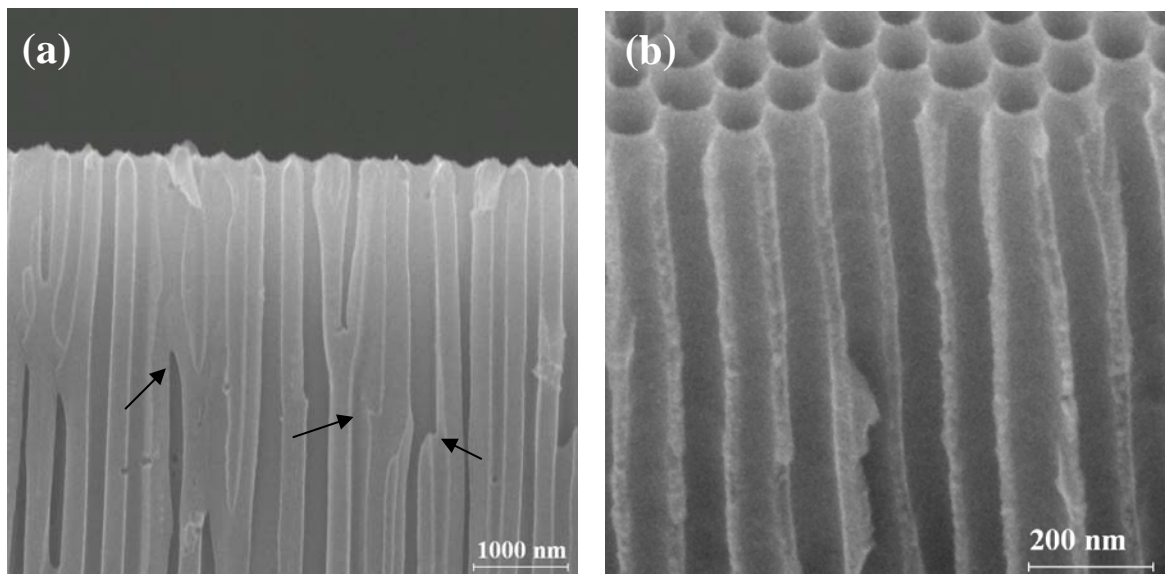
Fig. 5-3 The cross-section images of the porous alumina membrane with pore size
about 200 nm (a), and 80 nm (b).
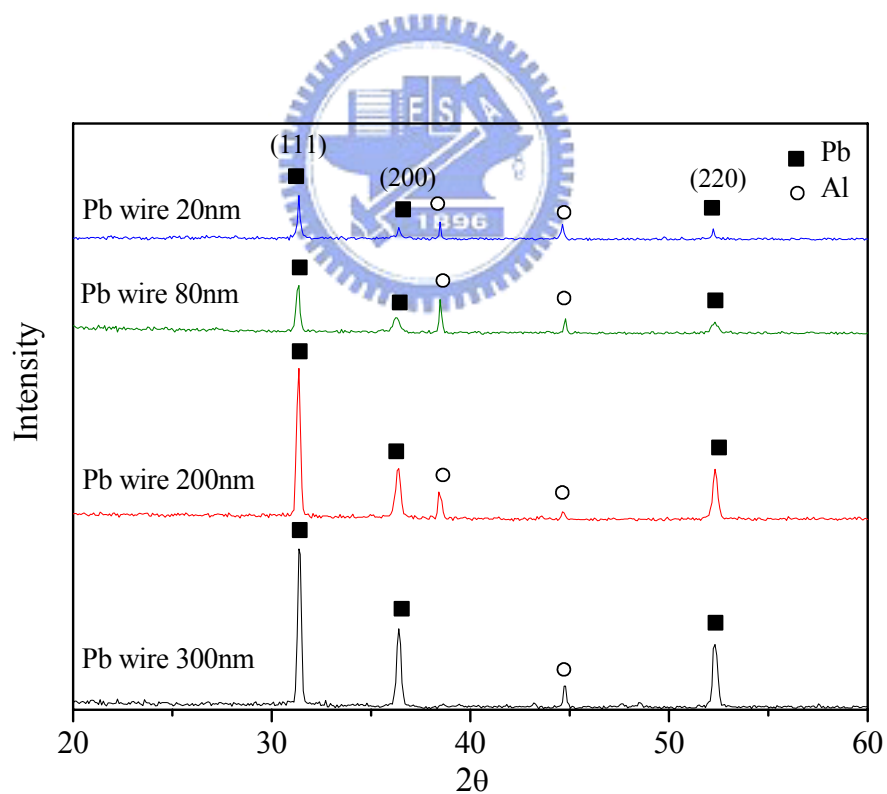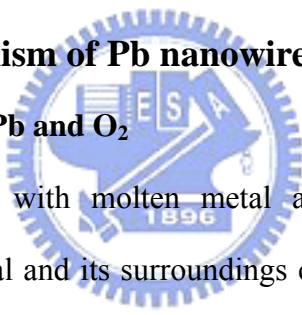
Fig. 5-4 The X-ray diffraction spectra of Pb nanowires with 20, 80, 200, and 300 nm
average diameter.

The results of the X-ray diffraction analyses of Pb nanowires with four different wire diameters are shown in Fig.5-4. Three peaks of the Pb nanowires identified as (111), (200) and (220) are the same as the peaks of Pb bulk with a face-centered cubic structure [94-95]. The major crystal plane of Pb nanowires with different diameters are the (111) lattice planes. The relative line intensities of $I_{(200)} / I_{(111)}$ are estimated. The intensity ratio reduces as the Pb wire diameter decreases. It can be known that nanowires produced by the pressure casting process usually possess high crystallinity and a preferred crystal orientation especially for the nanowires with smaller diameters; moreover, the crystal structure of bulk is preserved in the nanowires after heating and high pressure processes.

5.3 Formation mechanism of Pb nanowires

5.3.1 Reactions between Pb and O_2

Casting begins with molten metal and many reactions that occur between molten metal and its surroundings can lead to defects in the casting process. Oxygen and molten metal often react to produce metal oxides. These oxides usually comprise the dross or slag with other impurities and can be trapped in the casting to impair surface finish and mechanical properties. The oxides would float to the surface of the liquid metal and raise more difficulties during pouring the mold especially for nano-scale casting. Therefore, it is an important issue to minimize the oxidation of the molten metal before casting. Here we discuss the reactions between lead and oxygen first.

According to the available thermodynamic data [96], there are three metal oxides, PbO, PbO_2 and Pb_3O_4, in this system. The possible reactions for lead oxide formation are:

$$Pb_{(s,l)} + \frac{1}{2}O_{2(g)} \rightarrow PbO_{(s)} \quad (5\text{-}1)$$

$$Pb_{(s,l)} + O_{2(g)} \rightarrow PbO_{2(s)} \quad (5\text{-}2)$$

$$3Pb_{(s,l)} + 2O_{2(g)} \rightarrow Pb_3O_{4(s)} \quad (5\text{-}3)$$
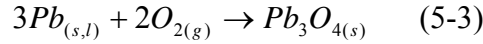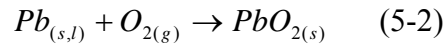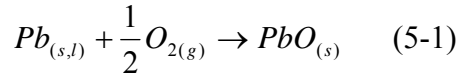
In the aspect of thermodynamics, any reaction for which the change in Gibbs free energy is negative should be favorable or spontaneous. The Gibbs free energy expression is given by the following equations:

$$\Delta G^0 = \Delta H^0 - T\Delta S^0 \quad (5\text{-}4)$$

$$\Delta G^0 = -RT \ln K = -2.303RT \log K \quad (5\text{-}5)$$

Where ΔG^0 is the standard state Gibbs free energy change of a reaction; ΔH^0 is the change in enthalpy; T is the absolute temperature; ΔS^0 is the change in entropy; R is the gas constant, and K is the equilibrium constant. All the presently observed reactions and their relevant thermodynamic data are listed in table 5-1. The magnitude of ΔG^0 would tell us how far the standard state is to equilibrium. Figure 5-5 presented the relationship between the change in Gibbs free energy and the temperature reveals that the most stable reaction in this system is the reaction 5-3. In addition, the equilibrium constant K of the reaction 5-3 can be expressed as:

$$\log K = -3 \log a_{Pb} - 2 \log P_{O_2} = -19.634 + \frac{37349.738}{T} \quad (5\text{-}6)$$

where a_{Pb} is the activity of Pb and P_{O_2} is the partial pressure of the oxygen. Since the activity of Pb is unity, the relationship between the partial pressure of the oxygen and temperature is shown in Fig. 5-6. As indicated in Fig. 5-6, the partial pressure of oxygen needed markedly grows as the temperature increases and the Pb_3O_4 can always exist until the partial pressure of oxygen is less than $10^{-21.26}$ atm at 600 K (the melting point of lead). In other words,

avoiding the formation of the oxide is much more difficult to achieve. Therefore, enhancing the reaction temperature and keeping the chamber in the high vacuum is necessary for reducing the occurrence of the oxidation.

Table 5-1 Thermodynamic data of the Pb-O reactions.

Reaction	ΔG^0 (kJ)	$\log K$
$Pb_{(s,l)} + \dfrac{1}{2}O_{2(g)} \rightarrow PbO_{(s)}$	$-218.104 + 0.099T$	$-5.183 + \dfrac{11419.057}{T}$
$Pb_{(s,l)} + O_{2(g)} \rightarrow PbO_{2(s)}$	$-273.230 + 0.194T$	$-10.157 + \dfrac{14305.235}{T}$
$3Pb_{(s,l)} + 2O_{2(g)} \rightarrow Pb_3O_{4(s)}$	$-713.380 + 0.375T$	$-19.634 + \dfrac{37349.738}{T}$
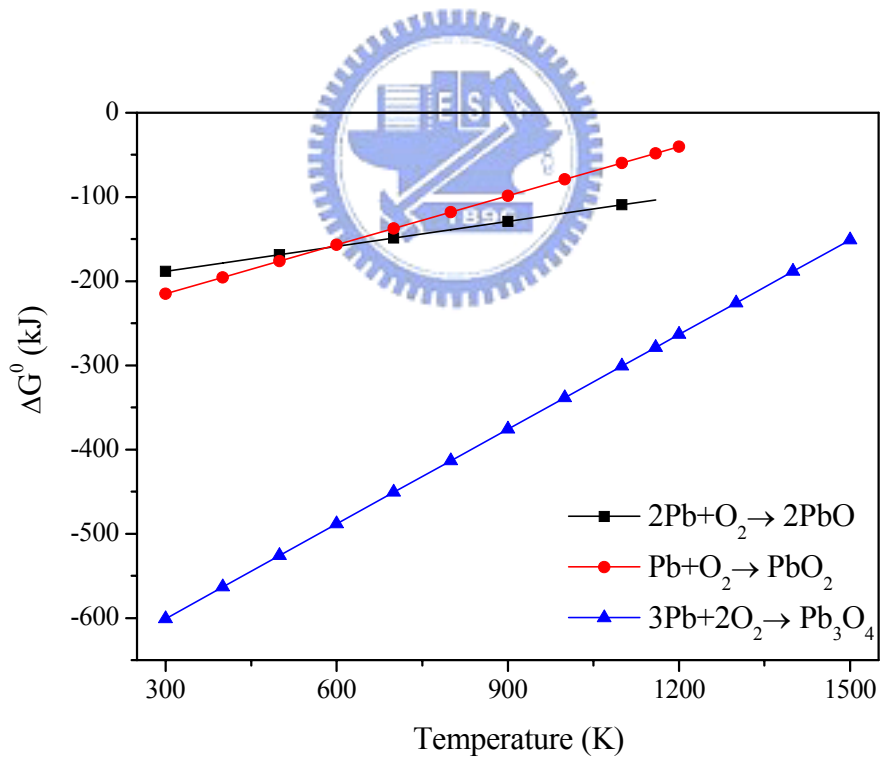
Fig. 5-5 Relationship between the change in Gibbs free energy and the reaction temperature.
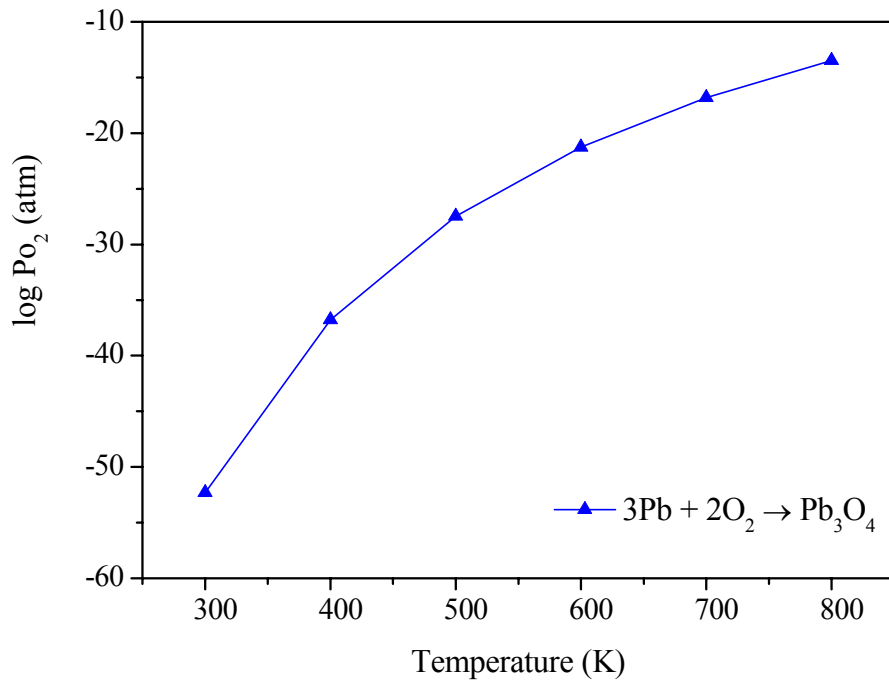
Fig. 5-6 Relationship between the partial pressure of the oxygen and the temperature

in the reaction: $3Pb_{(s,l)} + 2O_{2(g)} \rightarrow Pb_3O_{4(s)}$.
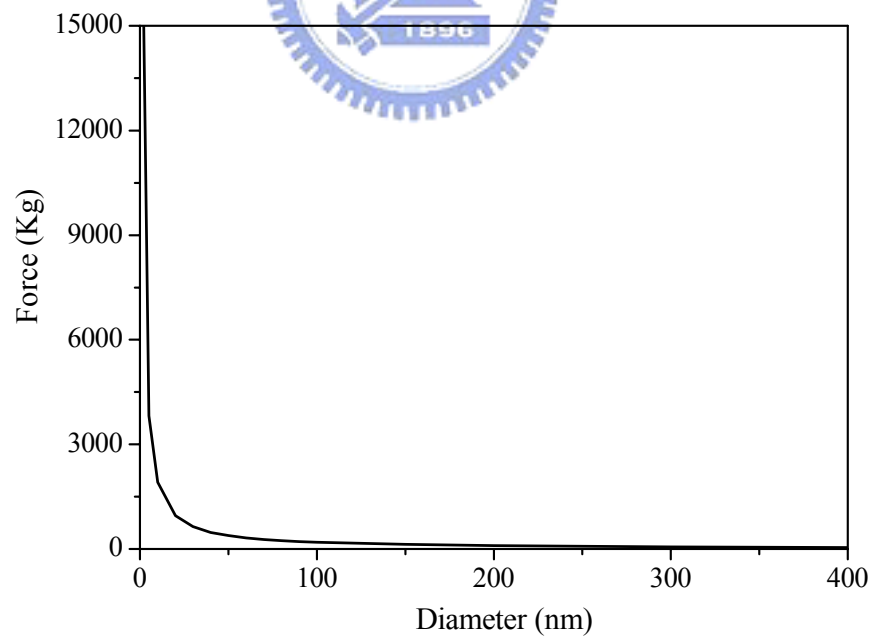
Fig. 5-7 The curve of required force with pore diameter when Pb melt is injected into

the nanochannel.

5.3.2 Casting process of Pb nanowires

In the casting process, the molten Pb metal is injected into the porous alumina membrane forming metallic nanowires. The required force for Pb melt into nanochanel is proportional to the surface tension of the melt. The pressure for melt injection into nanochannel can be evaluated as [97-98]:

$$\Delta P = \frac{F}{A} = \frac{-(2\gamma\cos\theta)}{r} \qquad (5\text{-}7)$$

Where F is the normal force; A is the area of specimen; r is the radius of nanochannel; γ is the surface tension of Pb melt, and θ is the contact angle between the Pb melt and the porous alumina membrane. In this experiment, the surface tension of Pb melt is 468 dyne/cm [99], A is 1 cm^2 and the contact angle assumes the least favorable case of complete nonwetting ($\theta = 180^0$). This is because liquid metal/ oxide systems mostly have non-wetted ($\theta > 90^0$) and non-reactive wetted conditions. Moreover, the contact angle would be greater in a rough surface than in a corresponding flat surface [100]. Therefore, the required force to inject the Pb melt into nanochannels with different diameters could be calculated. Figure 5-7 shows the relationship between the diameter of the nanochannel and the required force. It can be seen that the force is inversely proportional to the diameter of the nanochannel and getting smaller nanowires needs to apply larger hydraulic force. The critical force of forming the Pb nanowire with a diameter of 20 nm is counted as 955 kg. As discussed above (section 5.3.1), an oxide film is easily produced on the surface of Pb melt even if the vacuum maintains at 10^{-6} Torr. The oxide film would increase the difficulty of the casting process. Furthermore, the metal oxide usually has well mechanical properties and high melting temperature. The oxide has to be broken when the Pb melt is poured

into nanochannel. In the meanwhile, it is essential to increase the filling ratio of Pb nanowires as far as possible. For these reasons, the force used in this experiment is several times as the theoretical value.

5.3.3 Growth model of Pb nanowires

In the solidification process of pure metals, the solid phase will nucleate and grow in the melt. The nucleation of the solid phase should be homogeneous, but in actuality it is usually heterogeneous because less energy is added to the system if nuclei form at an already existing solid-liquid interface. Nucleation is favored at the mold wall, because not only there is a solid-liquid interface presented, the liquid is usually cooler near the mold wall. Growth of the grain is by movement of the interface between solid and liquid. The grain structure and direction of grain growth are controlled by the temperature gradients at the solid-liquid interface. Therefore, the growth of high quality single crystals is quite difficult and requires a planar solid-liquid interface and a particular solidified direction which is anti-parallel to that of the heat flow. That is, the formation of cells or dendrites must be avoided, and a sufficiently high thermal gradient or a sufficiently low growth rate will lead to the plane front growth. The temperature gradient (G) at the interface defines as:

$$G = dT/dZ \qquad (5-8)$$

Here, Z is the coordinate with respect to the movement of the solid/liquid interface. It can be found that the solid-liquid interface of a pure metal will be more stable if the temperature gradient is positive (G>0). Growth rate (V) means the movement rate of the solid-liquid interface and can be described by the following equation:

$V = dZ / dt$ (5-9)

The ratio, G/V, determines the solidification morphology (planar, columnar and dendritic). The product of G and V is equal to the cooling rate which controls the scale of the microstructures [101-102].

In this experiment, after nanochannels are filled with Pb melt, a solidification process proceeds immediately using the water cooling method. Heat loss from the bottom of the wire is often a sufficient heat sink. Solidification proceeds from the bottom of the wire to the top region in this experiment. The schematic diagram of the solidification is shown in Fig. 5-8.
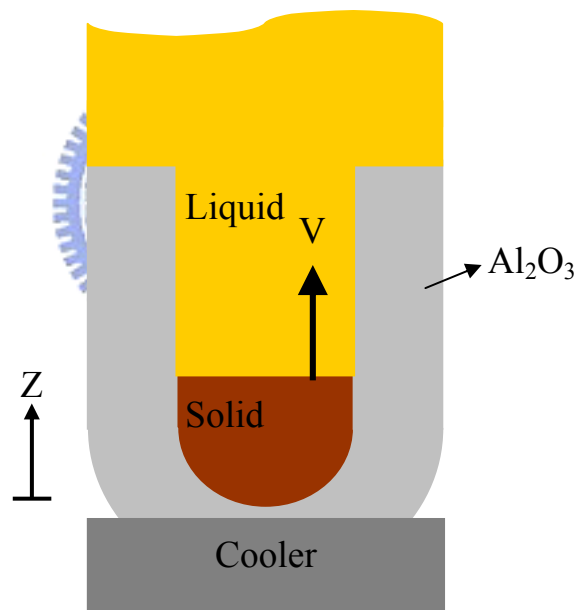
Fig. 5-8 Schematic illustration of the the Pb nanowire solidification model. Here, Z is the coordinate with respect to the moving solid-liquid interface and V is the rate of the movement of the solid-liquid interface.

One must suppose that the steady stable condition for the temperature gradient through the specimen is applicable. There is a constant temperature gradient, a uniform growth rate and a highly uniform microstructure

throughout the wire. The temperature difference between the top and bottom of the wire is about 500 K. The length of the wire is 10 μm and the total cooling time is 10 minutes. Therefore, G and V can be estimated to be 5×10^7 (K/m) and 1.67×10^{-8} (m/s), respectively. Due to the high G/V value and the directional solidification opposite to the direction of heat flow, solidification with a planar interface could occur and the individual nanowires with different diameters are believed to be single crystal structures.

5.4 Thermodynamic calculation for Pb-S system

In the light of thermodynamics, there are eighth equations describing the production of PbS when Pb reacts with sulfur vapor. The vapor composition is a mixture of several sulfur species including $S_{1(g)}$, $S_{2(g)}$, $S_{3(g)}$, $S_{4(g)}$, $S_{5(g)}$, $S_{6(g)}$, $S_{7(g)}$, and $S_{8(g)}$ [103]. All the presently observed reactions and their relevant thermodynamic data are listed in table 5-2. The thermodynamic stabilities of reactions in the Pb-S system are evaluated by considering their Gibbs free energy. Fig. 5-9 presents the relationship between the change in Gibbs free energy and the temperature. It also reveals that the most favorable reaction for PbS formation is:

$$Pb_{(s,l)} + S_{1(g)} \rightarrow PbS_{(s)} \qquad (5\text{-}10)$$
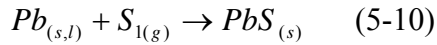
In this experiment, the reaction temperature is chosen as 573 K because that the Pb nanowire is still the solid phase at this temperature. According to the available reference [104], the vapor pressure of sulfur needed is about 0.1~0.2 atm close to the pressure of oxygen in the air. Based on the thermodynamic calculations, a high sulfur vapor pressure and a suitable temperature would facilitate the formation of lead sulfide.

However, there is a thorny problem appeared possibly. The nonreactive sulfur species in the vapor could deposit easily on the surface of the Pb nanowires. The sulfur depositions would prevent the Pb wire from reacting with the $S_{1(g)}$ gas.

In the other procedure, the reaction of PbS formation is described as following:

$$Pb_{(s,l)} + H_2S_{(g)} \rightarrow PbS_{(S)} + H_{2(g)} \qquad (5\text{-}11)$$
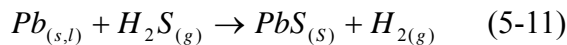
From the thermodynamics aspect, the Gibbs free energy can be written as,

$$\Delta G = -76.18 + 0.042T \quad [103] \qquad \text{kJ/mole} \qquad (5\text{-}12)$$

Based on the thermodynamic calculation as presented in Fig. 5-10, it is a spontaneous reaction as the temperature reaches 573 K and the reaction Gibbs free energy (G) is -52.11 kJ/mole. Therefore, all of the Pb nanowires would

transform into PbS crystals if the reaction time is long enough.

Table 5-2 Thermodynamic data of the Pb-S reactions.

Reaction	ΔG^0 (kJ)
$Pb_{(s)} + S_{(s)} \rightarrow PbS_{(s)}$	$-98.93 + 0.0065T$
$Pb_{(s)} + S_{(l)} \rightarrow PbS_{(s)}$	$-100.58 + 0.012T$
$Pb_{(l)} + S_{(l)} \rightarrow PbS_{(s)}$	$-109.11 + 0.026T$
$Pb_{(s,l)} + S_{1(g)} \rightarrow PbS_{(s)}$	$-376.47 + 0.143T$
$Pb_{(s,l)} + \frac{1}{2}S_{2(g)} \rightarrow PbS_{(s)}$	$-162.41 + 0.086T$
$Pb_{(s,l)} + \frac{1}{3}S_{3(g)} \rightarrow PbS_{(s)}$	$-145.29 + 0.062T$
$Pb_{(s,l)} + \frac{1}{4}S_{4(g)} \rightarrow PbS_{(s)}$	$-134.87 + 0.050T$
$Pb_{(s,l)} + \frac{1}{5}S_{5(g)} \rightarrow PbS_{(s)}$	$-120.53 + 0.035T$
$Pb_{(s,l)} + \frac{1}{6}S_{6(g)} \rightarrow PbS_{(s)}$	$-115.78 + 0.033T$
$Pb_{(s,l)} + \frac{1}{7}S_{7(g)} \rightarrow PbS_{(s)}$	$-115.12 + 0.032T$
$Pb_{(s,l)} + \frac{1}{8}S_{8(g)} \rightarrow PbS_{(s)}$	$-111.51 + 0.032T$

5.5 Microstructure and characterization of PbS nanocrystals

5.5.1 The morphologies and the XRD analyses of PbS nanocrystals via the reaction between Pb nanowires with 80 nm in diameter and S vapor

Pb nanowires with the porous alumina membrane and sulfur powders were sealed in a vacuum glass tube. The tube was put in a furnace with heat treatment at 573K for 3 and 8 hours. The sulfur vapor reacted with the Pb nanowires and the PbS nanocrystals were produced then. Figures 5-11 (a) and (b) shows the morphologies of the porous alumina membrane and Pb nanowires whose diameter around 80 nm fabricated by pressure casting process. The SEM images of the PbS nanocrystals with different sulfization time, 3 and 8 hours, are presented in Figs. 5-11 (c) and (d). The images indicate that the surface products increase obviously as the reaction time increases from 3 hours to 8 hours. The products in a disorderly pile on the surface and do not have smooth and regular patterns or shapes. The XRD analysis (Fig. 5-12) presents that the reaction of Pb and sulfur vapor associates with the time of heat treatment. The content of PbS in the specimen with heat treatment 8 hours is much higher than the one with heat treatment 3 hours. Moreover, the sulfur signals appear in both specimens. It means that the surface products could consist of PbS crystals and sulfur crystals. The result corresponds with the previous discussion in the section 5.4. The sulfur crystals are deposited from the nonreactive sulfur species. The existence of the sulfur depositions is the occasion of the surface roughness.
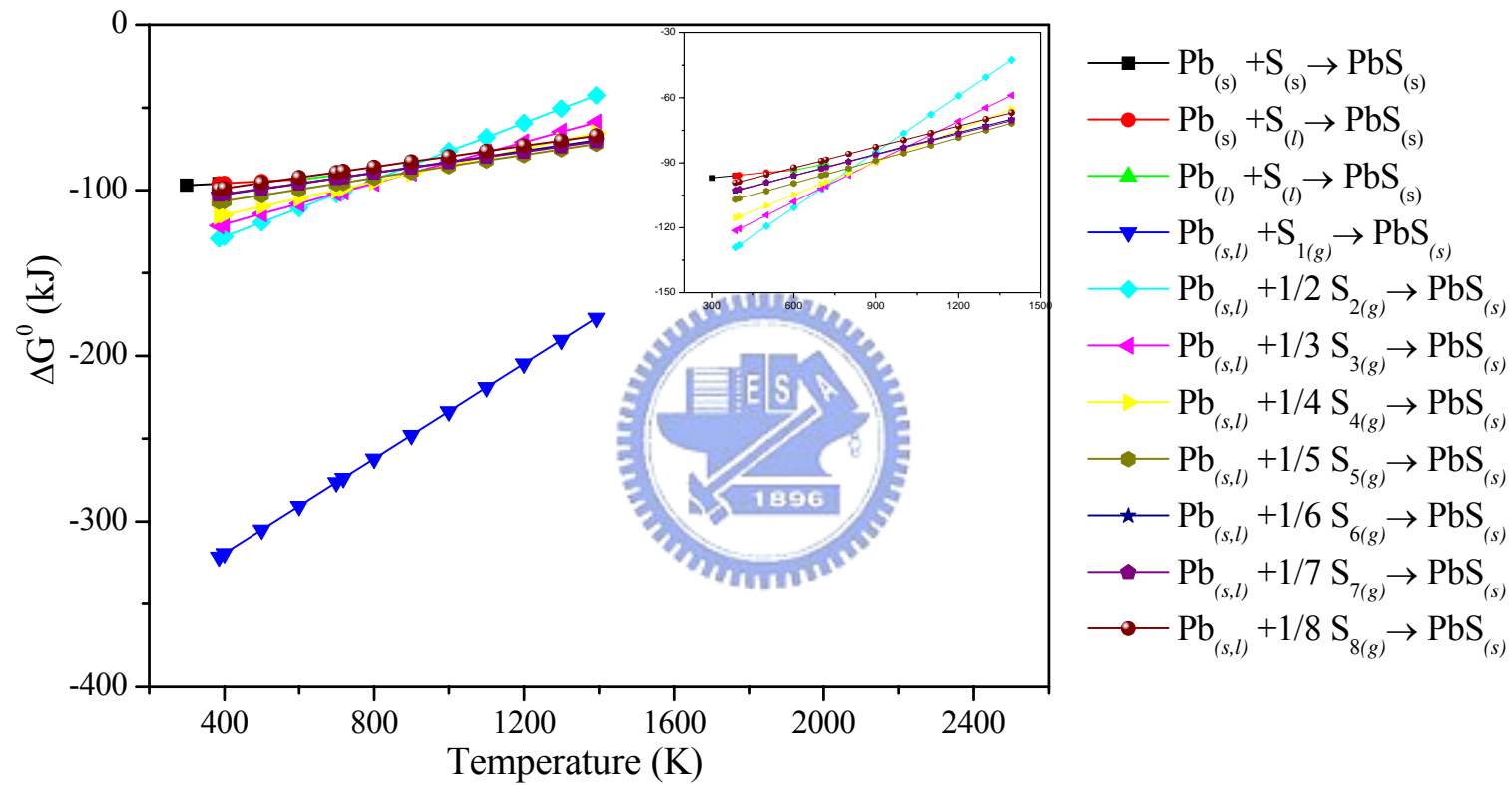
Fig. 5-9 The Gibbs free energies of various reactions forming PbS.
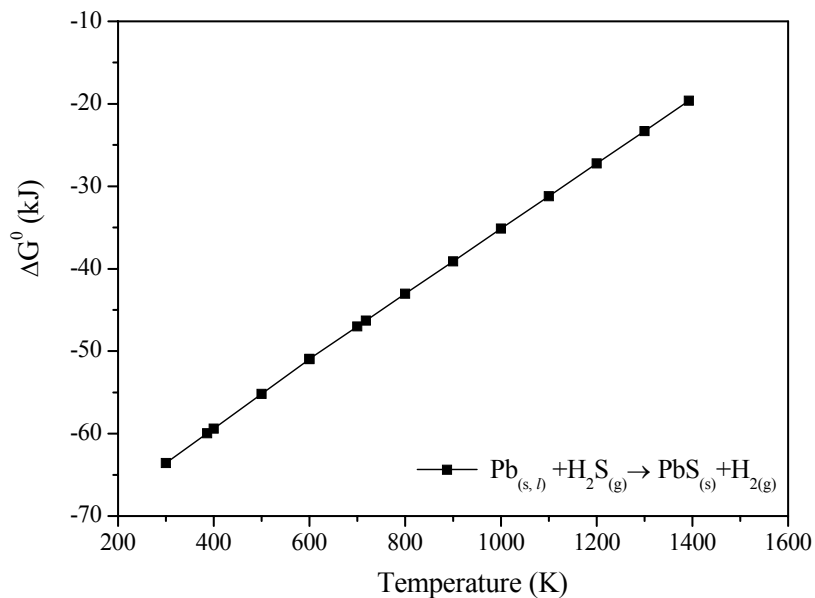
Fig. 5-10 Relationship between the change in Gibbs free energy and the reaction

temperature.
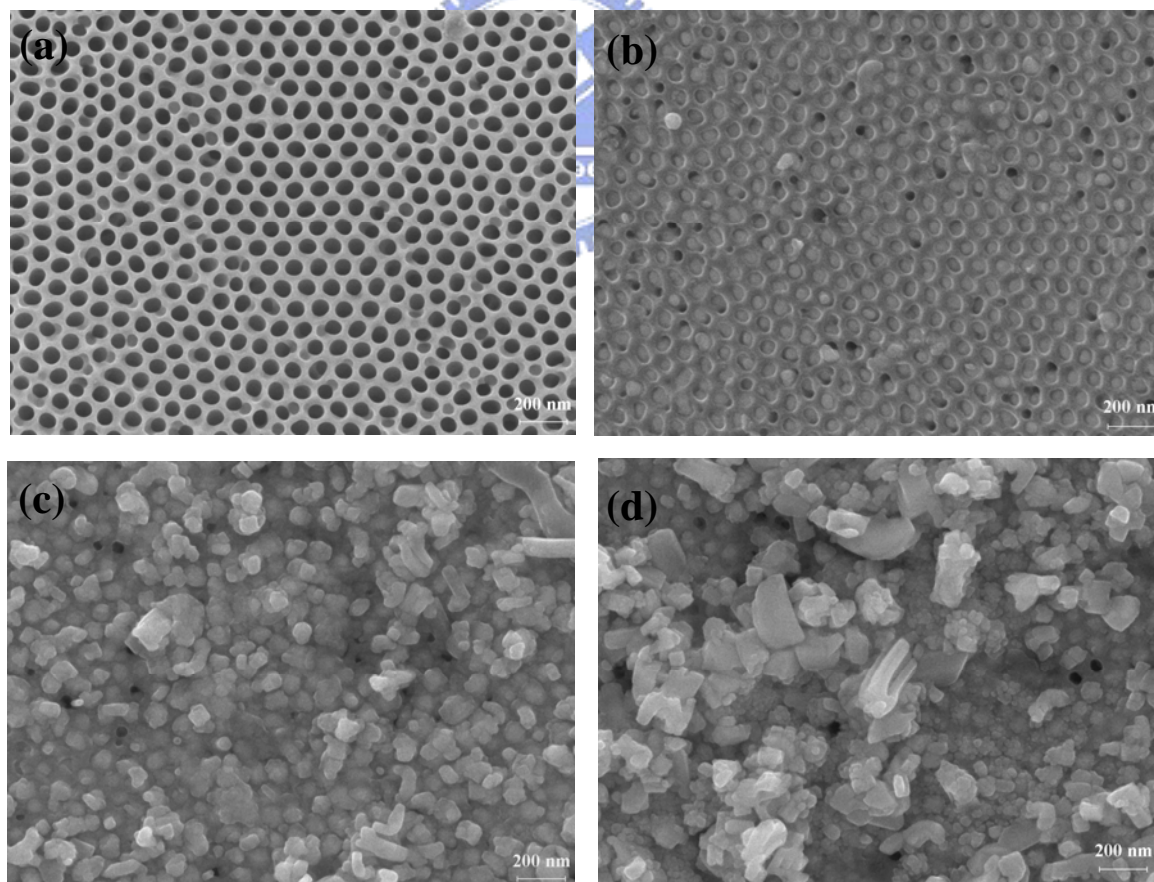
Fig. 5-11 (a) SEM image of a porous alumina membrane produced in 0.3 M oxalic

acid solution. (b) SEM image of Pb nanowires fabricated by vacuum

pressure injection process. The morphologies of the PbS nanocrystals prepared via the reaction between Pb wires and S vapor at various time: (c) 3 hours and (d) 8 hours.
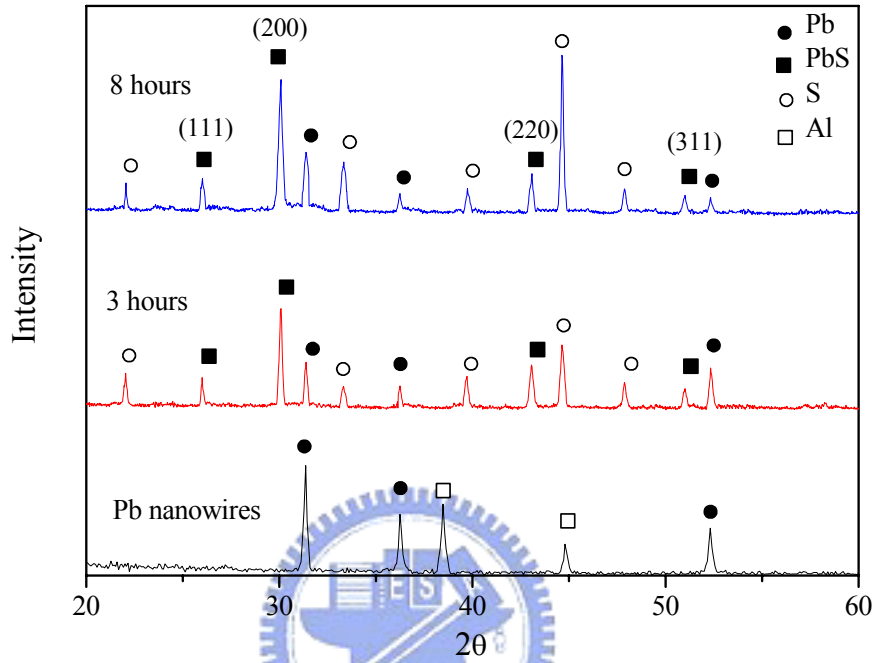
Fig. 5-12 X-ray diffraction profiles of Pb nanowires (80 nm) and PbS nanocrystals with different sulfization time (S vapor).

5.5.2 The morphologies and the XRD analysis of PbS nanocrysatls via the reaction between Pb nanowires with 80 nm in diameter and H$_2$S gas

A sulfization procedure with H$_2$S gas was proceeded to obtain PbS nanocrystals. The Pb nanowires were exposed to H$_2$S gas at different temperatures, 473 K, 573 K, and 673 K, for 8 hours. The morphologies of the different experimental conditions are shown in Figs. 5-13 (a)-(c). It can be seen that the PbS crystals grow into a film as the reaction temperature reaches 673 K which is higher than the melting point of Pb nanowires. When the Pb nanowires are sulfized at 473 K, the morphology does not have many changes compared with non-reacted Pb nanowires as presented in Fig. 5-13 (a). Therefore, the reaction temperature at 573 K is more appropriate for this procedure. Then, the reaction time varied from 3 hours to 8 hours as the Pb nanowires were heated up to a chosen temperature, 573 K. Figures 5-13(b), (d) and (e) are the PbS nanocrystals with various sulfization time and display that the PbS crystals would grow gradually into cubes as the reaction time increases. However, when the exposure time to H$_2$S gas is too long or the reaction temperature is too high, the formed PbS nanocrystals would aggregate easily on the surface of the porous alumina membrane. Therefore, controlling reaction conditions carefully is essential for the fabrication of PbS nanocrystals.

The XRD analysis in Fig. 5-14 shows that the PbS phase appears after the reaction of Pb and H$_2$S gas occurs. The PbS phase is identified to crystallize in cubic crystalline lattice (Fm3m, space group=225, JCPDS No.05-0592) with the lattice constant a = 0.59362 nm [94]. Atomic coordinates are (0, 0, 0) and (0, 1/2, 1/2) for Pb and (1/2, 1/2, 1/2) and (1, 1, 1/2) for S. The five peaks of PbS nanocrystals are the same as the (111), (200),

(220), (311), and (222) peaks of bulk PbS. In Fig. 5-14, the diffraction peaks of non-reacted Pb and Al substrate coming from the porous alumina template also exist simultaneously.
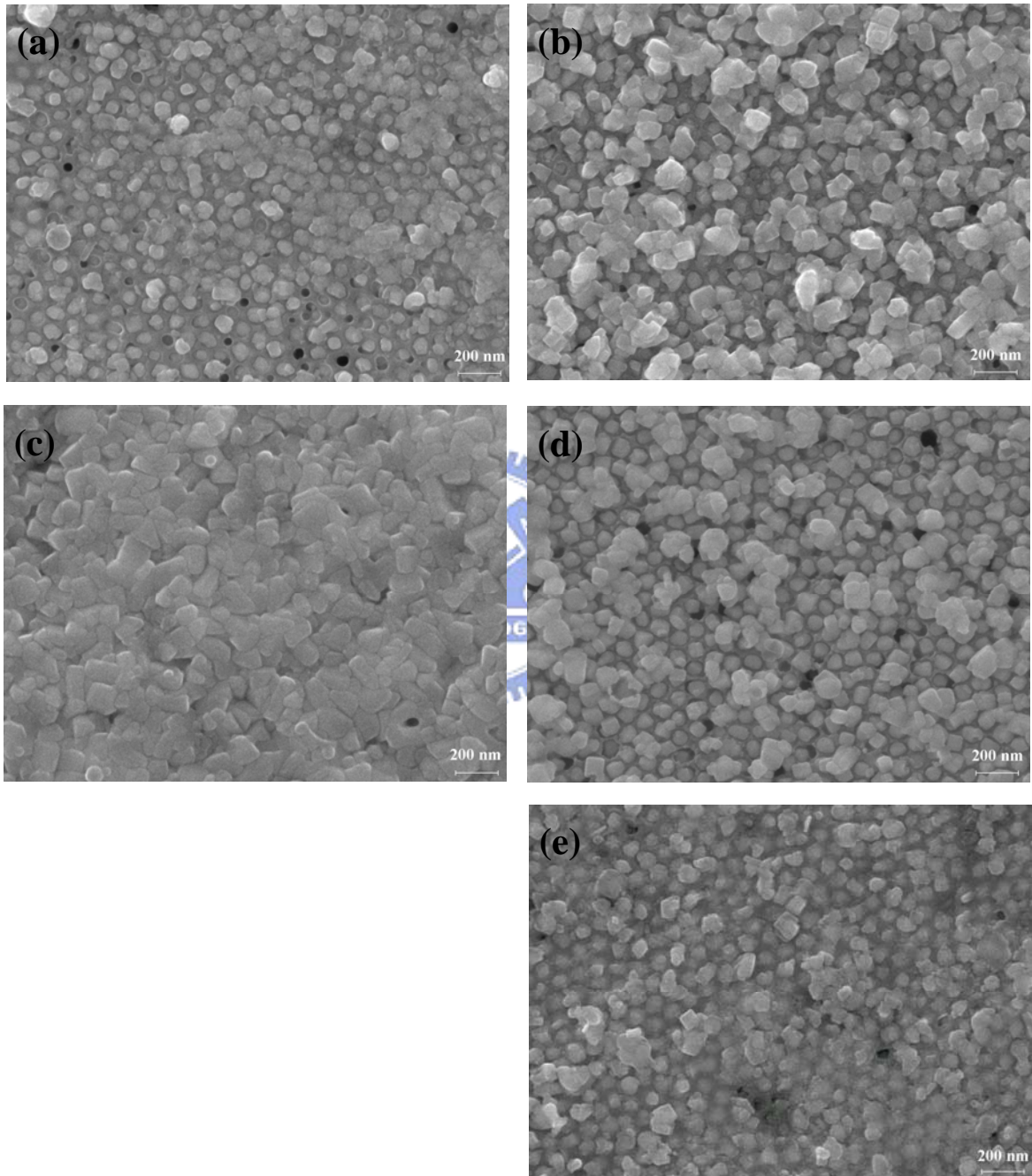
Fig. 5-13 SEM images of the PbS nanoparticles fabricated by sulfization process with H_2S gas: (a) 473 K 8 hours; (b) 573 K 8hours; (c) 673 K 8 hours; (d) 573 K 6 hours and (e) 573 K 3 hours.
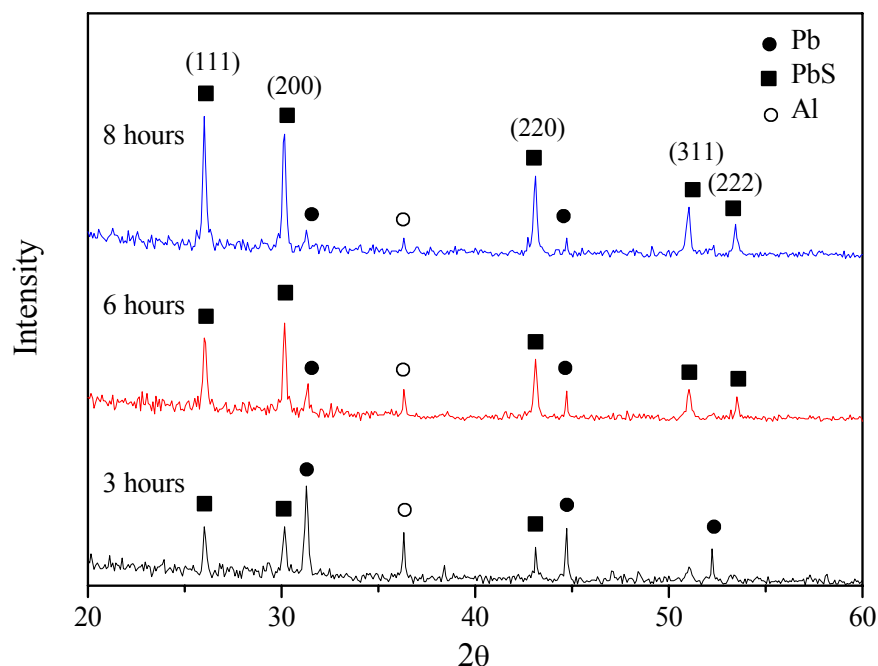
Fig. 5-14 X-ray diffraction profiles of Pb nanowires (80 nm) and PbS nanocrystals with different sulfization time (H_2S gas) at 573 K.

5.5.3 The microstructure and properties of PbS nanocrysatls via the reaction between Pb nanowires with 20 nm in diameter and H_2S gas

Figure 5-15(a) shows the surface morphology of nanoporous structure in the alumina membrane. As can be seen, the alumina membrane has a relative uniform pore diameter distribution with a mean pore size about 20 nm. The porosity of this membrane is counted as 16.49%. Using pressure casting process, Pb nanowires produce in the nanopores of the alumina membrane as shown in Fig. 5-15(b). The diameter of the nanowire is the same as that of the nanopore and the filling ratio of Pb wires is nearly 100%.

After the Pb nanowire arrays were fabricated, a sulfization procedure was proceeded to obtain PbS nanocubes. PbS nanocubes produced on/in the porous alumina membranes after the Pb nanowires exposed to H_2S gas at 573

K for 1 hour (Fig. 5-15 (c)), 3 hours (Fig. 5-15 (d)), 6 hours (Fig. 5-15 (e)), and 8 hours (Fig. 5-15 (f)), respectively. As the reaction time increases, the volumes of the PbS nanocubes on the alumina membranes increase obviously.

SEM and image analysis have been used in order to characterize the mean size and size distribution of PbS crystalline cubes. The SEM images of the PbS nanocubes (Fig. 5-15) are further analyzed with the Image-Pro Plus (IPP) software. The size distribution displays a single statistical ensemble of the PbS cubes as illustrated by the cube size histograms (Fig. 5-16). The average edge lengths in Figs. 5-16 (a)-(d) are 16.11 nm, 26.23 nm, 43.32 nm, and 55.64 nm respectively. An experiment formula for growth size of the PbS cubes has been work out. The edge length of the cube (L) and the sulfization time (t) are related according to $L = 10.57 + 5.44t$ as indicated in Fig. 5-17. The edge length of PbS cube grows at the rate 5.44 nm an hour. Therefore, the PbS cube size desired can be produced by controlling the sulfization time.

XPS spectrum can provide information about the element's chemical characteristics or oxidation state in a material and it measures the composition of the outermost 20~100 Å of a sample. Figure 5-18 shows the XPS elemental survey spectra of the as-prepared PbS sample surface. It is seen from Figs. 5-18 (a) and (b) that the PbS nanocubes show that the Pb4f spectrum is composed of two narrow peaks (Pb4f$_{7/2}$= 137.5eV, Pb4f$_{5/2}$= 142.3eV) and the binding energy of S2p peak is at 160.6 eV. Furthermore, the spectra in Figs. 5-18 (c) and (d) indicate an Al2p peak at 74.1 eV and an O1s peak at 531.5 eV. The results in Fig. 5-18 are in agreement with the values reported in literatures [105] and can be concluded that the as prepared sample is composed of PbS and Al$_2$O$_3$.
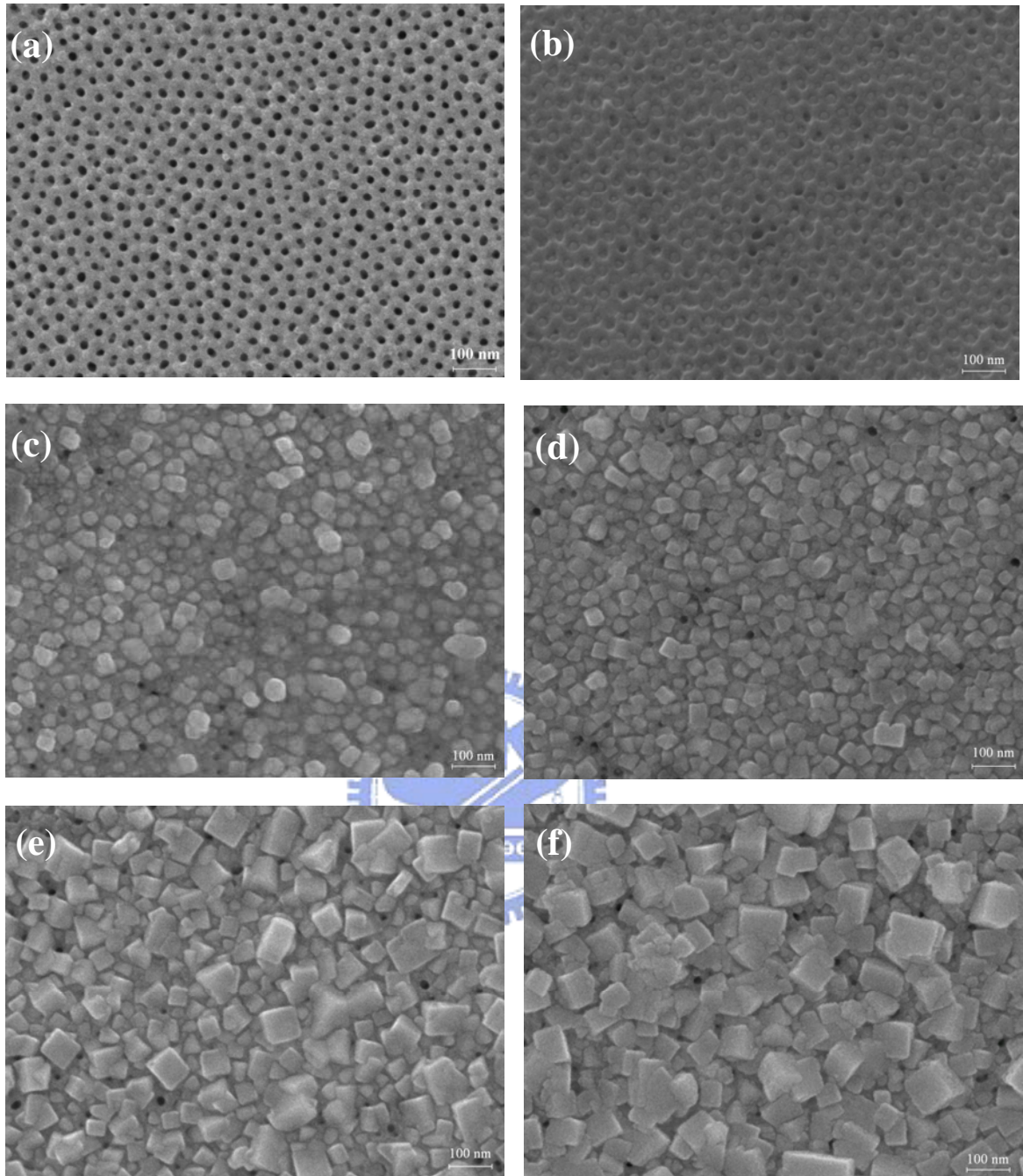
Fig. 5-15 (a) SEM image of a porous alumina membrane produced in 10% sulfuric acid solution. (b) SEM image of Pb nanowire arrays fabricated by vacuum pressure injection process. The morphologies of the PbS nanocrystals prepared at various time: (c) 1hour; (d) 3 hours; (e) 6 hours and (f) 8 hours.
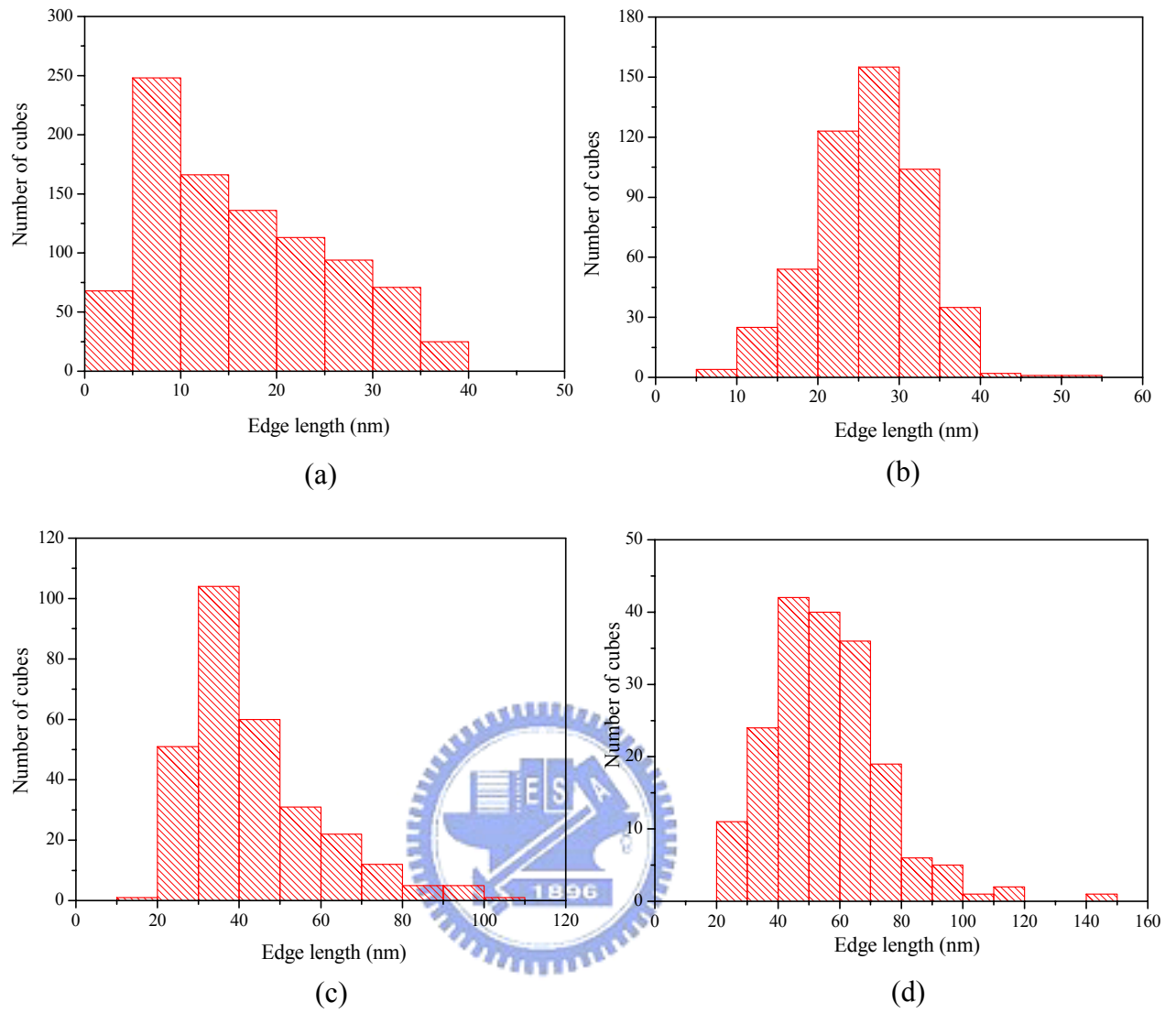
Fig. 5-16 The size distribution of the PbS cubes with different sulfization time: (a) 1

hours; (b) 3 hours; (c) 6 hours and (d) 8 hours.
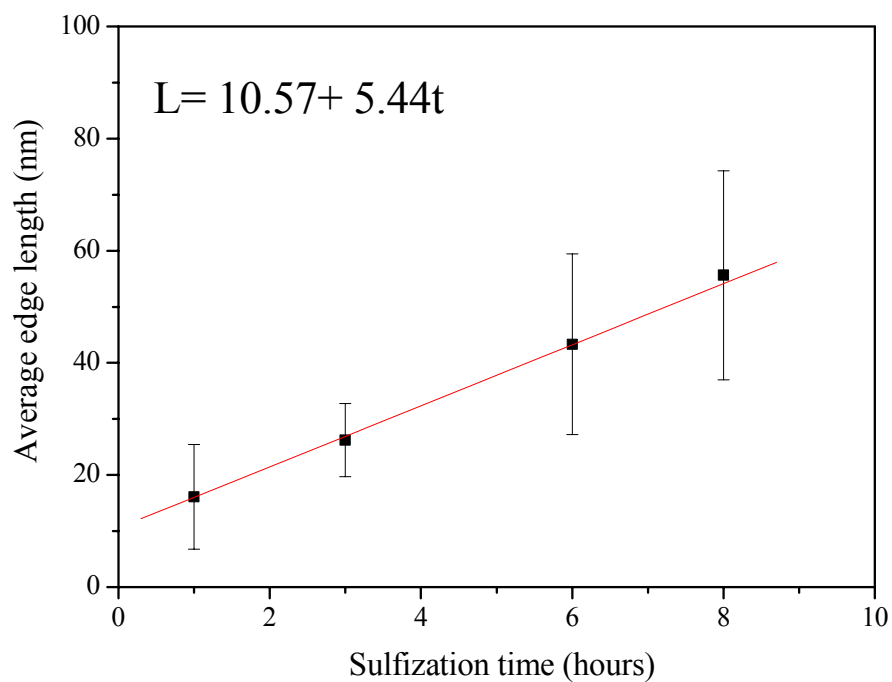
Fig. 5-17 Relationship between average edge length of PbS nanocubes and sulfization time.
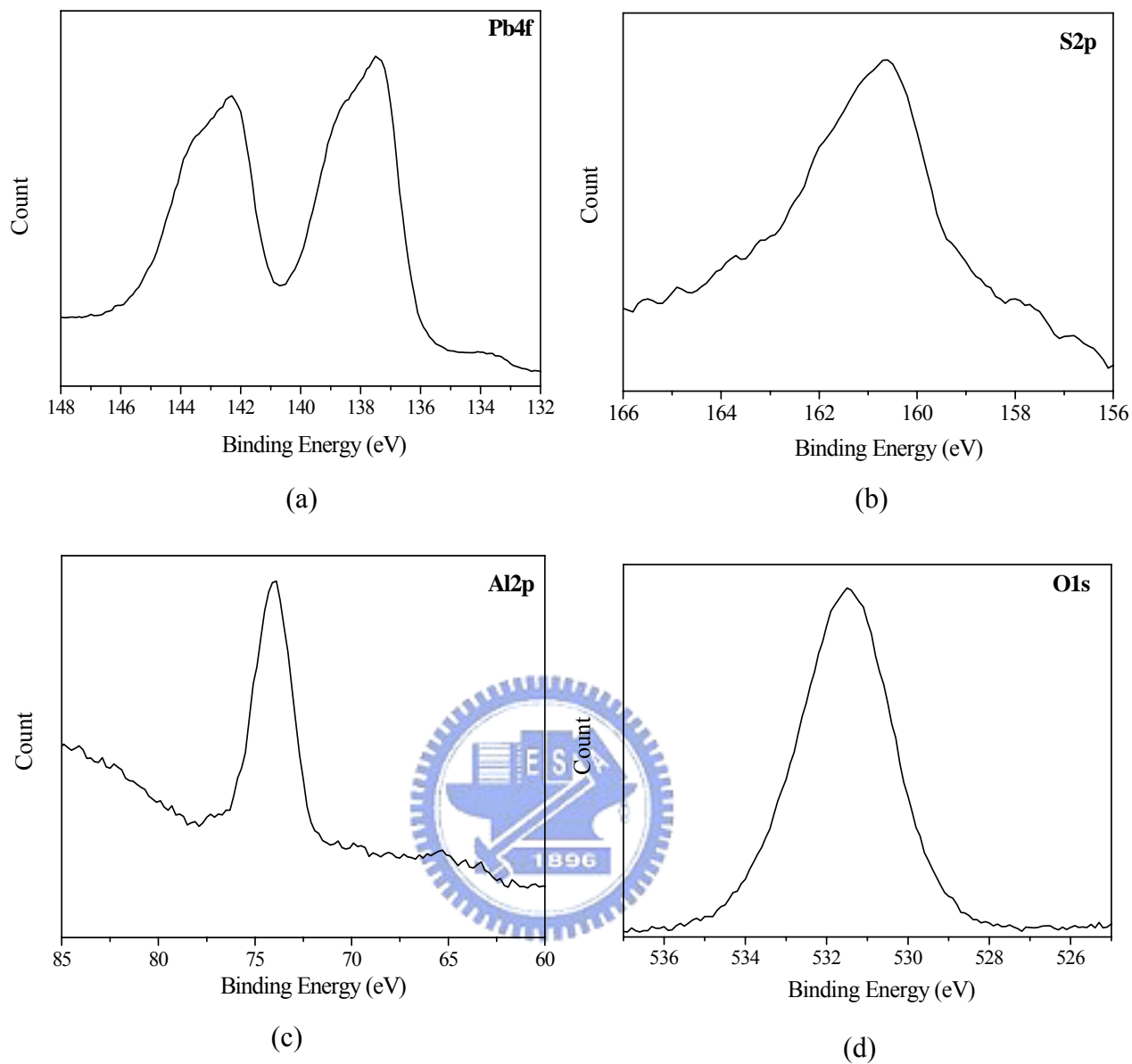
Fig. 5-18 Representative XPS spectra of the Al, O, S and Pb in the as-prepared PbS

sample.
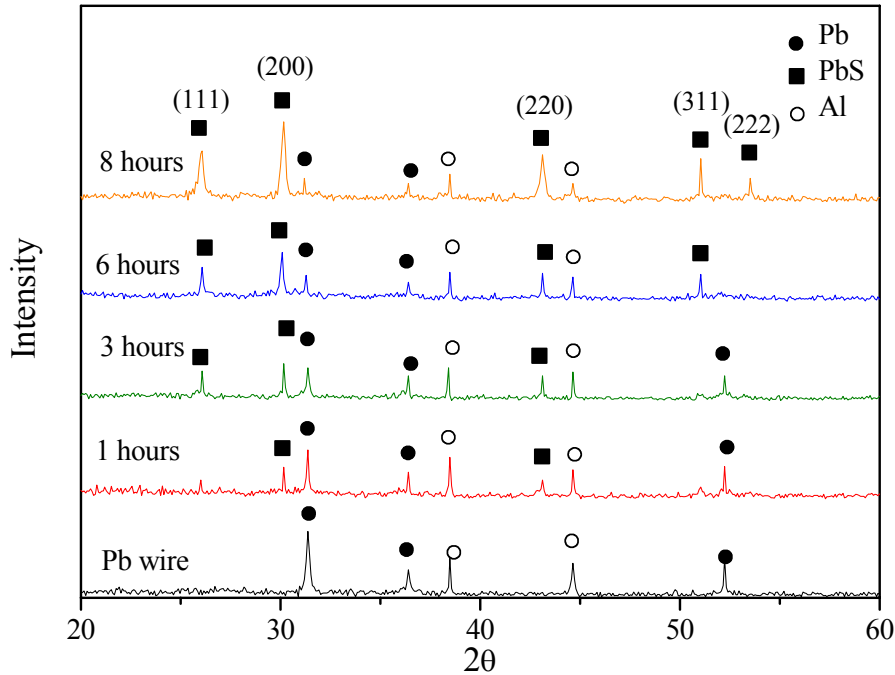
Fig. 5-19 X-ray diffraction profiles of Pb nanowires and PbS nanocrystals with different sulfization time.

The results of the X-ray diffraction analysis of PbS nanocubes with four different sulfization time are shown in Fig. 5-19. Five peaks of the PbS nanocubes identified as (111), (200), (220), (311) and (222) are the same as the peaks of Pb bulk with a face-centered cubic structure. It also can be seen that the intensity of PbS increases with the sulfization time exposed to H_2S gas.

Figure 5-20 (a) presents a TEM micrograph of a single Pb nanowire. The bright field image suggests a uniform and uninterrupted wire structure. Figure 5-20 (b) shows the corresponding selective area electron diffraction (SAED) of the Pb nanowire. According to index of the SAED, the nanowire is a single-crystal structure with a zone axis [001]. The low-magnification cross-sectional structure of PbS sample whose reaction time is 1 hour with

H$_2$S gas is presented in the bright field TEM image given in Fig. 5-20 (c). EDS analysis was performed with field emission TEM (FE-TEM) with nano-probe (~1nm) to determine the composition of the Pb-S nanocube marked in Fig. 5-20 (c). From the EDS spectrum (Fig. 5-20(d)), the nanocube is judged to consist of Pb and S in the ratio of 1:1 with a statistical error of 5%. The copper and gold signals are come from the TEM copper grid and surface conductive coating, respectively. The result is consistent with the XPS and XRD analyses which are discussed previously. High-resolution TEM (HRTEM) analyses were performed to determine the structure of PbS nanocube. The result of HRTEM imaging analysis (Fig. 5-20 (e)) indicates that the PbS nanocrystal has a cubic shape with about 8 nm edge length. The lattice fringes (d = 3.42Å) observed in the high-resolution TEM image are identical with the distance between the (111) lattice planes, confirming that the nanocrystal is composed of PbS. Figure 5-20 (f) shows the cross-sectional TEM image of the PbS nanocube with 3 hours sulfization process. It can be known that the PbS cube growing outside the pore is comprised several crystals.

The low-magnification cross-sectional structures of PbS cubes with 6 hours reaction time is presented in the bright field TEM image shown in Fig. 5-21(a). A particle growing out of the pore of the alumina membrane is marked by a circle. According to the selective-area electron diffraction pattern of this PbS nanoparticle (marked area), the particle growing outside the pore is a polycrystal structure and comprised several crystals as shown in the insert of Fig. 5-21 (a). The EDS analysis performed with TEM presents the composition of PbS nanocrystals marked in Fig. 5-21 (a). From the EDS spectrum in Fig. 5-21 (b), the nanocrystals are judged to consist of Pb and S

in the ratio of 1:1. To further confirm this result, high-resolution TEM images are performed to determine the structure of PbS nanocrystal. The HRTEM images (Figs. 5-22 (b-d)) of the boxed areas in Fig. 5-22 (a) further support the nanocrystal nature of PbS. The lattice fringes (d = 2.97Å) observed in those HRTEM images are identical with the distance between the (200) lattice planes.

When the sulfization time reaches 8 hours, the size of the nanocube outside the pore increases to 100 nm as displayed in Fig. 5-23(a). The HRTEM image (Fig. 5-23 (b)) was taken from a single crystal in a nanocube outside the pore of alumina membrane. In Fig. 5-23(c), Fast Fourier-transformation (FFT) analysis is performed on the lattice fringes from Fig. 5-23 (b) and the spots with a zone axis [001] match well with the rock salt structure of PbS. The PbS phase is identified to crystallize in cubic crystalline lattice (Fm3m, space group=225) with the lattice constant a = 0.59362 nm. Lattice-fringes image (Fig. 5-23 (d)) is generated by inverse Fourier-transformation with the (220) spots by Digital Micrograph Software [106]. A large amount of edge dislocations appear in the Fig. 5-23 (d). The edge dislocations should be created during sample preparation in the sulfization process. With increasing reaction time, the dislocations or other defects like vacancies are generated gradually.
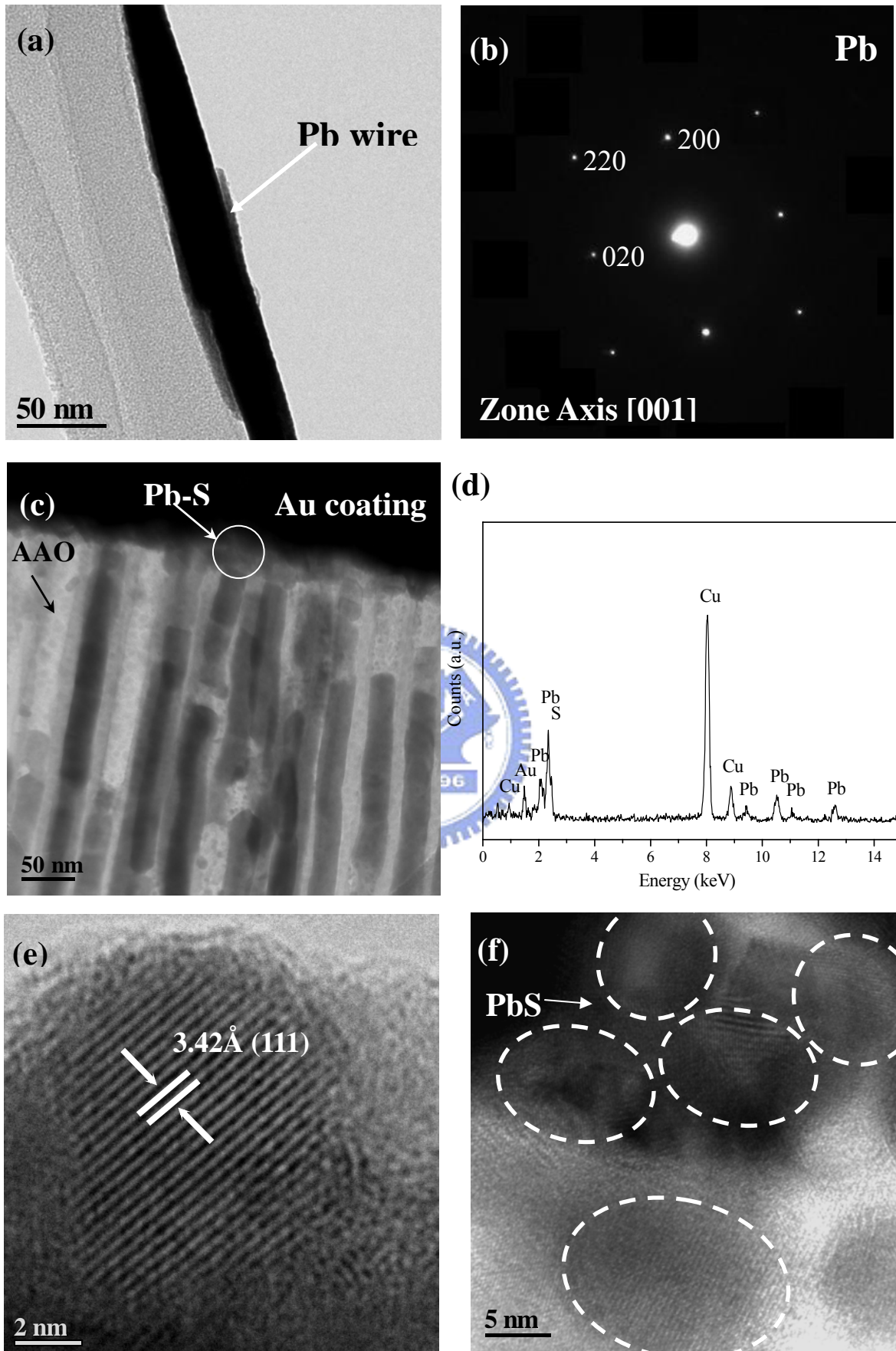
Fig. 5-20 (a) TEM image of a single Pb nanowire and (b) the selective area electron

diffraction pattern of the Pb wire. (c) Low magnification TEM image of the

PbS sample with 1 hour sulfization exposed to H_2S gas at 573 K. (d) Energy- dispersive X-ray spectrum recorded from a PbS nanocube (the circular area in (c)). (e) High resolution TEM image of a single PbS nanocrystal. (f) TEM morphology of the PbS nanocube as the reaction time was 3 hours.
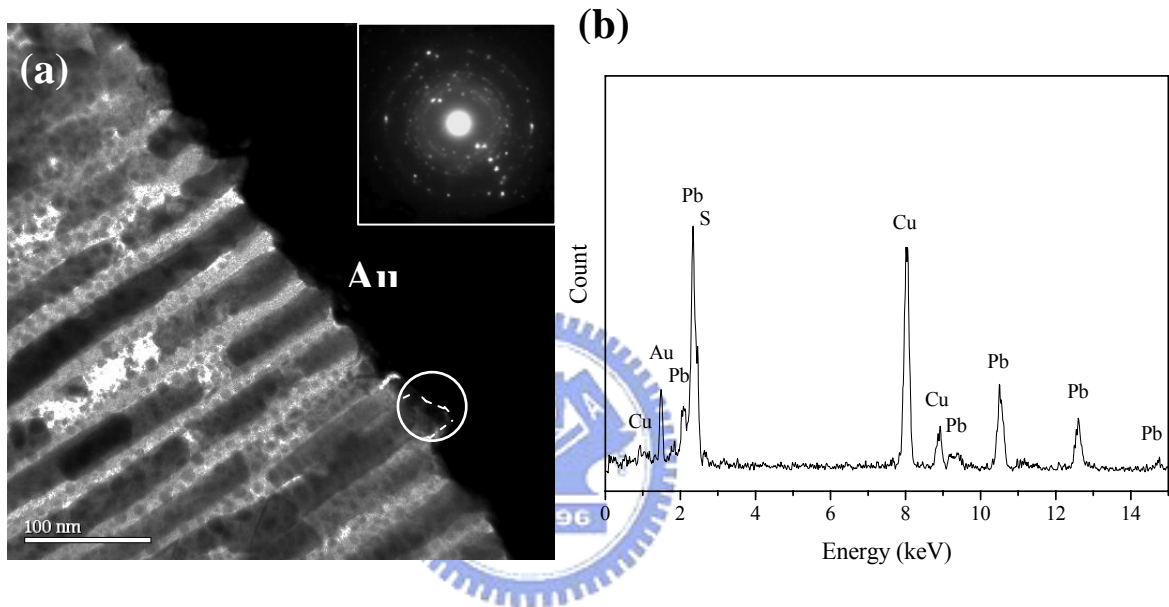
Fig. 5-21 (a) Low-magnification TEM image and the corresponding selective-area electron diffraction pattern of a PbS nanoparticle (the circular area) as the reaction time is 6 hours, and (b) Energy- dispersive X-ray spectrum recorded from a PbS nanoparticle (the circular area in (a)).
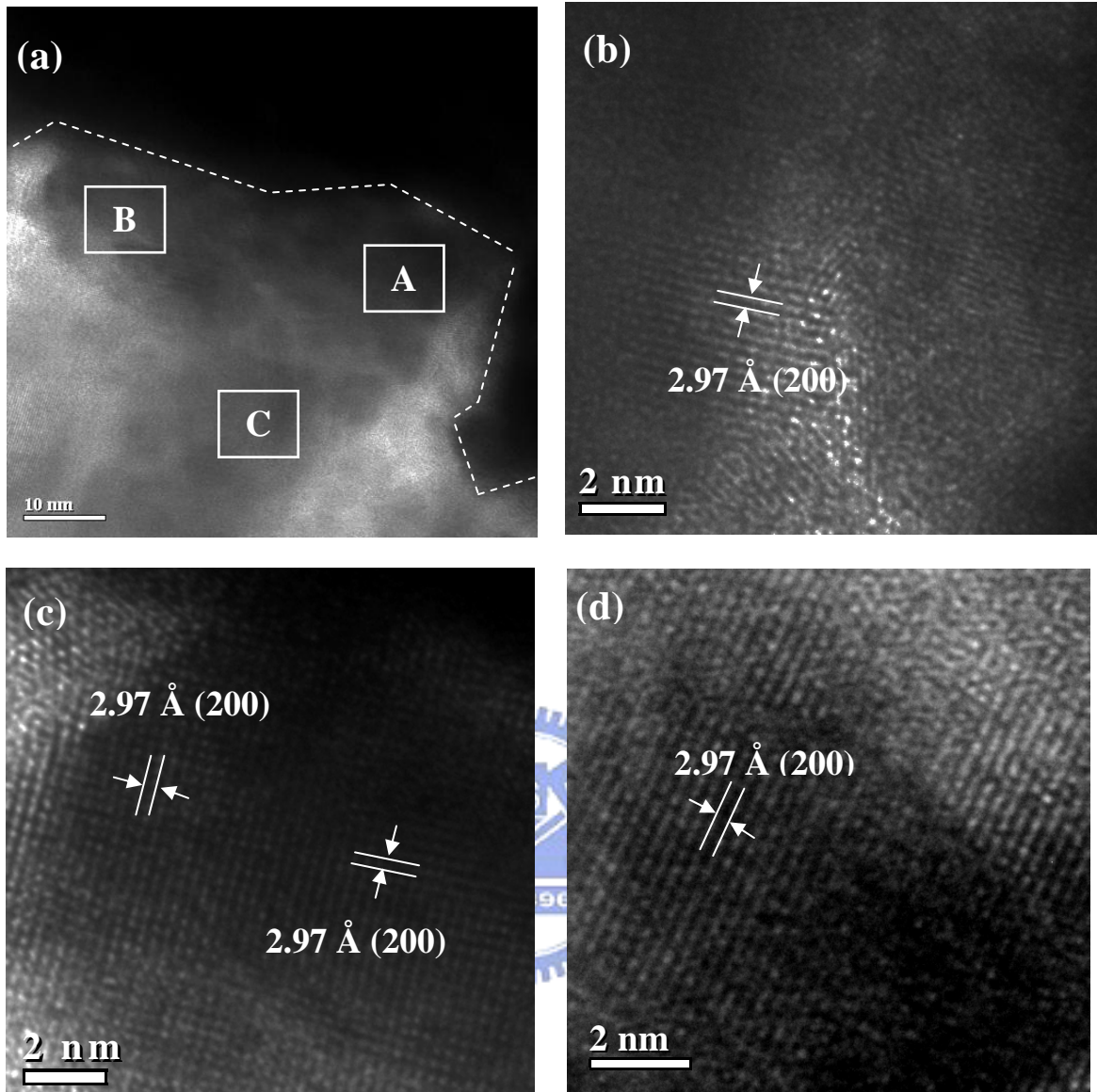
Fig. 5-22 (a) Enlarged TEM image recorded from the marked area in Fig. 5-21 (a); High-resolution TEM images of PbS nanocrystals, (b), (c) and (d), recorded from the areas indicated by A, B, and C boxes in (a), respectively.
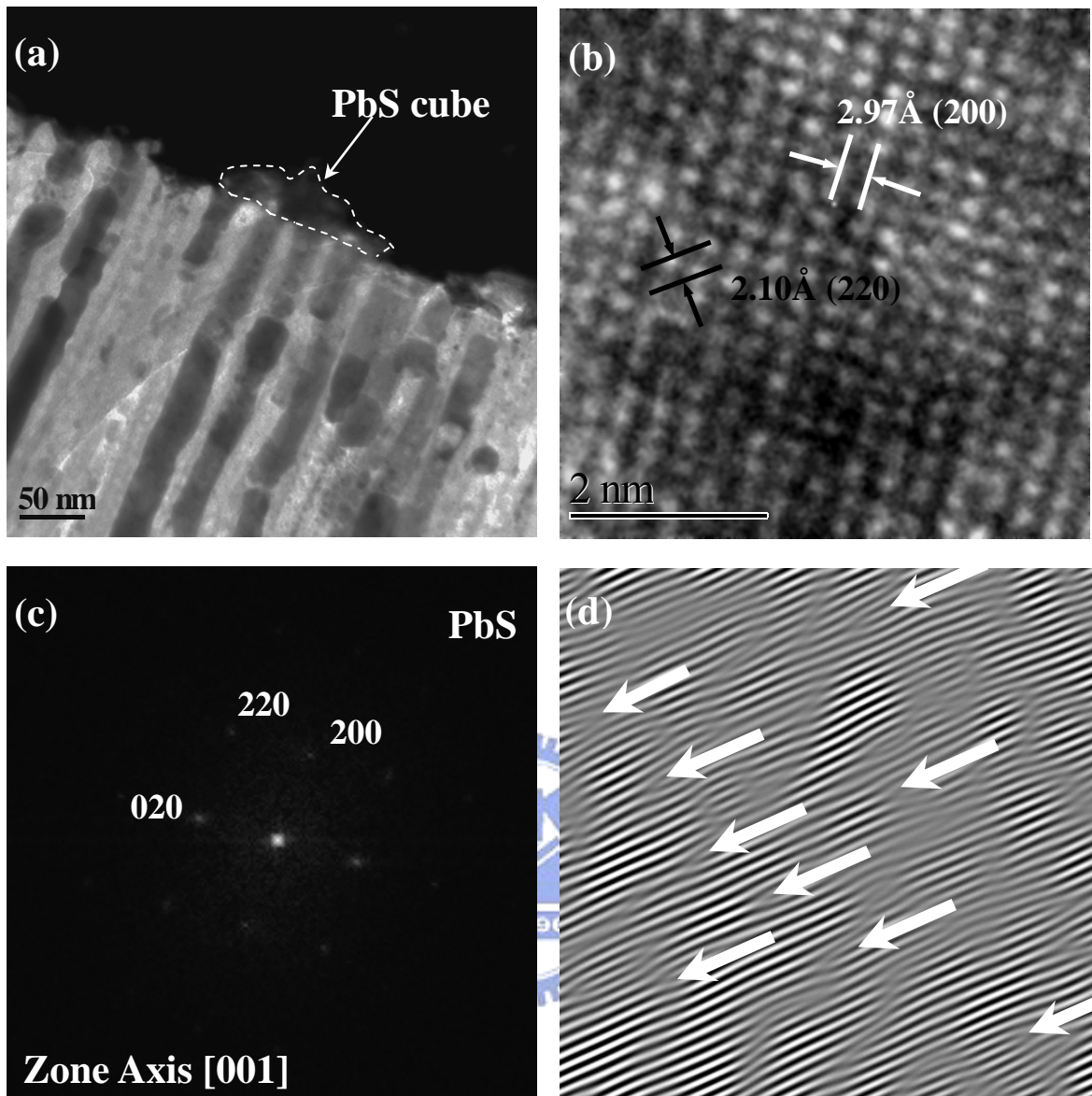
Fig. 5-23 (a) TEM image of the PbS sample with 8 hours sulfization. (b) High resolution TEM image of a single nanocrystal. (c) FFT analysis of the lattice fringes in (b) with the rock salt PbS planes indicated. (d) Inverse FFT lattice fringes image with the (220) spots by Digital Micrograph Software. The dislocations are indicated by arrows.

For the manufactures of electric or optical devices, some properties of PbS nanocrystals have to be concerned seriously, thermal stability, mechanical strength ……for instance. The DSC curves of the PbS nanocrystals in Fig. 5-24 show that there is a variation on the melting point for the Pb samples (bulk and nanowire). The melting temperature decreases from 600.0 K to 593.7 K as its size decreases. For nanocrystals embedded in a matrix, they can melt below the melting point of the bulk materials when the interfaces between embedded nanocrystals and the matrix are incoherent [107]. Therefore, the experiment result agrees well with the theoretical prediction. Furthermore, due to the potential applications in the field of microelectronics and optoelectronics, understanding of the thermal stability of low-dimensional materials is important. Mahmoud and Hamid [108] discussed that an exothermic peak (533.59 K) found in the thermal analysis spectrum attributed to the grain growth for the chemical deposition PbS powders. Moreover, there is a high intensity exothermic peak at 551.72 K in the thermal ingot powders.　In my experiment, however, the plot of DSC for PbS nanocrystals provides an information that there is no exothermic and endothermic reactions taking place in the sample during temperature range (373 K-623 K). That means the grain of the PbS nanocrystals grows slightly and non-obviously. This condition might result from the confinement of the nanochannel in the porous alumina membrane. Because the alumina membrane is a ceramic material with the excellent thermal and chemical stability, the interaction between the PbS crystals and substrate does not happen. Therefore, the PbS nanocrystals produced in our process have great thermal stability.
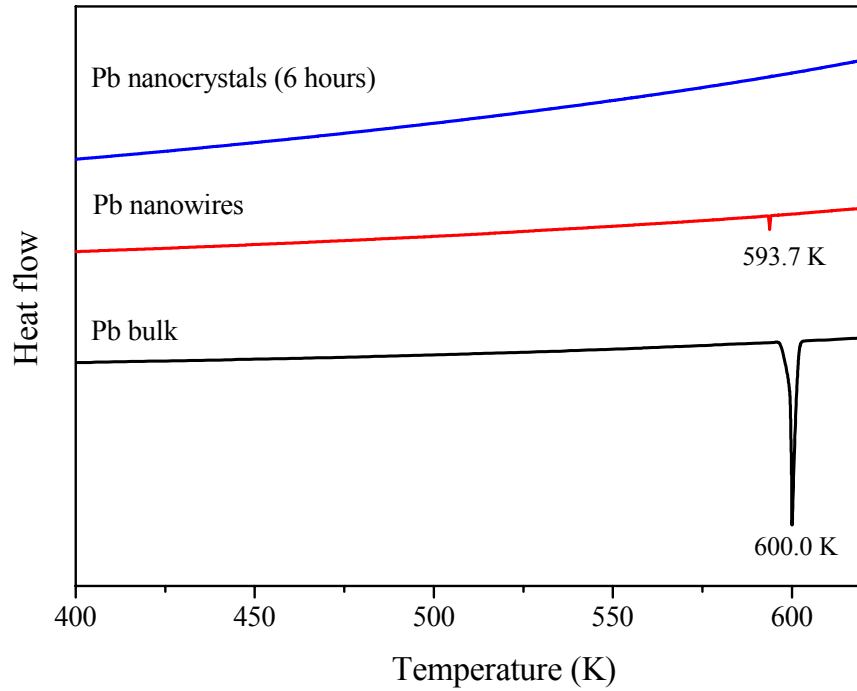
Fig. 5-24 DSC thermographs of Pb bulk, Pb nanowires and PbS nanocrystals.

5.6 Formation mechanism of PbS nanocrystals

Based on the TEM information, we set up a schematic model to explain the formation mechanism of the PbS nanocrystals. The Pb nanowire in the nanochannel has a single crystal structure shown in Fig. 5-25 (a). Applying a heat treatment in the Pb wire at 573 K, the thermal expansion of the Pb wire occurs along a particular direction toward the top of the nanochannel. The linear thermal expansion phenomenon can be determined as $l_t = l_0(1 + \alpha t)$, where l_t is the length at temperature t, l_0 is the length at 273 K and α is the coefficient of linear expansion (CLE). In this case, the value of the coefficient for Pb is 3.402×10^{-7} K^{-1} at 573 K [104]. The increasing length of Pb wire is 77.97 nm after a heat treatment. Therefore, the expansion volume out of the nanochannel can be calculated as 24495.00 nm^3 as presented in Fig. 5-25 (b).

The density of Pb and PbS are 11.34 (10^{-3} kg m^{-3}) and 7.61 (10^{-3} kg m^{-3}),

respectively. The volume expansion ratio is 49 % as Pb turns into PbS, moreover, the volume of PbS out of channel is 36497.55 nm^3 if the Pb out of channel reacted with H_2S completely. It assumes that PbS out of channel grows gradually and finally forms a cube structure whose edge length is r nm. Therefore, r can be counted as 33.17 nm and a diagonal line of the cube is 57.45 nm. Due to the distance of the pore wall (between pore and pore) is about 24 nm, the prepared PbS nanocube will aggregate together easily if reaction time is long enough.

Furthermore, the defects, such as vacancies, dislocations and so on, produce easily during the size of the substance changes because of partially incomplete crystallization. The similar result also appears in our experiment. There are much more defects in the PbS nanocrystal with 8 hours sulfization than in the PbS nanocrystal with 1 hour sulfization. The existence of the defects would influence seriously the photoluminescence properties of the PbS nanocrystals. The phenomenon will state more detailed at following section.
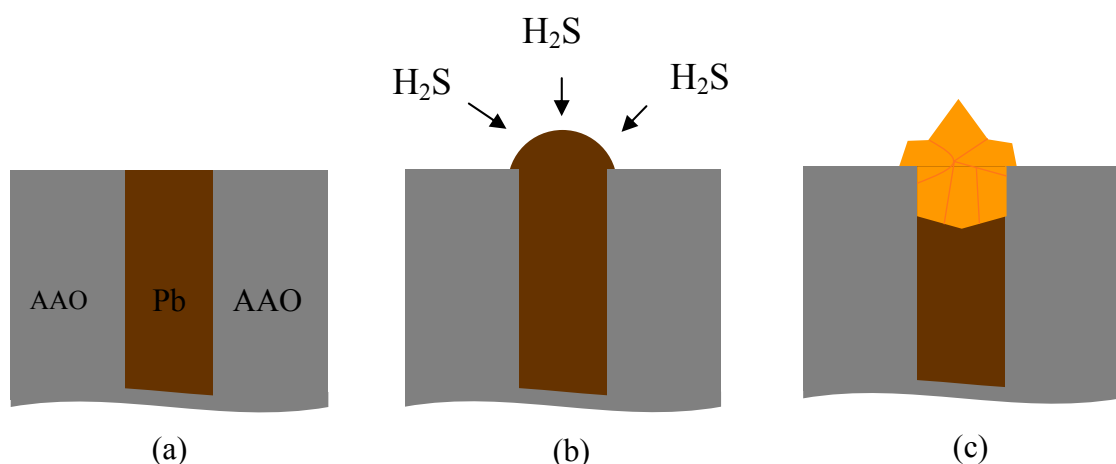
Fig. 5-25 Schematic illustration of the the PbS nanocrystals formation model.

5.7 Optical properties of PbS nanocrystals

PbS is an excellent semiconductor material because of its narrow band gap ~ 0.41eV and a large exciton Bohr radius of 18 nm [55]. Strong quantum confinement of both charge carriers (electron and hole) can be easily achieved by fabricating PbS crystals with a radius less than 18 nm. The photoluminescence (PL) emission spectra, as shown in Fig. 5-26 (a), are measured from 600 nm to 800 nm at the room temperature and the excitation wavelength is 514 nm. Figure 5-26 (a) indicates that there is no emission signal in pure Pb nanowires but a peak located around 655 nm appears after PbS nanocrystals produce. The PL properties of the PbS nanocrystals are fundamentally changed with respect to the bulk material. This modification is caused by the confinement of the free carriers into the volume of the nanocrystal. The emission intensity reaches a maximum value after 1 hour sulfization. When sulfization time is longer than 1 hour, the intensity of emission peak begins to decay and its position changes very little as the time increases. Due to the uniform size distribution, the half band width of the emission peak at 655 nm is much narrower than most others. A slight red shift is observed in the maximum of the PL spectrum as the reaction time increases. The probable explanation is that the energy gap shifts to lower energies with the increasing of the particle size due to a quantum size effect. The experimental spectrum of PbS nanocrystals with 1 hour sulfization has been deconvoluted, as shown in Fig. 5-26 (b). The orange-red emission is fit well by two Gaussian functions with a major peak centered at 655 nm (1.89 eV) and a shoulder at 670 nm (1.85 eV). To understand the physical mechanisms of the luminescence in PbS, many researches have been discussed. The electron state can determine almost any properties of nanocrystals. The electronic structure of PbS nanocrystals has been studied using the parabolic effective mass model [109], hyperbolic-hand approximation [110], tight binding type calculations [111], and four-band

envelope-function formalism [50]. The possibility of energy transitions in both electron and hole levels of PbS nanocrystals was revealed in four major types, the S_e-S_h, S_e-P_h, P_e-S_h and P_e-P_h transitions [57, 108]. In Fig. 5-26 (b), the emission peak observed at 1.89 eV corresponds to the S_e-S_h transition which is a lowest energy transition. This indicates that the photoluminescence is attributed to the direct recombination of free electron and hole, a kind of band to band transition energy, in the PbS nanocrystal. The transitions at higher energies (S_e-P_h, P_e-S_h and P_e-P_h) do not appear in our experiment because of the presence of a blue emission band (400~ 600 nm) of the porous anodic alumina membrane [9, 13].

(a)
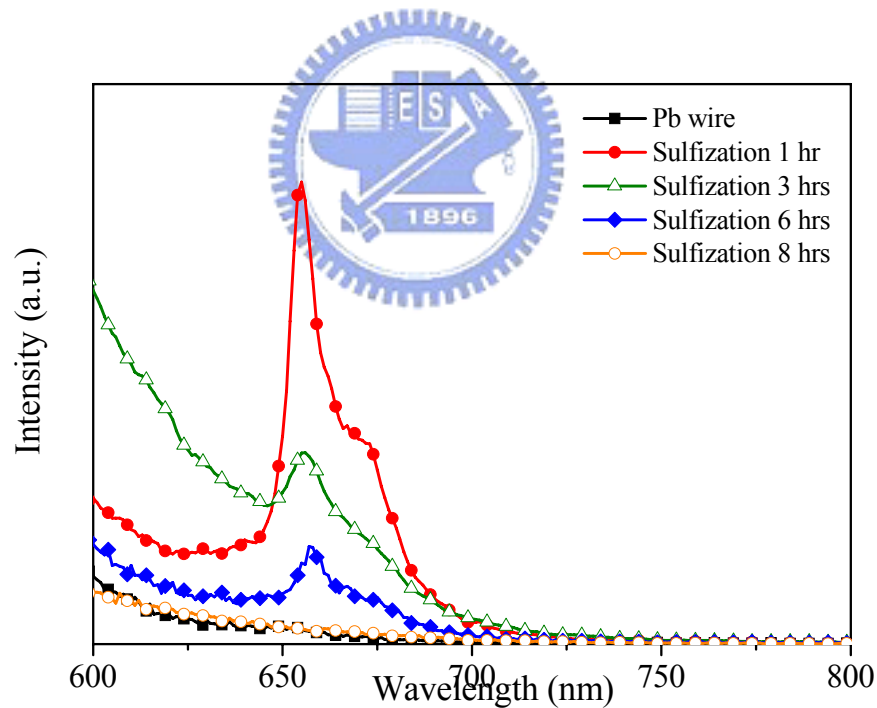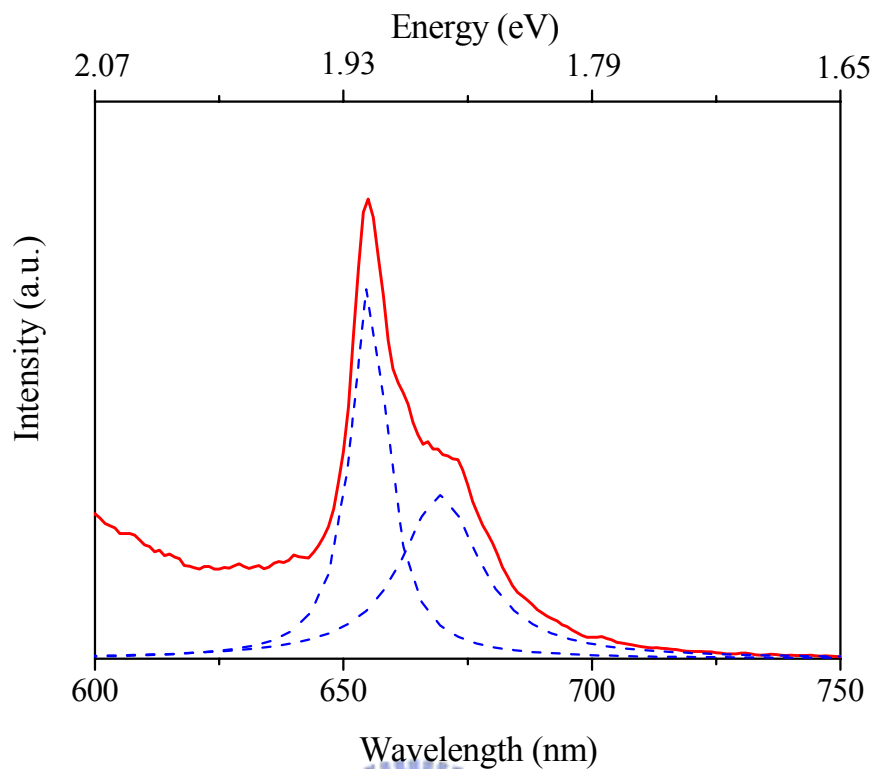
Fig. 5-26 (a) A series of PL spectra for PbS nanocrystals of different exposure time to H$_2$S gas. (b) Schematic diagram for PL curve of the PbS nanocrystals with 1 hour sulfization time whose spectra have been deconvoluted by Gaussian functions.

Additionally, PL band at the long wavelength side of PbS nanocrystals may be attributed to the defects. There have been a few researches in the PL properties of PbS nanostructures [33, 59, 68, 91, 112]. The emission related to defects in the PbS nanocrystal has not yet been observed. However, the similar result exists in other materials [113-116]. ZnSe [113] nanocrystals produced photoluminescence in a blue region, which had two components peaking at 387 nm and 475 nm. The former was assigned to the excitonic emission and the other was a defect emission. In addition, Lei and his coworkers [114] reported PL spectra of ordered TiO$_2$ nanowire arrays had three peaks which were attributed to self trapped excitons (425 nm), and two kinds of

oxygen vacancy (465, 525 nm). Furthermore, the defect emission usually has less energy than the major peak originating from the substrate and owns a wide range shoulder. In this case, the emission band peaking at 670 nm can be ascribed to electron transition by the defect energy levels in the band gap, such as vacancies or dislocations formed during sample sulfization. The concentration of defects can be increased markedly in the PbS nanocrystals as the reaction time increases. The defects will lend to nonradiative transition and stronger luminescence quenching. This fact would diminish obviously the intensity of the emission band. The condition is observed in the PL spectrum of the PbS sample with 8 hours sulfization (Fig. 5-26 (a)). Therefore, that a broad emission peak appears at 670 nm should be assigned to the defects produced from the formation of PbS nanocrystals.

5.8 Summary

In this chapter, we fabricated Pb nanowires in porous alumina membranes with different diameters by the pressure casting process. It can produce large quantity of Pb nanowires with 20, 80, 200 and 300 nm average diameters. The diameter of the nanowires can be controlled by selecting templates with a desired size. The formation of nanowires has a high temperature gradient and a slow growth rate besides the directional solidification. According to theoretical calculation, the nanowires prepared by the pressure casting process can be single crystal structure regardless of the diameter. From the TEM experiments, as the diameter of the nanowires increases, the microstructures of Pb wires are easily formed polycrystals due to the influence of mold properties. Therefore, the nanowires with 20 and 80 nm average diameters are single crystals but ones with 200 and 300 nm average diameters are polycrystals.

The PbS nanocubes were produced after Pb nanowires reacted with sulfur vapor

or H_2S gas. When the PbS nanocubes fabricated from sulfur vapor, the sulfur crystals deposited from the nonreactive sulfur species would be the occasion of the surface roughness and prevent the Pb wire from reacting with the $S_{1(g)}$ gas. Therefore, we decided to use the H_2S gas to proceed following experiments. According to the results of the TEM analysis, the PbS nanocube consists of several nanocrystals and as reaction time increases the defects in the nanocrystal increases gradually. The DSC analysis shows that there is no exothermic and endothermic reaction happened in the PbS nanocrystals. That is, the PbS nanocrystals have good thermal stability during temperature range (373 K-623 K). The photoluminescence properties are investigated and the prepared samples display a luminescence around 650-680 nm at room temperature. The emission band could be decomposed into two sub-peaks, one centered at 655 nm is contributed by the recombination of the electron and hole in the PbS nanocrystals; the other located around 670 nm is originated from defects. The existence of the defects would induce the nonradiative transition and substantially decline the intensity of the emission band. Therefore, the optimal condition fabricated the PbS nanocrystals is 1 hours sulfization. A significant quantum confinement effect makes the energy gap of PbS nanocrystals produce a blue shift from 0.41eV to 1.89 eV. On the basis of our present investigation, it may be promising for applications in the fabrication of photoelectric materials.

Chapter 6 Conclusion

1. The blue PL emission band of porous alumina membrane prepared in oxalic acid solution is consisted of two peaks: one centered at 443 nm is attributed to the oxygen defects of the alumina membranes, and the other located around 470 nm is associated with the oxalic impurities produced in the anodization process.

2. The effect of electrolyte has a large influence on the PL properties of porous alumina membrane. The alumina membranes only anodized in oxalic acid solution has a strong blue emission band.

3. The distribution of the oxalic impurities can be profiled based on the PL spectra of porous alumina membranes with different etching times. The density of the oxalic impurities increases with the depth of the pore wall, and impurities concentrate mostly in the intermediate oxide.

4. Pb nanowires with diameters of 20, 80, 200, and 300 nm have been successfully fabricated by casting process. According to theoretical calculations, the nanowires prepared by pressure casting are single crystal structures regardless of their diameters. From TEM experiments, as the diameter of the nanowires increases, the microstructure of the nanowires is easily formed polycrystals due to the effects of mold properties.

5. The PbS nanocrystals were produced after Pb wires with a diameter 20 nm reacted with H_2S gas. In order to obtain the great PL properties, the optimal

condition fabricated the PbS nanocrystals is 1 hours sulfization.

6. As indicated in the PL spectra, an orange-red emission band around 650-680 nm appears at room temperature. The emission band can be decomposed into two sub-peaks, one centered at 655 nm is contributed by the recombination of the electron and hole in the PbS nanocrystals; the other located around 670 nm is originated from defects.

7. A significant quantum confinement effect is observed in this study. It makes the energy gap of PbS nanocrystals produce a blue shift from 0.41eV to 1.89 eV.

Chapter 7 Future Work

1. The applications of porous alumina membranes as two dimensional photonic crystals or micropolarizers have been noted recently. More extensive researches would be necessary to make clear definitions in these fields.

2. The further application of porous alumina membranes is as a light extraction component in a LED. Porous alumina membrane has an appropriate reflective index between semiconductor layer of the LED and air; moreover, its surface roughness and photonic crystal structure can enhance the light extraction

3. Nonlinear optical properties of semiconductor nanocrystals are expected to be great enhanced in the strong confinement regime. Owing to a large Bohr radius and the adjustable optical absorption, these make PbS interesting for potential applications in nonlinear optics. It will be useful to investigate the nonlinear optical property of PbS nanocrystals in detail.

4. A kind of application of the PbS is the fabrication of light converting electrodes which can be obtained by producing PbS nanocrystals in porous titania template. In this divice, visible light is absorbed by PbS nanocrystals, followed by electron transfer into the porous TiO_2 membrane. There are several advantages to use PbS nanocrystals instead of organic dyes: the band gap or the absorption range can be easily adjustable by the size of the nanocrystals, and the absorption behavior has the higher photo-electro conversion efficiency.

REFERENCE

1. D. R. Vij: *Luminescence of Solid*, Plenum Press (1998).

2. J. B. Birks: *Standardization in Spectrophotometry and Luminescence Measurements*, Nat. Bur. Std. Special Publ. (1977).

3. Klaus D. Mielenz: *Measurement of Photoluminescence*, Academic Press, INC. (1982).

4. B. D. Evans, M. Stapelbroek: Phys. Rev. B **18**, 7089 (1978).

5. B. G. Draeger, G. P. Summers: Phys. Rev. B **19**, 1172 (1979).

6. P. Lacovara, L. Esterowitz, M. Kokta: IEEE J. Quantum Electron. **21**, 1614 (1985).

7. W. Chen, H. Tang, C. Shi, J. Deng, J. Shi, Y. Zhou, S. Xia, Y. Wang, S. Yin: Appl. Phys. Lett. **67**, 317 (1995).

8. Y. Du, W. L. Cai, C. M. Mo, J. Chen, L. D. Zhang, X. G. Zhu: Appl. Phys. Lett. **74**, 2951 (1999).

9. Y. Li, G. H. Li, G. W. Meng, L. D. Zhang, F. Phillipp: J. Phys.: Condens. Matter **13**, 2691 (2001).

10. J. H. Wu, X. L. Wu, N. Tang, Y. F. Mei, X. M. Bao: Appl. Phys. A **72**, 735 (2001).

11. G. S. Huang, X. L. Wu, Y. F. Mei, X. F. Shao: J. Appl. Phys. **93**, 582 (2003).

12. Y. Yamamoto, N. Baba, S. Tajima: Nature **289**, 572 (1981).

13. T. Gao, G. Meng, L. Zhang: J. Phys.: Condens. Matter **15**, 2071 (2003).

14. G. H. Li, Y. Zhang, Y. C. Wu, L. D. Zhang: J. Phys.: Condens. Matter **15**, 8663 (2003).

15. Z. J. Li, K. L. Huang: Luminescence (2006).

16. L. Dong, Y. Chu, Y. Liu, M. Li, F. Yang, L. Li: J. Colloid Interface Sci. **301**, 503 (2006).

17. M. A. Hines, G. D. Scholes: Adv. Mater. **15**, 1844 (2003).

18. D. S. Koktysh, J. R. McBride, S. K. Dixit, L. C. Feldman, S. J. Rosenthal: Nanotechnology **18**, 1 (2007).

19. M. S. Bakshi, P. Thakur, S. Sachar, G. Kaur, T. S. Banipal, F. Possmayer, N. O. Petersen: **111** ,18087 (2007).

20. C. Zhang, Z. Kang, E. Shen, E. Wang, L. Gao, F. Luo, C. Tian, C. Wang, Y. Lan, J. Li, X. Cao: J. Phys. Chem. B **110**, 184 (2006).

21. J. P. Yang, S. B. Qadri, B. R. Ratna: J. Phys. Chem. **100**, 17255 (1996).

22. G. Lin, A. Xicheng: Mater. Chem. Phys. **63**, 30 (2000).

23. S. M. Lee, Y. W. Jun, S. N. Cho, J. Cheon: J. Am. Chem. Soc. **124**, 11244 (2002).

24. Y. Ma, L. Qi, J. Ma, H. Cheng: Cryst. Growth Des. **4** ,351 (2004).

25. M. Bashouti, E. Lifshitz: Inorg. Chem. **47**, 678 (2008).

26. G. Zhou, M. Lü, Z. Xiu, S. Wang, H. Zhang, Y. Zhou, S. Wang: J. Phys. Chem. **110**, 6543 (2006).

27. J. P. Ge, J. Wang, H. X. Zhang, X. Wang, Q. Peng, Y. D. Li: Chem. Eur. J. **11**, 1889 (2005).

28. A. A. Rempel, N. S. Kozhevnikova, A. J. G. Leenaers, S. Van den Berghe: J. Cryst. Growth **280**, 300 (2005).

29. S. Chen, W. Liu: Mater. Chem. Phys. **98**, 183 (2006).

30. Y. J. Yang: Mater. Sec. Eng. B **131** ,200 (2006).

31. X. Changqi, Z. Zhicheng, W. Hailong, Y. Qiang: Mater. Sec. Eng. B **104**, 5 (2003).

32. Y. Ni, H. Liu, F. Wang, Y. Liang, J. Hong, X. Ma, Z. Xu: Cryst. Growth Des. **4**, 759 (2004).

33. Y. Ni, H. Liu, F. Wang, Y. Liang, J. Hong, X. Ma, Z. Xu: Crys. Res. Technol. **39**, 200 (2004).

34. S. Wang, S. Yang: Langmuir **16**, 389 (2000).

35. A. A. R. Watt, H. Rubinsztein-Dunlop, P. Meredith: Mater. Lett. **59**, 3033 (2005).

36. A. A. R. Watt, D. Blake, J. H. Warner, E. A. Thomsen, E. L. Tavenner, H. Rubinsztein-Dunlop, P. Meredith: J. Phys. D: Appl. Phys. **38**, 2006 (2005).

37. M. T. Nenadovic, M. I. Comor, V. Vasic, O. I. Micic: J. Phys. Chem. **94**, 6390 (1990).

38. J. Kuljanin, M. I. Comor, V. Djokovic, J. M. Nedeljkovic: Mater. Chem. Phys. **95**, 67 (2006).

39. T. D. Krauss, F. W. Wise: Phys. Rev. B **55**, 9860 (1997).

40. K. K. Nanda, S. N. Sahu, R. K. Soni, S. Tripathy: Phys. Rev. B **58**, 15405 (1998).

41. R. Vogel, P. Hoyer, H. Weller: J. Phys. Chem. **98**, 3183 (1994).

42. R. Könenkamp, P. Hoyer, A.Wahi: J. Appl. Phys. **79**, 7029 (1996).

43. B. Ma, F. Luo, L. Wang, X. Wu, C. Zhan, Y. Qiu: Jpn. J. Appl. Phys. **46**, 7745 (2007).

44. A. A. Lipovskii, E. V. Kolobkova, A. Olkhovets, V. D. Petrikov, F. W. Wise: Physica E **5**, 157 (2000).

45. A. M. Malyarevich, V. G. Savitsky, I. A. Denisov, P. V. Prokoshin, K. V. Yumashev, E. Raaben, A. A. Zhilin, A. A. Lipovskii: Phys. Stat. Sol. (b) **224**, 253 (2001).

46. C. Kittel: *Introduction to solid state physics*, John Wiley & Son, Inc. (1996).

47. P. N. Prasad: *Nanophotonics*, John Wiley & Son, Inc. (2004).

48. F. W. Wise: Acc. Chem. Res. **33**, 773 (2000).

49. C. Dushkin, K. Papazova, N. Dushkina, E. Adachi: Colloid. Polym. Sci. **284**, 80 (2005).

50. I. Kang, F. W. Wise: J. Opt. Soc. Am. B **14**, 1632 (1997).

51. A. D. Yoffe: Adv. Phys. **42**, 173 (1993).

52. J. H. Warner, E. Thomsen, A. R. Watt, N. R. Heckenberg, H. Rubinsztein-Dunlop: Nanotechnology **16**, 175 (2005).

53. M. J. Fernée, A. Watt, J. Warner, S. Cooper, N. Heckenberg, H. Rubinsztein-Dunlop: Nanotechnology **14**, 991 (2003).

54. I. Chakraborty, S. P. Moulik: J. Nanoparticle Res. **6**, 233 (2004).

55. M. J. Fernée, A. Watt, J. Warner, N. Heckenberg, H. Rubinsztein-Dunlop: Nanotechnology **15**, 1328 (2004).

56. S. Chen, L. A. Truax, J. M. Sommers: Chem. Mater. **12**, 3864 (2000).

57. J. L. Machol, F. W. Wise, R. C. Patel, D. B. Tanner: Phys. Rev. B **48**, 2819 (1993).

58. K. S. Kang: Appl. Phys. Lett. **85**, 293 (2004).

59. F. Gao, Q. Lu, X. Liu, Y. Yan, D. Zhao: Nano Lett. **1**, 743 (2001).

60. L. Bakueva, S. Musikhin, M. A. Hines, T. W. F. Chang, M. Tzolov, G. D. Scholes, E. H. Sargent: Appl. Phys. Lett. **82**, 2895 (2003).

61. M. J. Fernée, A. Watt, J. Warner, N. Heckenberg, H. Rubinsztein-Dunlop: Nanotechnology **15**, 1351 (2004).

62. H. Gao, G. Wang, S. Zhang, X. Zhang: Nanotechnology **17**, 3280 (2006).

63. R. E. de Lamaëstre, H. Bernas: J. Appl. Phys. **98**, 114310 (2005).

64. B. Yu, G. Yin, C. Zhu, F. Gan: Opt. Mater. **11**, 17 (1998).

65. C. Lü, C. Guan, Y. Liu, Y. Cheng, B. yang: Chem. Mater. **17**, 2448 (2005).

66. L. Fushman, D. Englumd, J. Vuckovic: Appl. Phys. Lett. **87**, 241102 (2005).

67. R. Thielsch, T. Böhme, R. Reiche, D. Schläfer, H. D. Bauer, H. Böttcher: Nano struc. Mater. **10**, 131 (1998).

68. Y. Hu, J. Chen, X. Jin, W. Chen: Mater. Lett. **59**, 234 (2005).

69. M. T. Wu, I. C. Leu, M. H. Hon: J. Vac. Sci. Technol. B **20**, 776 (2002).

70. S. Shingubara, K. Morimoto, H. Sakaue, T. Takahagi: Electrochem. Solid- state

Lett. **7**, E15 (2004).

71. N. Stein, M. Rommlfangen, V. Hody, L.Johann, J. M. Lecuire: Electrochem. Acta **47**, 1811 (2002).

72. Y. Huang, X. Duan, Y. Gui and C. M. Lieber: Nano Lett. **2**, 101 (2002).

73. K. Nielsch, F. Muller, A. P. Li, U. Gosele: Adv. Mater. **12**, 582 (2002).

74. G. L. Che, B. B. Laksshmi, E. R. Fisher, C. R. Martin: Nature **393**, 346 (1998).

75. S. Z. Chu, S. Inoue, K. Wada, D. Li, H. Haneda: J. Mater. Chem. **13**, 866 (2003).

76. F. Matsumoto, K. Nishio, H. Masuda: Adv. Mater. **16**, 2105 (2004).

77. O. Jessensky, F. Muller, U. Gosele: Appl. Phys. Lett. **72**, 1173 (1998).

78. S. Ono, H. Ichinose, N. Masuko: Corros. Sci. **33**, 841 (1992).

79. J. Choi, Y. Luo, R. B. Wehrspohn, R. Hillebrand, J. Schilling, U. Gösele: J. Appl. Phys. **94**, 4757 (2003).

80. K. Tanaka: Science **277**, 1786 (1997).

81. M. Sugisaki, H. W. Ren, S. V. Nair, K. Nishi, Y. Masumoto: Phys. Rev. B **66**, 235309 (2002).

82. F. Wu, J. W. Lewis, D. S. Kliger, J. Z. Zhang: J. Chem. Phys. **118**, 12 (2003).

83. Y. Q. Wang, Y. Ishikawa, N. Shibata: Jpn. J. Appl. Phys. **41**, 5177 (2002).

84. S. K. Sarkar, N. Chandrasekharan, S. Gorer, G. Hodes: Appl. Phys. Lett. **81**, 5045 (2002).

85. X. D. Wang, P. X. Gao, J. Li, C. J. Summers, Z. L. Wang: Adv. Mater. **14**, 1732 (2002).

86. K. Murakoshi, H. Hosokawa, S. Yanagida: Jpn. J. Appl. Phys. **38**, 522 (1999).

87. Y. Jiang, X. M. Meng, J. Liu, Z. R. Hong, C. S. Lee, S.T. Lee: Adv. Mater. **15**, 1195 (2003).

88. X. Zhang, Y. Xie, Q. Zhao, Y. Tian: New J. Chem. **27**, 827 (2003).

89. F. Goto, M. Ichimura, E. Arai: Jpn. J. Appl. Phys. **36**, L1146 (1997).

90. Q. Lu, F. Gao, D. Zhao: Nano Lett. **2**, 725 (2002).

91. J. H. Warner, A. A. R. Watt, R. D. Tilley: Nanotechnology **16**, 2381 (2005).

92. R. Plass, S. Pelet, J. Krueger, M. Grätzel, U. Bach: J. Phys. Chem. B **106**, 7578 (2002).

93. S. W. Lu, U. Sohling, M. Menning, H. Schmidt: Nanotechnology **13**, 669 (2002).

94. P. Villars, L. D. Calvert: *Pearson's Handbook of Crystallographic Data for intermetallic phases*, Materials Park, OH/ASM International (1991).

95. JCPDS No.04-0686.

96. I. Barin: *Thermochemical Data of Pure Substances*, VCH Publishers, Inc. (1995).

97. Z. Zhang, J. Y. Ying, M. S. Dresselhaus: J. Mater. Res. **13**, 1745 (1998).

98. C. C. Chen, Y. Bisrat, Z. P. Luo, R. E. Schaak, C. G. Chao, D. C. Lagoudas: Nanotechnology **17**, 367 (2006).

99. B. B. Alchagirov, A. G. Mozgovoy, Kh. B. Khokonov: High Temp. **41** , 755 (2003).

100. C. W. Extrand: Langmuir **18**, 7991 (2002).

101. M. C. Flemings: *Solidification Processing*, McGraw-Hill (1974).

102. W. Kurz, D. J. Fisher: *Fundamentals of solidification*, Trans Tech Publication Ltd. (1992).

103. M. W. Chase, C. A. Davies: *NIST-JANAF Thermochemical Tables*, Dow Chemical Company. Thermal Research Laboratory (1985).

104. I. S. Grigoriev, E. Z. Meilikhov: *Handbook of Physical Quantities*, Boca Raton /CRC Press (1997).

105. J. F. Moulder, W. F. Stickle, P. E. Sobol, K. D. Bomben: *Handbook of X-ray Photoelectron Spectroscopy*, Perkin-Elmer Corporation, Physical Electronics Division (1992).

106. Gatan Inc., DigitalMicrograph 3.10.0 for GMS 1.5.0 (2003).

107. Z. Zhang, J. C. Li, Q. Jiang: J. Phys. D: Appl. Phys. **33**, 2653 (2000).

108. S. Mahmoud, O. Hamid: FIZIKAN A **10**, 21 (2001).

109. L. E. Brus: J. Chem. Phys. **80**, 4403 (1984).

110. Y. Wang, A. Suna, W. Mahler, R. Kasowski: J. Chem. Phys. **80**, 7315 (1987).

111. R. S. Kane, R. E. Cohen, R. Silbey: J. Phys. Chem. **100**, 7928 (1996).

112. M. J. Fernee, J. Warner, A. Watt, S. Cooper, N. R. Heckenberg, H. Rubinsztein-Dunlop: Nanotechnology **15**, 16 (2004).

113. N. Murase, M. Gao: Mater. Lett. **58**, 3898 (2004).

114. Y. Lei, L. D. Zhang, G. W. Meng, G. H. Li, X. Y. Zhang, C. H. Liang, W. Chen, S. X. Wang: Appl. Phys. Lett. **78**, 1125 (2001).

115. S. C. Lyu, Y. Zhang, H. Ruh, H. J. Lee, H. W. Shim, E. K. Suh, C. J. Lee: Chem. Phys. Lett. **363**, 134 (2002).

116. C. R. M. de Oliveira, A. M. de Paula, F. O. Plentz Filho, J. A. Medeiros Neto, L. C. Barbosa, O. L. Alves, E. A. Menezes, J. M. M. Rios, H. L. Fragnito, C. H. Brito Cruz, C. L. Cesar: Appl. Phys. Lett. **66**, 439 (1995).

PUBLICATION LIST

SCI Journal papers:

1. Chien Chon Chen, **Jung Hsuan Chen**, Chuen Guang Chao, *Post-treatment Method of Producing Ordered Array of Anodic Aluminum Oxide*, Jpn. J. Appl. Phys. (2004) **43**, 8354–8359.

2. Chien-Chon Chen, Chin-Guo Kuo, **Jung-Hsuan Chen**, Chuen-Guang Chao, *Nanoparticles of Pb–Bi Eutectic Nucleation and Growth on Alumina Template*, Jpn. J. Appl. Phys. (2005) **44**, 1529-1533.

3. Chin-Guo Kuo, Shen-Chuan Lo, **Jung-Hsuan Chen**, Cheng-Cheng Chlang, Chuen-Guang Chao, *Formation Procedure and Microstructural Analysis of Pb7Bi3 (Pb–Bi) Alloy Nanowires*, Jpn. J. Appl. Phys. (2005) **44**, 3333-3336.

4. Chien-Chon Chen, **Jung-Hsuan Chen**, Chuen-Guang Chao, *Electrochemical Characteristics of Surface of Titanium formed by Electrolytic Polishing and Anodizing*, J. Mater. Sci. (2005) **40**, 4053-4059.

5. **Jung Hsuan Chen**, Chin Ping Huang, Chuen Guang Chao, Teng Ming Chen, *The Investigation of Photoluminescence Centers in Porous Alumina Membranes*, Appl. Phys. A (2006) **84**, 297-300.

6. **Jung-Hsuan Chen**, Chuen-Guang Chao, Jong-Chyan Ou, Tzeng-Feng Liu, *Growth and Characteristics of Lead Sulfide Nanocrystals Produced by the Porous Alumina Membranes*, Surface Sci. (2007) **601**, 5142-5147.

7. **Jung-Hsuan Chen**, Shen-Chuan Lo, Chuen-Guang Chao, Tzeng-Feng Liu, *A Study on Fabrication, Morphological and Optical Properties of Lead Sulfide Nanocrystals*, J. Nanosci. Nanotechnol. (2008) **8**, 967-972.

8. **Jung-Hsuan Chen**, Shen-Chuan Lo, Chuen-Guang Chao, Tzeng-Feng Liu, *Microstructure and Properties of Pb Nanowires Fabricated by Casting*, Jpn. J. Appl. Phys. (2008) **47**, 4815-4819.

International conference papers:

1. Chien-Chon Chen, **Jung-Hsuan Chen**, Wen C. Say, Chuen-Guang Chao, *The Fabrication of Ordered Nanochannel Anodic Titanium Oxide and Thermodynamics Property of Gibbs Free Energy*, 2nd International Conference on Materials for Advanced Technologies &IUMRS-International Conference in Asia 2003, 2003, Suntec, Singapore.

2. Chin-Guo Kuo, **Jung-Hsuan Chen**, Yung-Yuan Hsu, Maw-Kuen Wu, Chuen-Guang Chao, *Procedure and Characterization of Eutectic Lead-Bismuth Alloy Nanowires*, IUMRS-International Conference in Asia 2004, 2004, Hsinchu, Taiwan.

3. **Jung-Hsuan Chen**, Chuen-Guang Chao, Jong-Chyan Ou, *Growth and Characteristics of Lead Sulfide Nanocrystals Produced by the Porous Alumina Membrane*, The tenth ISSP International Symposium on Nanoscience at Surfaces, 2006, P-095, Tokyo, Japan.

4. **Jung-Hsuan Chen**, Shen-Chuan Lo, Chuen-Guang Chao, Tzeng-Feng Liu, *Microstructure and Properties of Pb Nanowires Fabricated by Casting Process*, The 2nd International Conference on Surfaces, Coatings and Nanostructured Materials, 2007, NFC 28, Algarve, Portugal.

中文期刊:

1. 郭金國、**陳蓉萱**、朝春光,*鉛鉍合金奈米線之研究*,鑄造工程學刊,(2005) **31**,33-36。

研討會論文:

1. 郭金國、**陳蓉萱**、朝春光,*規則性排列的氧化鋁奈米孔洞的製備*,中華民國陶業研究學會九十三年度會員大會暨學術論文發表會論文集,2004,台北。

2. 陳建仲、**陳蓉萱**、朝春光，*利用模板法製作奈米線*，九十三年度中國材料科學學會論文集，2004，新竹。

3. 郭金國、**陳蓉萱**、朝春光，*鉛鉍合金奈米線之研究*，台灣鑄造學會九十三年度論文發表會論文集，2004，台北。

4. **陳蓉萱**、陳建仲、郭金國、朝春光，*有序硫化鉛奈米線陣列的製備與特性研究*，九十四年度中國材料科學學會論文集，2005，台北。

5. **陳蓉萱**、楊大緯、朝春光、李秉璋，*利用鑄造法製備 BiSbTe 奈米線陣列之研究*，九十五年度中國材料科學學會論文集，2006，台南。

6. 羅文翔、**陳蓉萱**、朝春光、劉增豐，*三點彎曲實驗量測陽極氧化鋁模板機械性質以及破斷面分析*，九十六年度中國材料科學學會論文集，2007，新竹。

7. **陳蓉萱**、楊大緯、廖筱媛、朝春光，*利用壓鑄法製備奈米銀線*，九十六年度中國材料科學學會論文集，2007，新竹。

專利:

1. 朝春光、郭金國、陳建仲、**陳蓉萱**，*新穎離心法製作奈米球、奈米線及元件*，中華民國專利證號：I243752 (2005)。

2. 朝春光、郭金國、陳建仲、**陳蓉萱**，*製造奈米線的方法和儀器*，中華民國專利證號：I262221 (2006)。

3. 朝春光、陳建仲、**陳蓉萱**、郭金國，*鋁陽極處理製作陣列式奈米孔洞模板的後處理法*，中華民國專利証號: I285225 (2007)。

4. 朝春光、胡明理、**陳蓉萱**、劉緒東，*發光二極體結構及其製造方法*，申請國別: 台灣，申請中 (2006)。

5. 朝春光、胡明理、**陳蓉萱**、劉緒東，*發光二極體結構及其製造方法*，申請國別: 台灣，申請中 (2006)。

6. 朝春光、胡明理、**陳蓉萱**、劉緒東，*發光二極體結構及其製造方法*，申請國

別: 台灣，申請中 (2007)。

7. 朝春光、胡明理、**陳蓉萱**、劉緒東，*發光二極體結構及其製造方法*，申請國別: 台灣，申請中 (2007)。

8. 朝春光、**陳蓉萱**、楊大緯，*奈米熱電裝置的製造方法*，申請國別: 台灣，申請中 (2008)。

9. 朝春光、**陳蓉萱**、楊大緯，*奈米熱電裝置的製造方法*，申請國別: 美國，申請中 (2008）。